CHARLOTTE WALTER

EFFECTS AND VARIABILITY OF DECLINE IN SEA ICE ON MARINE PRIMARY PRODUCTION IN THE ARCTIC

UNIVERSIDADE DO ALGARVE
Faculdade de Ciências e Tecnologia
2025

CHARLOTTE WALTER

EFFECTS AND VARIABILITY OF DECLINE IN SEA ICE ON MARINE PRIMARY PRODUCTION IN THE ARCTIC

Master’s in Marine and Coastal Systems

Work performed under the supervision of:
Dr. Paulo Relvas
Dr. Annette Samuelsen

UNIVERSIDADE DO ALGARVE
Faculdade de Ciências e Tecnologia
2025

Declaração de autoria do trabalho
Declaro ser o(a) autor(a) deste trabalho, que é original e inédito. Autores e trabalhos consultados estão devidamente citados no texto e constam da listagem de referências incluída.

Statement of authorship
I declare to be the author of this work, which is original and unpublished. Authors and works consulted are duly cited in the text and included in the reference list.

Charlotte Walter

Acknowledgements

I would like to express my gratitude to Dr. Annette Samuelsen and Dr. Heather Regan at the Nansen Environmental and Remote Sensing Center (NERSC) Bergen, who offered me the opportunity to conduct this research project under their supervision during my internship. Their guidance and support throughout the development of this Master thesis was invaluable. I would also like to acknowledge that the HYCOM-neXtSIM-ECOSMO simulation analyzed in this study was run by Dr. Heather Regan.

Furthermore, I would like to thank Dr. Shuang Gao (NERSC), who ran the HYCOM-CICE-ECOSMO simulation analyzed in this study, and who always helped to answer my questions regarding the data output and analysis while writing these Master thesis.

I would like to thank Dr. Çağlar Yumruktepe (NERSC) for supporting me in creating a functional regional mask for data analysis in Python.

Finally, a last big ’thank you’ goes out to all the colleagues at NERSC, who made my research internship such an enjoyable and interesting learning experience, and to Dr. Paulo Relvas, who agreed to be my supervisor for this Master thesis at Universidade do Algarve.

Abstract

The Arctic environment is rapidly changing and drastic declines in sea ice extent and thickness have been observed over the past decades. The thinning of the ice pack affects its dynamics and makes it more susceptible to form pressure-ridges and leads. Such features appear at a scale of meters to kilometers, and are thus usually not represented in common Earth system models. However, observations show that their presence influences polar phytoplankton communities and productivity, pointing at the importance of representing such sea ice features in biogeochemical ocean modeling. The following study investigates how Arctic primary production and carbon export simulated with the biogeochemical model HYCOM-ECOSMO are affected by different sea ice models. Two simulations are available; one coupled to the classical Los Alamos sea ice model (CICE) that simulates sea ice as a continuum that deforms in a viscous manner. In contrast, the second simulation was run with the next generation sea-ice model (neXtSIM) with a brittle rheology that better represents features such as leads and ridges. Climatologies, daily time series and maps of monthly mean values for relevant parameters were analyzed for three Arctic regions. Differences in sea ice concentration resulting from the different rheologies caused differences in light availability and primary production between simulations in all regions. The different influx volumes of melt water and resulting stratification of the upper ocean affected primary production in two of three regions, and might have caused differences in nutrient availability between simulations. These findings suggest that the choice of sea ice model affects primary production modeling in HYCOM-ECOSMO to a certain extent. The results of this study contribute to the evaluation of whether the better representation of mechanical damage in sea ice models with brittle rheology can improve primary production and carbon export predictions from Arctic Ocean biogeochemical models.

Key words: Arctic Ocean primary production, biogeochemical modeling, carbon export, sea ice modeling, rheology

Resumo

O ambiente do Ártico está a mudar rapidamente. Reduções drásticas na extensão e espessura do gelo marinho têm sido observadas nas ultimas décadas. A diminuição de espessura da camada de gelo afeta sua dinâmica e torna-a mais suscetível à formação de cristas de pressão e fraturas (leads). Tais estruturas ocorrem em escalas de metros a quilômetros e, portanto, geralmente não são representadas nos modelos convencionais do sistema terrestre. No entanto, observações indicam que sua presença influencia as comunidades de fitoplâncton polar e sua produtividade, evidenciando a importância de representar essas características do gelo marinho na modelação biogeoquímica oceânica.

Para prever alterações na produção primária marinha e na exportação de carbono no Ártico, é essencial utilizar modelos oceânicos regionais acoplados a modelos de gelo marinho que simulem de forma realista as características do gelo e seus impactos sobre o crescimento do fitoplâncton. Contudo, a simulação de estruturas de fraturas pode ser computacionalmente onerosa, especialmente quando é necessário aumentar a resolução do modelo para representar essas estruturas à escala. Surge, então, a questão de saber se a simulação dessas estruturas em modelos de gelo marinho altera significativamente a modelação da produção primária quando acoplada a um modelo biogeoquímico.

Para investigar essa questão, o modelo biogeoquímico HYCOM-ECOSMO foi acoplado ao modelo clássico de gelo marinho de Los Alamos (CICE), que simula o gelo como um contínuo que se deforma de maneira viscosa. Para comparação, foi realizada uma segunda simulação com o modelo da próxima geração (neXtSIM), que utiliza uma reologia frágil e representa melhor estruturas como fraturas e cristas de pressão, mesmo sob a mesma resolução.

Climatologias, séries temporais diárias e mapas de valores médios mensais foram analisados para os seguintes parâmetros-chave: temperatura da superfície do mar, salinidade superficial, valores superficiais de nutrientes (silicato, nitrato e fosfato), profundidade da camada de mistura, valores de produção primária bruta integrados até 500 m de profundidade, concentração de gelo marinho e espessura do gelo marinho. A análise regional foi conduzida para o ano de baixo gelo marinho de 2012 e para o ano seguinte, 2013, nas regiões do Atlântico Ártico, Mar de Barents e Mar de Chukchi. O objetivo foi identificar diferenças na produção primária bruta entre as simulações e atribuí-las às diferenças nos parâmetros do gelo marinho, causadas pelas distintas reologias dos modelos de gelo.

A análise das regiões selecionadas mostrou que ambos os modelos simulam de forma distinta a espessura e a concentração do gelo marinho para o ano de 2012 em comparação com 2013. No Atlântico Ártico e no Mar de Chukchi, os valores mínimos de espessura e concentração do gelo foram menores em 2012. No Mar de Barents, a diferença entre os anos foi observada nos valores máximos desses parâmetros, que foram menores no verão de 2012 em ambas as simulações, em comparação com o verão de 2013.

A climatologia da concentração de gelo marinho indicou que o modelo neXtSIM simulou concentrações mais baixas em todo o domínio ártico em relação ao CICE. Isso era esperado, pois a reologia frágil do neXtSIM permite uma melhor simulação das estruturas de fraturas de pequena escala, mesmo sob a mesma resolução. Assim, a concentração de gelo no neXtSIM diminui mais com o aumento da área de águas abertas nas células da grelha, decorrente da abertura de fraturas.

O efeito das diferenças na concentração de gelo marinho sobre a disponibilidade de luz foi evidente em todas as regiões analisadas. O influxo de água de derretimento para o oceano superior e sua influência no afloramento afetaram a produção primária bruta integrada no Mar de Barents e na região do Atlântico Ártico. Além disso, a mistura mais profunda durante o inverno na região do Atlântico Ártico na simulação com neXtSIM pode ter sido parcialmente impulsionada pela maior espessura do gelo marinho, com efeito sobre a disponibilidade de nutrientes. Portanto, diferenças na reologia que influenciam a formação e o derretimento do gelo marinho podem impactar a modelação da produção primária no HYCOM-ECOSMO.

Os resultados deste estudo contribuem para a avaliação de se a melhor representação dos danos mecânicos em modelos de gelo marinho com reologia frágil pode melhorar as previsões de produção primária e exportação de carbono em modelos biogeoquímicos do Oceano Ártico. Isso avançará a compreensão sobre as incertezas relacionadas com o desempenho dos modelos oceânicos acoplados comumente utilizados no Ártico. Essas indicações podem ajudar a melhorar a fiabilidade das simulações regionais do Ártico e dos modelos do sistema terrestre, nos quais o Ártico desempenha um papel extraordinariamente influente.

Palavras-chave: Produção primária do Oceano Ártico, modelagem biogeoquímica, exportação de carbono, modelagem do gelo marinho, reologia do modelo do gelo marinho

Table of contents

Acknowledgements **iii**

Abstract **iv**

Resumo **v**

List of figures **ix**

List of tables **xiii**

List of abbreviations **xv**

1 Introduction **1**

2 Literature review **3**

2.1 Description of the Arctic domain 3
2.1.1 Geography and bathymetry 3
2.1.2 Arctic sea ice 3
2.1.3 Forcings 6
2.1.4 Vertical structure and water column properties 7
2.1.5 Inflow and circulation 9
2.1.6 Deep water formation and ventilation 12
2.1.7 Uncertainties and future predictions 12
2.2 Primary production and carbon export in the Arctic Ocean 13
2.2.1 Controlling factors of biomass production 13
2.2.2 Biological carbon pump 15
2.2.3 Trends and future predictions 15

3 Methods **17**

3.1 Fundamental background of sea ice modeling 17
3.2 Sea ice model comparison 18
3.2.1 Rheology 18
3.2.2 Sea ice thickness distribution 19

3.2.3 Material and radiation fluxes 20
3.3 HYCOM-ECOSMO coupling 21
3.4 Datasets and processing 23
3.5 Selected variables 25
3.6 Analysis methods 25

4 Results 27
4.1 Selection of study regions and target years 27
4.2 Climatologies of the Arctic domain 28
4.3 Barents Sea 30
4.4 Arctic Atlantic 37
4.4.1 Biogeochemical variables 37
4.4.2 Mixed layer depth 41
4.4.3 Sea ice variables 42
4.4.4 Summary of results 43
4.5 Chukchi Sea 43
4.5.1 Biogeochemical variables 45
4.5.2 Mixed layer depth 50
4.5.3 Sea ice variables 50
4.5.4 Summary of results 53

5 Discussion 55
5.1 Barents Sea 55
5.1.1 Ice-edge bloom 55
5.1.2 Magnitude of integrated GPP 56
5.2 Arctic Atlantic 57
5.2.1 Spring bloom and primary production magnitude 57
5.2.2 Light availability and sea ice parameters 58
5.2.3 Mixed layer depth and sea ice parameters 58
5.2.4 Concluding remarks 61
5.3 Chukchi Sea 61
5.3.1 Spring bloom and primary production magnitude 61
5.3.2 Light availability and sea ice parameters 61
5.3.3 Mixed layer depth and sea ice parameters 62
5.3.4 Missing peak production in neXtSIM 63
5.3.5 Concluding remarks 63
5.4 Carbon export 63
5.5 Synthesis of regional analysis 64

6 Conclusions 66

References **68**

List of figures

2.1 (a) Arctic Ocean bathymetry map showing the four main basins and other bathymetry and topographic features of the Arctic domain: AB = Amerasian Basin. AR = Alpha Ridge. EB = Eurasian Basin. FJL = Franz Josef Land. GR = Gakkel Ridge. GSR = Greenland-Scotland Ridge. LR = Lomonosov Ridge. LS = Lancaster Sound. MR = Mendeleev Ridge. NS = Nares Strait. SZ = Severnaya Zemlya. Note that the Barents Sea Opening, located between Svalbard and the northern Norwegian coastline is not labeled. (b) Map of the upper ocean circulation in the Arctic Ocean, showing warm Atlantic currents (red arrows), cold less saline polar and Arctic currents (blue arrows), and low salinity transformed currents (green arrows). The annual mean maximum ice extent is shown in blue and the annual minimum in red (late twentieth century conditions). The minimum in 2007, the second absolute minimum to date, is shown in dark red. AC = Anadyr Current. ACC = Alaskan Coastal Current. BC = Baffin Island Current. BIC = Bear Island Current. BG = Beaufort Gyre. EGS = East Greenland Current. EIC = East Iceland Current. ESC = East Spitsbergen Current. IC = Irminger Current. JMC = Jan Mayen Current. MC = Murman Current. NAD = North Atlantic Drift. NAC = Norwegian Atlantic Current. NCC = Norwegian Coastal Current. SB = Siberian branch (of the Transpolar Drift). SCC = Siberian Coastal Current. TPD = Transpolar Drift. WGC = West Greenland Current. WSC =West Spitsbergen Current. From Rudels & Carmack (2022), used under Creative Commons license BY 4.0. 4

2.2 Map of the pan-Arctic watershed (red line), showing the 6 largest catchments mentioned in this report. Red dots are indicative of their approximate discharge location into the Arctic Ocean. From Stubbins et al. (2015), used under Creative Commons license BY 4.0. 8

2.3 Typical vertical distribution of potential temperature (°C) and salinity for Nansen Basin (NB), Amundsen Basin (AB), Markarov Basin (MB) and Canada Basin (CB). PML indicates Polar Mixed Layer. Adapted from Rudels (2009). From Gonçalves-Araujo (2016), used with permission from the author. 9

4.1 Map of the Arctic domain, showing the extents of the selected study regions. . . 28

4.2 Climatologies of SST for the simulation period from 2007 to 2016, plotted for both simulations. 29

4.3 Climatologies of surface salinity for the simulation period from 2007 to 2016, plotted for both simulations. 29

4.4 Maps of integrated GPP rates (in mg C m^{-2} d^{-1}) in the Barents Sea from the neXtSIM-simulation for March to June 2012, plotted from monthly mean files. The White Sea is located approximately between 30 °E and 40 °E along the 65 °N latitude. 31

4.5 Difference maps (CICE minus neXtSIM) of integrated GPP rates (in mg C m^{-2} d^{-1}) in the Barents Sea for March to June 2012, plotted from monthly mean files. 32

4.6 Time series of SIT for 2012 to 2013 for both simulations, plotted as regional average from daily files. 32

4.7 Maps of SIC in the Barents Sea from the neXtSIM-simulation for March to June of both years, plotted from monthly mean files. The White Sea is located approximately between 30 °E and 40 °E along the 65 °N latitude. 33

4.8 Difference maps (CICE minus neXtSIM) of SIC in the Barents Sea for March to June 2012, plotted from monthly mean files. Red areas indicate higher SIC in CICE, blue areas indicate higher SIC in neXtSIM. The White Sea is located approximately between 30 °E and 40 °E along the 65 °N latitude. 34

4.9 Difference maps (CICE minus neXtSIM) of light limitation (integrated over 100 m) in the Barents Sea for March to June 2012, plotted from monthly mean files. Red areas indicate higher light availability in CICE, blue areas indicate higher light availability in neXtSIM. The White Sea is located approximately between 30 °E and 40 °E along the 65 °N latitude. 34

4.10 Maps of nitrate limitation (integrated over 100 m) in the Barents Sea from the neXtSIM-simulation for March to June in 2012, plotted from monthly mean files. Darker shading indicates higher nitrate availability. The White Sea is located approximately between 30 °E and 40 °E along the 65 °N latitude. 35

4.11 Maps of MLD (given in m depth) in the Barents Sea from the neXtSIM-simulation for January to June 2012, plotted from monthly mean files. The White Sea is located approximately between 30 °E and 40 °E along the 65 °N latitude. 36

4.12 Difference maps (CICE minus neXtSIM) of MLD in the Barents Sea for January to June 2012, plotted from monthly mean files. Red areas indicate a deeper mixed layer in CICE, blue areas indicate a deeper mixed layer in neXtSIM. The White Sea is located approximately between 30 °E and 40 °E along the 65 °N latitude. 36

4.13 Time series of integrated GPP rates (in mg C m^{-2} d^{-1}) in the Arctic Atlantic region for 2012 to 2013 for both simulations, plotted as regional average from daily files. 37
4.14 Maps of integrated GPP rates (in mg C m^{-2} d^{-1}) in the Arctic Atlantic region from the neXtSIM-simulation for March to June 2012, plotted from monthly mean files. 38
4.15 Time series of the light limitation factor (integrated over 100 m) In the Arctic Atlantic region for 2012 and 2013 for both simulations, plotted as regional average from daily files. Larger factors indicate lower levels of limitation. . . . 39
4.16 Maps of light limitation (integrated over 100 m) in the Arctic Atlantic region from the neXtSIM-simulation for March to June 2012, plotted from monthly mean files. Darker shading indicates higher light availability. 39
4.17 Difference maps (CICE minus neXtSIM) of light limitation (integrated over 100 m) in the Arctic Atlantic region for March to June 2012, plotted from monthly mean files. Red areas indicate higher light availability in CICE, blue areas indicate higher light availability in neXtSIM. 40
4.18 Time series of MLD in the Arctic Atlantic region for 2012 to 2013 for both simulations, plotted as regional average from daily files. 41
4.19 Maps of MLD (given in m depth) in the Arctic Atlantic region from the CICE-simulation for January to June 2013, plotted from monthly mean files. 42
4.20 Time series of SIC for 2012 to 2013 for both simulations, plotted as regional average from daily file. 43
4.21 Difference maps (CICE minus neXtSIM) of SIC in the Arctic Atlantic region for March to June 2012, plotted from monthly mean files. Red areas indicate higher SIC in CICE, blue areas indicate higher SIC in neXtSIM. 44
4.22 Time series of integrated GPP rates (in mg C m^{-2} d^{-1}) in the Chukchi Sea for 2012 to 2013 for both simulations, plotted as regional average from daily files. . 45
4.23 Maps of integrated GPP rates (in mg C m^{-2} d^{-1}) in the Chukchi Sea from the neXtSIM-simulation for March to June 2012, plotted from monthly mean files. 46
4.24 Time series of the light limitation factor (integrated over 100 m) in the Chukchi Sea for 2012 and 2013 for both simulations, plotted as regional average from daily files. Larger factors indicate lower levels of limitation. 47
4.25 Maps of light limitation (integrated over 100 m) in the Chukchi Sea from the CICE-simulation for March to June in 2012, plotted from monthly mean files. Darker shading indicates higher light availability. 47
4.26 Maps of light limitation (integrated over 100 m) in the Chukchi Sea from the neXtSIM-simulation for March to June in 2012, plotted from monthly mean files. Darker shading indicates higher nitrate availability. 48

4.27 Difference maps (CICE minus neXtSIM) of light limitation (integrated over 100 m) in the Chukchi Sea for March to June 2012, plotted from monthly mean files. Red areas indicate higher light availability in CICE, blue areas indicate higher light availability in neXtSIM. 48

4.28 Maps of nitrate limitation (integrated over 100 m) in the Chukchi Sea from the neXtSIM-simulation for March to June in 2012, plotted from monthly mean files. Darker shading indicates higher nitrate availability. 49

4.29 Difference maps (CICE minus neXtSIM) of nitrate limitation (integrated over 100 m) in the Chukchi Sea for March to June 2012, plotted from monthly mean files. Red areas indicate higher nitrate availability in CICE, blue areas indicate higher light availability in neXtSIM. 49

4.30 Time series of carbon export (in mol m$^{-2\ -1}$) at 300 m depth for both simulations, plotted as regional average from daily files. 50

4.31 Time series of MLD in the Chukchi Sea for 2012 to 2013 for both simulations, plotted as regional average from daily files. 51

4.32 Maps of MLD (given in m depth) in the Chukchi Sea from the neXtSIM-simulation for January to June 2012, plotted from monthly mean files. 51

4.33 Difference maps (CICE minue neXtSIM) of SIT in the Chukchi Sea for March to June of both years, plotted from monthly mean files. Red areas indicate thicker ice in CICE, blue areas indicate thicker ice in neXtSIM. 52

4.34 Maps of SIC in the Chukchi Sea from the neXtSIM-simulation for March to June of both years, plotted from monthly mean files. 53

4.35 Maps of SIC in the Chukchi Sea from the CICE-simulation for March to June of both years, plotted from monthly mean files. 54

5.1 Maps of integrated GPP rates (in mg C m^{-2} d^{-1}) in the Arctic Atlantic region from the CICE-simulation for March to June 2012, plotted from monthly mean files. 59

5.2 Maps of light limitation (integrated over 100 m) in the Arctc Atlantic region from the CICE-simulation for March to June in 2013, plotted from monthly mean files. Darker shading indicates higher light availability. 60

5.3 Difference maps (CICE minus neXtSIM) of surface salinity in the Arctic Atlantic region for January to June 2012, plotted from monthly mean files. Red areas indicate higher surface salinity in CICE, blue areas indicate higher surface salinities in neXtSIM. 60

List of tables

3.1 Comparison of simulation set-up and overview of key differences between the sea ice models used in this study. 23

4.1 R-values from linear regression analysis for integrated GPP for ArcAtl, using the light limitation factor as predictor variable (all p-values < 0.0001). 40

4.2 R-values from linear regression analysis for integrated GPP for Chukchi Sea, using the SIC as predictor variable (all p-values < 0.0001). 54

List of abbreviations

AB	Amerasian Basin
ACC	Alaskan Coastal Current
AC	Anadyr Current
ArcAtl	Arctic Atlantic
AR	Alpha Ridge
BC	Baffin Island Current
BCP	Biological carbon pump
BBM	Brittle Bingham-Maxwell
BG	Beaufort Gyre
BIC	Bear Island Current
CB	Canada Basin
CDO	Climate Data Operators
CHL *a*	Chlorophyll *a*
CHS	Chukchi Sea
CICE	Los Alamos sea ice model
DOC	Dissolved organic carbon
DOM	Dissolved organic matter
EB	Eurasian Basin
ECMWF	European Centre for Medium-Range Weather Forecasts
ECOSMO	ECoSystem MOdel

EGC	East Greenland Current
EGS	East Greenland Current
EIC	East Iceland Current
ERA	ECMWF Re-Analysis
ESC	East Spitsbergen Current
EU	European Union
EVP	Elastic-viscous-plastic
FJL	Franz Josef Land
GPP	Gross primary production
GR	Gakkel Ridge
GSR	Greenland-Scotland Ridge
HYCOM	Hybrid Coordinate Ocean Model
IC	Irminger Current
JMC	Jan Mayen Current
LR	Lomonosov Ridge
LS	Lancaster Sound
MB	Markarov Basin
MC	Murman Current
MLD	Mixed layer depth
MR	Mendeleev Ridge
MIZ	Marginal ice zone
NAC	Norwegian Atlantic Current
NAD	North Atlantic Drift
NAO	North Atlantic Oscillation
NB	Nansen Basin
NCC	Norwegian Coastal Current

NCO	netCDF Operator
NEMO	Nucleus for European Modelling of the Ocean
NERSC	Nansen Environmental and Remote Sensing Center
NOAA	United States National Oceanic and Atmospheric Administration
NS	Nares Strait
NSIDC	United States National Snow and Ice Data Center
NPP	Net primary production
PAR	Photosynthetically active radiation
PISCES	Pelagic Interactions Scheme for Carbon and Ecosystem Studies
PML	Polar Mixed Layer
POC	Particulate organic carbon
PP	Primary production
SB	Siberian branch (of the Transpolar Drift)
SCC	Siberian Coastal Current
SIC	Sea ice concentration
SIMBA	Sea Ice Model for Bottom Algae
SIT	Sea ice thickness
SST	Sea surface temperature
SZ	Severnaya Zemlya
TOP	Tracers in Ocean Paradigm
TPD	Transpolar Drift
WOA	World Ocean Atlas
WGC	West Greenland Current
WSC	West Spitsbergen Current

Chapter 1

Introduction

The Arctic environment is observed to warm much faster than the rest of the globe, a phenomenon that is referred to as Arctic Amplification. The most drastic estimates suggest that the region warms four times faster than the rest of the world, which strongly affects the terrestrial and marine environment (Rantanen et al., 2022). In 2024, the Arctic Ocean sea ice extent was reported as the 6th-lowest in the past 45 years of available satellite observations, following a long-term negative trend (Meier et al., 2024). Records of average winter sea ice thickness show a decrease from 3.6 m in the 1980s down to currently 2 m, which has been largely attributed to a loss of usually thicker multi-year ice, which is ice that survives at least one summer season (Regan et al., 2023; Timmermans & Marshall, 2020). At the same time, satellite observations show that the Arctic Ocean net primary production has increased by 57 % since 1998, and this positive trend is expected to continue during the next decades (Lewis et al., 2020; Timmermans & Marshall, 2020).

The regime change towards a thinner and more seasonal ice pack in the Arctic affects its dynamics. The sea ice becomes more susceptible to form fractal features such as leads and ridges at scales of meters to kilometers, and larger openings called polynyas. Observations have shown that these pack ice features influence polar phytoplankton communities and productivity, because sea ice properties alter light availability and vertical mixing processes (Arrigo & Van Dijken, 2003; Fernández-Méndez et al., 2018).

To predict changes in Arctic marine primary production and carbon export, it is therefore essential to run Arctic Ocean models that realistically simulate sea ice characteristics and their impacts on phytoplankton growth. However, simulating fractal features can be computationally expensive when the model resolution has to be increased in order to simulate these features at scale. Hence, the question arises whether the simulation of these features does in fact influence the modeling of primary production when coupled to a biogeochemical model.

To investigate this question, two available model simulations that were run with with different sea ice rheologies were compared. In the first simulation, the biogeochemical model HYCOM-ECOSMO was coupled to the classical Los Alamos sea ice model (CICE) that simulates sea ice as a continuum that deforms in a viscous manner. The second simulation was run with the next generation sea ice model (neXtSIM) with a brittle rheology that better represents features such as leads and ridges when run at the same resolution. In the following study, the model output will be analyzed and compared, with the objective to understand whether the differences in sea ice rheology affect primary production and carbon export simulated in HYCOM-ECOSMO. The study will help to assess whether employing a sea ice model that better represents mechanical damages of the sea ice cover results in significant differences in primary production and carbon export within a coupled biogeochemical model. This will advance the understanding about uncertainties related to the performance of commonly employed coupled ocean models in the Arctic.

Chapter 2

Literature review

2.1 Description of the Arctic domain

2.1.1 Geography and bathymetry

The Arctic Ocean is the smallest of the global ocean, which holds approximately 1 % of the world's oceanic water volume (Timmermans & Marshall, 2020). It is centered over the North Pole and surrounded by land and shallow channels that create connections with the Pacific and Atlantic oceans. A map of the Arctic Ocean is provided in Fig. 2.1(a) (Rudels & Carmack, 2022). Its geographical location makes the Arctic Ocean an environment of extreme seasonal variability, with complete lack of sunlight during polar night vs. extensive light availability during the summer months. As approximately 50 % of the ocean basin are very shallow shelf regions, the influence of the radiation on the water column properties and biological processes is amplified during the polar day (Rudels & Carmack, 2022).

As seen in Fig. 2.1(a), the shallow seas along the continental slopes are named after their geographical locations, and range in mean depth between 50 m and 200 m (Rudels & Carmack, 2022). Note that in some studies the Northwestern Passages are called Canadian Arctic Archipelago. The Arctic deep basin has a mean depth of 4000 m and is separated by the Lomonosov Ridge into the Eurasian and Amerasian basins (Timmermans & Marshall, 2020). These are further subdivided into Amundsen and Nansen basins, and the Makarov and Canada basins (see Fig. 2.1(a)).

2.1.2 Arctic sea ice

Sea ice covers large areas of the Arctic Ocean and strongly mediates the ocean-atmosphere exchange of energy, mass and momentum, thereby affecting stratification, circulation and biological processes (Meier et al., 2024). The Arctic sea ice extent, defined as total area of ice with a sea ice concentration (SIC) larger than 15 % is subject to a strong seasonal cycle (Meier et al., 2024). Its summer minimum extent occurs in September, which in recent years has been approximately

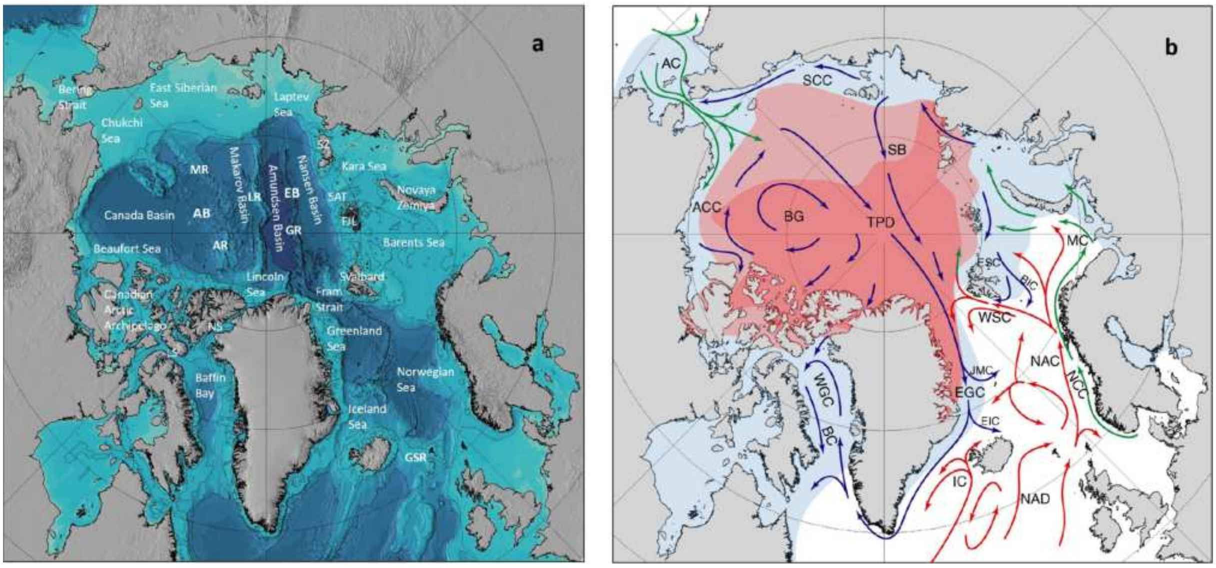

Figure 2.1: (a) Arctic Ocean bathymetry map showing the four main basins and other bathymetry and topographic features of the Arctic domain: AB = Amerasian Basin. AR = Alpha Ridge. EB = Eurasian Basin. FJL = Franz Josef Land. GR = Gakkel Ridge. GSR = Greenland-Scotland Ridge. LR = Lomonosov Ridge. LS = Lancaster Sound. MR = Mendeleev Ridge. NS = Nares Strait. SZ = Severnaya Zemlya. Note that the Barents Sea Opening, located between Svalbard and the northern Norwegian coastline is not labeled. (b) Map of the upper ocean circulation in the Arctic Ocean, showing warm Atlantic currents (red arrows), cold less saline polar and Arctic currents (blue arrows), and low salinity transformed currents (green arrows). The annual mean maximum ice extent is shown in blue and the annual minimum in red (late twentieth century conditions). The minimum in 2007, the second absolute minimum to date, is shown in dark red. AC = Anadyr Current. ACC = Alaskan Coastal Current. BC = Baffin Island Current. BIC = Bear Island Current. BG = Beaufort Gyre. EGS = East Greenland Current. EIC = East Iceland Current. ESC = East Spitsbergen Current. IC = Irminger Current. JMC = Jan Mayen Current. MC = Murman Current. NAD = North Atlantic Drift. NAC = Norwegian Atlantic Current. NCC = Norwegian Coastal Current. SB = Siberian branch (of the Transpolar Drift). SCC = Siberian Coastal Current. TPD = Transpolar Drift. WGC = West Greenland Current. WSC =West Spitsbergen Current. From Rudels & Carmack (2022), used under Creative Commons license BY 4.0.

one third of the winter extent. Winter sea ice is characterized by an average thickness of 2 m and its maximum extent occurs in March (Timmermans & Marshall, 2020). The map in Fig. 2.1(b) shows the annual mean maximum and minimum sea ice extent in blue and red respectively, representing late twentieth century conditions, and the second absolute minimum that occurred in 2007 in dark red (Rudels & Carmack, 2022).

Sea ice starts to form when the sea surface temperature (SST) reaches below the freezing point of sea water at -1.8 °C (NSIDC, 2025). The first ice crystals, called frazil, accumulate and freeze together, eventually forming a thin ice cover or ice floes. Sea ice thickness increases through the formation of ice crystals at the bottom of the ice surface, a process that is called congelation. Through this, first-year ice (or seasonal ice) can reach a sea ice thickness (SIT) of up to 2 m (Australian Antarctic Division, 2017). All first-year ice that survives one summer will be classified as multi-year ice. Whether or not the first-year ice melts completely depends on its initial thickness at the start of spring, SIC, and the spatial and temporal differences in summer conditions (NSIDC, 2025).

The term pack ice summarizes all forms of ice that are mobile and can be moved by winds and currents. The marginal ice zone (MIZ) appears where pack ice transitions into open water, is usually defined as area of SIC below 85 %, and is know to be a highly productive region (Sundfjord et al., 2008). If the ice sheet is attached to a shore line, it is referred to as landfast ice, where it can either form through in-situ freezing, or through the attachment of drifting pack ice to the coast (Australian Antarctic Division, 2017). The thickness of the sea ice and the ratio of open water in the pack ice strongly influence the light flux into the upper ocean, and therefore strongly affect phytoplankton growth.

Sea ice properties change over time. Salinity decreases with sea ice age due to brine formation and ejection. Brine is formed when droplets of highly saline water accumulate during the formation of frazil ice, and remains liquid due to its high salinity. The brine is either expelled into the ocean or gets trapped in brine pockets between the ice crystals, which causes young ice to have a high salinity content. Over time and aided by gravity, the brine is ejected into the ocean and leaves air pockets in the ice. Brine release can be triggered by different processes: (1) The compression of sea ice can break the brine pockets; (2) fresh water that accumulates in melt ponds at the sea ice surface can flush out the brine when draining through cracks and openings in the ice sheet; (3) the cooling of the ice surface in winter can increase the brine's salinity to a level that is sufficient to melt the surrounding ice and release the brine at the bottom of the ice sheet (NSIDC, 2025). Brine is also formed and ejected during congelation. The influx of saline brine changes the stratification of the upper ocean during ice formation and enhances vertical mixing. In contrast, sea ice melt introduces fresher water into the water column, which enhances stratification and can promote mixed layer shoaling. Through this, sea ice influences nutrient availability and phytoplankton distribution in the water column, and eventually the biomass production.

Older multi-year ice tends to be thicker than younger ice, because congelation and ridge formation increase the ice thickness over time (Maslanik et al., 2007). Ridges form when ice sheets of a certain thickness collide or bend from convergence, which creates elongated piles of fractured ice (NSIDC, 2025). The total thickness of these ridge features can in extreme cases be up to 20 m, and is a combination of the smaller surface ridge, called sail, with a height of up to 2 m, and a keel at the bottom of the ice sheet that can reach down several meters (NSIDC, 2025).

The sea ice age and associated formation of ridges change the surface properties of multi-year ice and affect its albedo (i.e. reflectiveness). Multi-year sea ice tends to have a thicker snow cover compared to first-year ice, because of longer accumulation times or redistribution during ridge formation (Krumpen et al., 2025). Although the albedo of the snow cover is independent of thickness, the thicker snow layer delays the formation of melt ponds, which will eventually lower the albedo of the ice surface significantly. The rugged topography of multi-year ice further restricts the spatial extent of melt ponds and therefore dampens their effect on the albedo of multi-year ice compared to first-year ice (Krumpen et al., 2025). Therefore, the radiation influx to seasonal ice compared to multi-year ice is much higher. In combination with the observed thinning of the ice pack, this effect is anticipated to increase the overall heat input to the upper ocean through young and thin ice (Perovich & Polashenski, 2012).

The energy absorption by the upper ocean is furthermore altered by openings in the pack ice. Leads are narrow, linear openings that form by divergence or shear of ice floes. Their width typically ranges between meters and tens of kilometers, and they can form extended networks of several hundreds of kilometers (NSIDC, 2025). The ocean can absorb additional heat from the atmosphere through these short-lived openings in the sea ice, which can enhance the sea ice melt in the surrounding areas. Their fast refreezing in winter contributes to the Arctic ice production (Qu et al., 2024). Independent of the season, leads can also be closed through continuous movement of ice floes driven by wind and currents (NSIDC, 2025).

Polynyas are open water features that are larger and more persistent than leads. They can prevail for periods of weeks to months and appear in sizes of tens to tens of thousands of square kilometers. They typically reoccur in the same location every year (Barber & Massom, 2007). Polynyas can form in the the open ocean, but often appear as coastal polynyas between landfast ice and pack ice (NSIDC, 2025).

Satellite-derived observations starting in the 1980s have revealed a continuous decline in multi-year ice coverage in the Arctic Ocean. The fraction of total ice extent of multi-year ice in March was 45 % in 2011 compared to 75 % in the mid-1980s (Maslanik et al., 2011). This trend has been associated with the overall decline in average sea ice thickness in the Arctic Ocean, and correlates with a volume decrease of the Arctic sea ice from 17,800 km^3 to 14,300 km^3 between 1980 and 1999 (Rudels & Carmack, 2022). As pointed out by Rheinlænder et al. (2022), the observed loss of thick multi-year ice and the corresponding decrease in overall thickness negatively affect the overall stability of the Arctic ice pack. The sea ice becomes increasingly mobile and more susceptible to be fractured by intense atmospheric forcing. This does not only alter the exchange processes at the ocean-atmosphere interface, but may also amplify the observed trends of decreasing minimum sea ice extent (Rheinlænder et al., 2022).

2.1.3 Forcings

A major external driver of water column properties and circulation is **atmospheric forcing through wind**. Ekman transport dominates the upper ocean circulation and causes down-welling across most of the Arctic, while the Nordic seas (Greenland, Iceland and Norwegian Sea) are mostly influenced by upwelling (Timmermans & Marshall, 2020). Two major wind patterns exist over the Arctic. The Beaufort High over the Amerasian Basin is driving the anticyclonic Beaufort Gyre with a radius of approximately 400 km. It is the largest circulation pattern and captures most of the freshwater influx in the Amerasian Basin (Rudels & Carmack, 2022; Timmermans & Marshall, 2020). The Icelandic Low over the North Atlantic introduces cyclonic tendencies, and the interaction of those two wind patterns drives the Transpolar Drift (TPD), which carries sea ice and water from the coast of Siberia across the Arctic. As can be seen on the map in Fig. 2.1(b), the TPD is a major export pathway towards the North Atlantic along the east coast of Greenland (Timmermans & Marshall, 2020).

Radiation fluxes are another important atmospheric forcing in the Arctic domain. SST in winter, and year-round underneath the sea ice is at freezing temperature (i.e. below -1.8 °C) (NSIDC, 2025). In areas without sea ice, or where the ice pack opens as leads or polynyas, solar radiation alters the heat budget of the upper ocean. This effect is especially strong during the spring and summer months when atmospheric temperatures are above 0 °C. This additional heat in the water column enhances the melt of proximal sea ice masses and thus affects the freshwater budget of the upper ocean (Timmermans & Marshall, 2020). Snow cover and melt water ponds on the sea ice affect its albedo and alter radiation fluxes through sea ice, as discussed before in Section 2.1.2.

As summarized by Timmermans & Marshall (2020), the **freshwater influx** to the Arctic Ocean is driven by three main sources: (1) Approximately 50 % of freshwater inflow is released from the main Arctic river catchments of the rivers Ob, Yenisey, Lena, Kolyma, Yukon and Mackenzie. The extent of their catchments and approximate location of inflow to the Arctic Ocean are shows on the map in Fig. 2.2 (Stubbins et al., 2015). Their freshwater contribution makes up approximately 10 % of the global river inputs into the oceans, which is a disproportionally large percentage considering the size of the Arctic Ocean. Seasonal variations in radiation influence the melt of terrestrial ice masses and alter the river flow volumes, which leads to variations in terrestrial freshwater and nutrient discharge into the Arctic Ocean. (2) Around one quarter of freshwater input is caused by net precipitation due to the global-scale atmospheric transfer of water vapor from lower to higher latitudes. (3) The remaining 25 % are contributed from the Pacific inflow, which is much fresher compared to the Atlantic inflow. On a basin-wide scale, only a small percentage of freshwater influx is derived from sea ice melt.

2.1.4 Vertical structure and water column properties

The Arctic Ocean is a so-called β-ocean, which means its stratification is salinity-driven. Freshwater inputs from the sources mentioned in Section 2.1.3 lead to the formation of a relatively cold and low salinity Polar Mixed Layer (PML), which has an average thickness of 50 m (Jones, 2001). As shown by the representative vertical temperature and salinity profiles in Fig. 2.3, the freshness of the PML, and also the thickness of the halocline underneath it vary between basins (Gonçalves-Araujo, 2016). For example, the salinity profile for the Canada Basin clearly shows the influence of the influx of the fresher Pacific water through the Bering Strait on upper ocean salinity and halocline depth.

The cold halocline is separating the mixed layer from the Atlantic Layer. This water mass resides at depths between 200 m and 500 m. As can be seen in the temperature vertical profiles in Fig. 2.3, the Atlantic water can be identified by the temperature maximum it creates in the

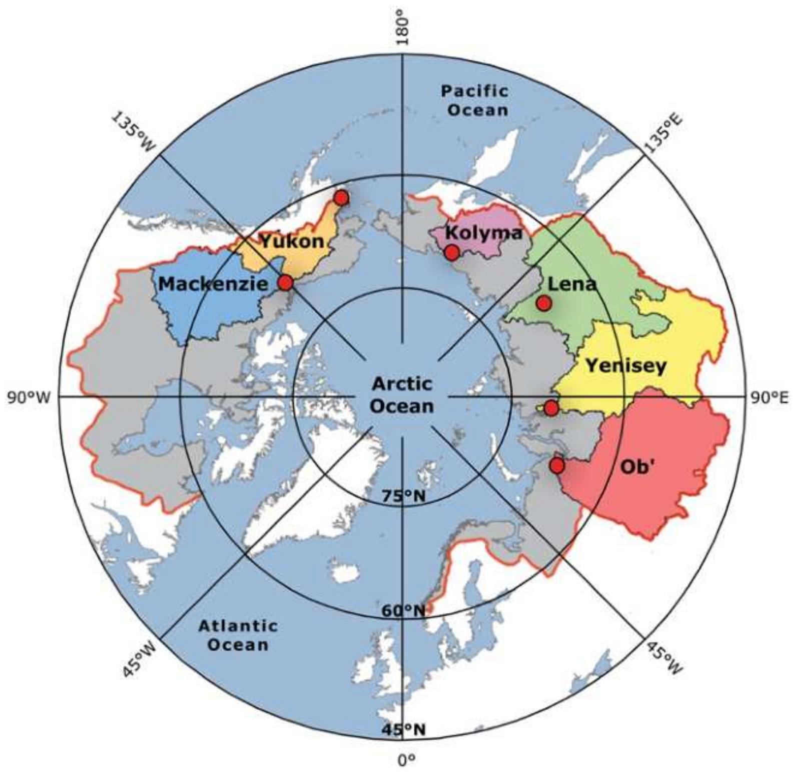

Figure 2.2: Map of the pan-Arctic watershed (red line), showing the 6 largest catchments mentioned in this report. Red dots are indicative of their approximate discharge location into the Arctic Ocean. From Stubbins et al. (2015), used under Creative Commons license BY 4.0.

water column. These temperature maxima range between approximately 2 °C in the Eurasian Basin (Nansen and Amundsen basins), and 0.5 °C in the Canada and Markarov basins (Jones, 2001). Below the Atlantic Layer reside the Upper Polar Deep Water, which extends to an average depth of 1700 m, a deep water layer extending to a depth of 2500 m, and the Arctic bottom water beneath (Jones, 2001).

The mixing processes in the water column and their drivers differ between water masses. The main external drivers of deepening and shoaling of the mixed layer are wind forcing and freshwater flux from sea ice melt and formation (Rudels & Carmack, 2022). During winter, the upper ocean becomes more homogeneously saline from brine ejection during ice formation, and despite the mediating presence of sea ice, strong wind forcing can enhance the deepening of the mixed layer through openings in the pack ice. During summer, the melt of sea ice introduces additional fresh water at the top of the ocean, which intensifies the halocline and prevents deeper mixing. The water column remains strongly stratified during the summer months despite the increase in area of open water that can be affected by wind, and despite smaller ice floes of higher mobility (Rudels & Carmack, 2022).

The deeper water layers are shielded from the influence of energy input at the surface, but are affected by other mixing processes. Where tidal forcing interacts with bathymetry features, internal waves can be triggered. Furthermore, diffusive-convective processes have been observed to create thermo-haline staircases. These form because of the unstable temperature

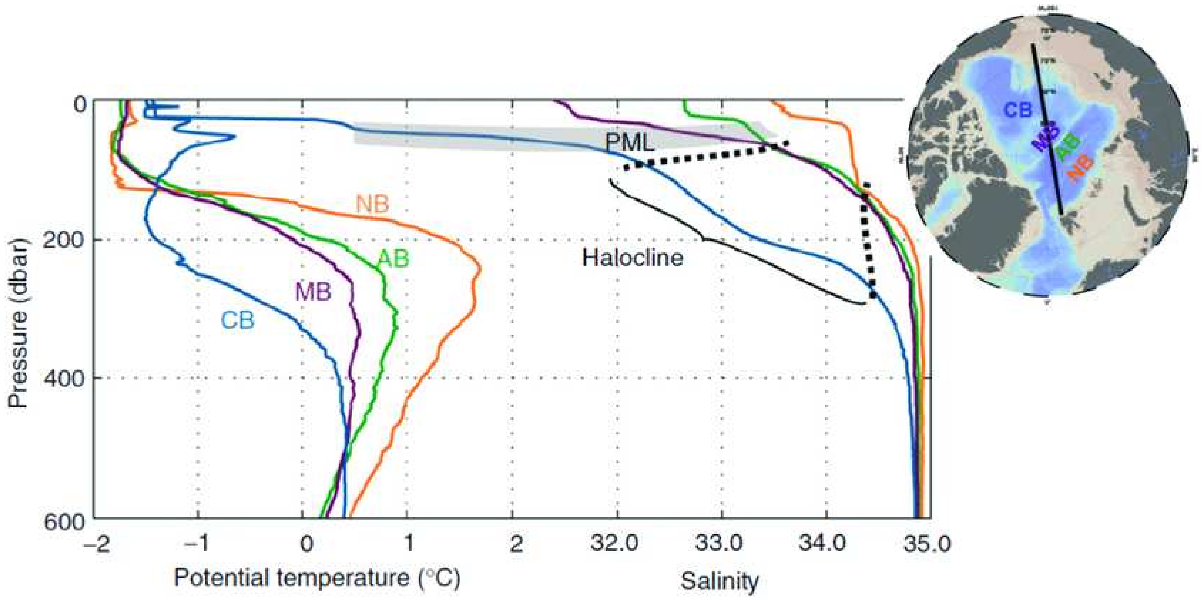

Figure 2.3: Typical vertical distribution of potential temperature (°C) and salinity for Nansen Basin (NB), Amundsen Basin (AB), Markarov Basin (MB) and Canada Basin (CB). PML indicates Polar Mixed Layer. Adapted from Rudels (2009). From Gonçalves-Araujo (2016), used with permission from the author.

stratification of the warmer Atlantic water residing below the colder surface water, which can create diffusive interfaces that bring saline water to the top. This creates local salinity instabilities which eventually leads to convective mixing (Rudels & Carmack, 2022). Although diffusive-convective processes are mostly associated with vertical mixing, horizontal mixing via intrusions and eddies has also been observed throughout the Arctic (Rudels & Carmack, 2022).

2.1.5 Inflow and circulation

The largest water fluxes at the Arctic Ocean's boundaries appear on the side of the Atlantic Ocean, through the deep Fram Strait (2600 m depth) located between Greenland and Svalbard, and the shallow Barents Sea Opening (200 m depth) (see map in Fig. 2.1(a)) (Rudels & Carmack, 2022). The water influx is driven by the Norwegian Atlantic Current (NAC), the northern extension of the Gulf Stream and North Atlantic Drift (NAD), which carries warm and relatively saline water into the Arctic Ocean and forms the Atlantic Layer in the water column. As can be seen in 2.1(b), the NAC splits into two branches along topographic features. One branch continues through Fram Strait west of Svalbard as the West Spitzbergen Current (WSC). Approximately half of the transported water volume enters the Arctic and encounters sea ice north of Svalbard, as shown by the green branch of the WSC in Fig. 2.1(b). This leads to a cooling of the upper layer of the Atlantic water, because a fraction of its heat is used to melt the present sea ice. The meltwater contributes to the formation of the PML, which isolates the warm and saline Atlantic water from the sea ice at the surface, and limits the Atlantic Layer's heat transfer to the atmosphere (Rudels & Carmack, 2022). The other half of the Atlantic water in the WSC does not enter the central

Arctic Ocean and recirculates inside the Fram Strait. As shown in the map in Fig. 2.1(b), it joins the southward-bound East Greenland Current (EGC) that carries cooler and fresher Arctic water. This exchange flow inside the Fram Strait was estimated to create a net southward transport of several Sverdrup (Timmermans & Marshall, 2020).

The second branch of the NAC flows into the Barents Sea and keeps its southern extent largely ice free throughout the year (Rudels & Carmack, 2022). Once it reaches the northern Barents and Kara seas, the inflow water has already cooled down significantly and carries less energy. Therefore, it induces less sea ice melt, and the formed surface layer is less fresh compared to the regions closer to the gateways (Rudels & Carmack, 2022). Despite the higher volume transport through the deep Fram Strait, observations indicate that heat influx from the Atlantic into the Arctic Ocean is higher through the Barents Sea Opening (Timmermans & Marshall, 2020).

The warm Atlantic Layer beneath the PML circulates as main current of the Arctic Ocean. It is also referred to as Arctic Circumpolar Boundary Current and describes a cyclonic pathway along the continental slopes of the Eurasian Basin, before it penetrates into the Makarov and Canada basins. Here it continues its cyclonic path, visibly following the isobaths of the continental slopes (Timmermans & Marshall, 2020). During its anti-clockwise flow, the Atlantic Layer loses all its heat before exiting the Arctic through the Fram Strait (Rudels & Carmack, 2022). Whether this circulation is caused by drivers inside or outside the domain remains under discussion: the first models of Arctic circulation adopted a so-called estuary framework of solely buoyancy-driven circulation, and only account for wind as driver of mixing processes in the upper and intermediate water layers. Other models simulate the circulation as wind-driven flow along potential vorticity contours that coincide with the isobath contours of the basin (Timmermans & Marshall, 2020).

Variability in the heat flux at the Fram Strait has been associated with the North Atlantic Oscillation (NAO), which arises from changes in the pressure gradient between the Azores High and the Icelandic Low and drives changes in regional wind patterns (Wang et al., 2019). An increasing heat flux into the Arctic has been detected during NAO positive phases through the intensification of SST gradients and volume transport inside the NAC (Flatau et al., 2003). At the same time, an increase in westerly winds during NAO positive phases can drive ocean-heat loss to the atmosphere in the sub-polar North Atlantic, which reduces heat availability at the Arctic Ocean boundaries (Fan et al., 2023). Although trends in volume influx are difficult to quantify due to a lack of observational data, measurable indicators of so-called Atlantification have been recorded. These include a reduction of sea ice and enhanced Atlantic Layer heat flux northeast of the Eurasian Basin due to poleward expansion of Atlantic water (Årthun et al., 2025; Timmermans & Marshall, 2020). Model predictions show that the Eurasian Basin could be completely filled with Atlantic water by 2070, which corresponds to an expected decrease of SIT by approximately 1.2 m, and an average ocean-ice heat flux increase by up to 5 W/m^2. The associated sea ice loss will further lead to increased mixing through wind, which is expected to have an amplifying feedback on the Atlantic water inflow and further drive sea ice melt. However, the stronger stratification of the upper ocean due to meltwater may have a counteracting effect on the mixing (Timmermans & Marshall, 2020).

Pacific water enters the Arctic Ocean into the Chukchi Sea through the narrow and shallow Bering Strait along the border between the United States and Russia (see map in Fig. 2.1(a)). The Pacific inflow is significantly fresher compared to the Atlantic inflow waters. This difference in salinity is mainly caused by the large scale atmospheric transport of evaporated water from the Atlantic to the Pacific (Timmermans & Marshall, 2020).

Differences in oceanic pressure between Pacific and Arctic Ocean as well as regional wind forcing have been discussed as the primary drivers of the flow and its variability through the Bering Strait. The origin of the steric height difference remains under discussion. It is thought to either be attributable to the differences in salinity between Pacific and Arctic waters, or may be caused by global wind patterns (Woodgate, 2018). Furthermore, the Alaska Coastal Current (ACC) was estimated to add approximately 10 % to the annual mean flow through the Bering Strait. Despite its very seasonal and small volume contribution, Woodgate et al. (2006) estimate that the ACC can increase the annual mean heat flux by approximately 30 %, and the annual mean freshwater influx by approximately 25 %. Due to low availability of observational data, it remains difficult to explain and predict the seasonal and inter-annual variability and trends of fluxes in the Bering Strait. Based on measurements from four moorings during the period of 1990 to 2015, Woodgate (2018) detected an increase in annual influx of Pacific water into the Arctic and propose that this positive trend in summer flow may be driven by far-field forcing (i.e. wind). Furthermore, a general increase in heat transport through the Bering Strait has been detected and is associated with the increasing volume flux (Serreze et al., 2019). The inflow of the less saline Pacific water contributes to the maintenance of the regional halocline and thus to the isolation of the Atlantic Layer from the sea surface and sea ice in the Canada and Markarov basins (Timmermans & Marshall, 2020). Furthermore, through the transformation and circulation of water masses inside the Arctic Ocean, the Pacific inflow plays a key role in restocking the freshwater budget of the Atlantic Ocean via export through the Canadian Arctic Archipelago and the Fram Strait (Jones, 2001; Rudels & Carmack, 2022).

The variability of volume and heat fluxes from the Atlantic and Pacific Ocean can exert a strong influence on various processes. Changes in heat fluxes can affect the strength and timing of sea ice melt, and may delay its formation in consecutive years when forming an uncommon heat reservoir in the ocean (Serreze et al., 2019). The associated changes in freshwater input from sea ice melt, together with changes in volume influx especially from the fresher Pacific Ocean can affect the upper ocean stratification. Furthermore, changes in volume fluxes can affect the advection of nutrients and micro-organisms, creating implications for biogeochemical processes trophic interactions (Rudels & Carmack, 2022; Woodgate, 2018).

2.1.6 Deep water formation and ventilation

The processes of Arctic deep water formation and ventilation remain under discussion. During winter, significant cooling and increasing salinity due to brine ejection from sea ice freezing enhance the sinking of surface water masses. As mentioned above, this leads to the formation of the intermediate Atlantic Layer, and is a driver of the Arctic Overturning Circulation. Especially in the shallow shelf regions, this Atlantic intermediate layer can be an important source of deep water ventilation via density-flows down the continental slope (Björk & Winsor, 2006; Jones et al., 1995).

A second pathway of deep water formation is thought to be the Atlantic inflow into the Barents Sea during winter. The inflow water cools down and becomes more saline due to brine ejection from sea ice formation, and sinks down the Saint Anna trough with only little entrainment (Rudels & Carmack, 2022). Furthermore, direct deep water fluxes between the Nordic seas and the Arctic Ocean are possible via the Fram Strait due to its sill depth of 2600 m (Björk & Winsor, 2006). However, this and other bathymetry features can also isolate deep water at lower depth from being ventilated and circulated beyond basin boundaries, and restricts their export from the Arctic Ocean (Jones et al., 1995). Lastly, the significant winter deepening of the PML can contribute to the ventilation and renewal of deep water masses. This is especially the case in the Labrador, Irminger and Greenland seas, where the mixed layer was observed to reach depth of 1000 m (Bretones et al., 2022).

2.1.7 Uncertainties and future predictions

As pointed out by Rudels & Carmack (2022), predicting the changes in Arctic Ocean stratification, circulation and mixing remains difficult due to the strong inter-linkage of, and uncertainties related to the evolution of their influencing factors. However, the overall freshwater influx to the Arctic is expected to increase with permafrost thaw, changes in precipitation patterns, increasing river inflows and sea ice melt. The effects are expected to be spatially heterogeneous, and the residence time and relative export of freshwater will determine the overall freshwater budget of the Arctic Ocean (Rudels & Carmack, 2022; Timmermans & Marshall, 2020). The freshwater-related strengthening of the halocline is expected to weaken vertical mixing and further limit the heat and material fluxes between water masses in the Arctic Ocean (Rudels & Carmack, 2022). At the same time, the retreat, thinning and associated decrease in stability of the sea ice may have a counteracting effect, allowing for more wind-driven energy input into the upper ocean. In this scenario, the deep winter mixing is expected to propagate further north following the sea ice retreat (Bretones et al., 2022). Furthermore, where the MIZ retreats behind the shelf break upwelling may intensify, which would increase mixing and nutrient availability for primary production (Rudels & Carmack, 2022). This effect may be counteracted locally in shallow areas, where the Arctic Ocean may become temperature-stratified. The expected increase in heat absorption by the upper ocean may influence the rates and timing of sea ice melt and refreezing, an effect that is further enhanced by the increasing formation of leads and other fractal features (Timmermans & Marshall, 2020).

2.2 Primary production and carbon export in the Arctic Ocean

2.2.1 Controlling factors of biomass production

Arctic Ocean primary production (PP), which is the production of organic carbon by phytoplankton (i.e. micro-algae) via photosynthesis, creates the foundation of the Arctic Ocean's foodweb and is a key mechanism of carbon fixation (Castellani et al., 2017; Frey et al., 2024). Gross primary production (GPP) is the total amount of produced organic carbon by this process, while net primary production (NPP) represents the amount of carbon available for cell growth after respiration by its producing organisms (Westberry et al., 2023).

Phytoplankton occurs in different realms of the Arctic Ocean, in open water, underneath the sea ice and inside or attached to the bottom of the sea ice. These ice algae are mainly confined to the network of brine channels and can be ejected to the open ocean during sea ice melt (Castellani et al., 2017). It has been estimated that ice algae make up around 60 % of the total primary production in the Arctic (Castellani et al., 2017).

The pigment chlorophyll *a* (Chl *a*) occurs in all groups of micro-algae and its surface concentrations are thus indicative of the total standing stock of phytoplankton biomass; the combination of remotely-sensed Chl *a* concentrations, SST and SIC are commonly used to estimate total primary production in the Arctic Ocean (Lewis et al., 2020).

GPP is limited by the availability of inorganic nutrients and photosynthetically active radiation (PAR), which is the spectrum of short-wave radiation that can be utilized as source of energy by phytoplankton (Mõttus et al., 2012). It is therefore restricted to the euphotic zone of the water column, and commonly observed during the months of March to September, because light restrictions arise from the polar night during the winter months (Randelhoff et al., 2020). Once light becomes available in the water column at the beginning of spring, NPP rates start to increase exponentially and peak in late spring. This is referred to as the spring bloom, and is mainly driven by the growth of diatoms (Ardyna & Arrigo, 2020).

Light availability not only varies temporally, but also spatially. The seasonal cycle of sea ice exerts a strong influence on the amount of incoming radiation, as discussed in Section 2.1.2. Therefore, GPP decreases with increasing latitudes, where the sea ice tends to be more consolidated, the onset of melt is delayed, and light becomes available later during the year (Frey et al., 2024). Once the atmospheric radiation reaches the sea surface, the availability of PAR decreases with depth and light attenuation can be intensified by suspended particles such as terrigenous sediments, or through the self-shading effects of increasing biomass in the water column (Hoppe et al., 2024; Rudels & Carmack, 2022; Terhaar et al., 2021).

In the Arctic Ocean, nitrate is the limiting nutrient in the group of macro-nutrients, and model simulations show that winter and early-spring concentrations of nitrate pre-condition the magnitude of the peak productivity in spring (Castellani et al., 2017; Terhaar et al., 2021). The disproportionally large volumes of river run-off into the Arctic Ocean carry substantial amounts of micro-nutrients such as iron, and make the Arctic Ocean a source of micro-nutrients for the northern Atlantic (Krisch et al., 2022).

The commonly cited pathways for the replenishment of macro-nutrients (for simplicity hereafter only referred to as nutrients) in the euphotic zone are the advection from boundary oceans through the gateways, upward fluxes driven by deep winter mixing and upwelling, and in-situ re-mineralization by heterotrophic organisms (Castellani et al., 2017; Terhaar et al., 2021). Furthermore, Terhaar et al. (2021) estimate that 29 % to 51 % of current annual Arctic Ocean NPP could be sustained by terrigenous nitrogen fluxes from rivers and coastal erosion. Even though the trophic status of the system is mainly defined by nitrate concentrations, an observed decrease in silicate concentrations may trigger shifts in the phytoplankton species assemblage (Ardyna & Arrigo, 2020).

As described by Castellani et al. (2017), the presence of ice algae influences the timing and magnitude of the spring bloom. As light becomes available first 'inside' the ice, ice algae growth can determine the onset time of the spring bloom. At the same time, their presence increases shading for the pelagic algae and thus delays the onset of primary production in the water column due to light attenuation from pigments in the ice. Analyzing the results obtained from a new Sea Ice Model for Bottom Algae (SIMBA), the authors find that this shading effect can delay under-ice phytoplankton bloom by up to 40 days in regions north of 80 °N. Furthermore, the uptake and re-mineralization of nutrients by ice algae affects nutrient availability for under-ice communities.

Water column stratification and vertical mixing determine nutrient availability, but also the distribution and therefore light exposure of phytoplankton, which alters the dynamics and magnitude of the spring bloom (Hoppe et al., 2024). Sverdrup (1953) hypothesized that the spring bloom initiates once the mixed layer shoaling transports phytoplankton above a critical depth, where the light exposure is sufficient to make phytoplankton growth exceed losses. The critical depth level was estimated to lie between 30 m to 300 m depth, depending on the amount of incoming radiation, water transparency and respiration rates. One shortcoming of this theory is that the losses of phytoplankton alive biomass from grazing of zooplankton, viral lysis or sinking are assumed to be of equal rates across the water column. However, it has been shown that the distribution of grazers and concentrations of pathogens can vary significantly within the water column due to vertical mixing and related dilution of the upper water layers (Behrenfeld, 2010; Hoppe et al., 2024). Furthermore, a recent study found that the increase in light due to sea ice decline can delay upward migration of winter-active zooplankton (Flores et al., 2023). The authors hypothesize that the sea ice decline and related alterations in bloom dynamics from changes in light availability will widen the 'food gap' and decrease survival probabilities of migrating zooplankton. This may negatively affect higher trophic levels by altering the transfer of phytoplankton carbon into other ecosystem compartments (Ardyna & Arrigo, 2020; Flores et al., 2023).

2.2.2 Biological carbon pump

Carbon export is the transfer of organic matter produced by phytoplankton from the upper ocean to lower water levels, leading to the isolation of organic carbon from the atmosphere for extended time scales and thus its sequestration (Oziel et al., 2025). Recent calculations of the integrated Arctic Ocean carbon sink estimate oceanic uptake of CO_2 at 127 ± 36 Tg C year^{-1}, and the burial of organic carbon in shelf sediments at 112 ± 41 Tg C year^{-1} (Vonk et al., 2025).

The vertical transport and hence export of organic matter to deeper water layers and sediments is a combination of processes summarized as the marine biological carbon pump (BCP), which includes the export of organic and inorganic carbon (Oziel et al., 2025). Particulate *organic* carbon (POC), created through photosynthetic carbon fixation, is exported as organic detritus in two ways: (1) The gravitational sinking of phytoplankton aggregates; (2) The gravitational sinking of faceal pellets produced by zooplankton when grazing on phytoplankton. Export efficiency is affected by re-mineralization rates from metabolic respiration (Oziel et al., 2025). The export of particulate *inorganic* carbon via a sinking flux was demonstrated to be comparably small (< 5 %) (Oziel et al., 2025).

Based on observational data from the Barents Sea combined with results from numerical modeling, Rogge et al. (2023) show that the efficiency of the BCP can be augmented where primary production hotspots are located in areas of deep water formation. They propose that the effects of grazing and respiration are offset by accelerated downward transport of biomass via deep water plumes. The authors point out that other transport mechanisms, such as lateral transport by advection or eddies remain an uncertainty for modeling carbon export (Rogge et al., 2023).

The vertical migration of zooplankton can also contribute to the BCP as an 'active' component. It has been estimated to increase the carbon export of the BGC by 25 % to 132 % (Flores et al., 2023).

2.2.3 Trends and future predictions

Satellite-derived PP estimates published by the United States National Oceanic and Atmospheric Administration (NOAA) for the observational record of 2003 to 2024 show a 19.2 % increase in primary production during this period, corresponding to an annual increase in PP of 14.7 Tg C (Frey et al., 2024). These estimates are likely an under-representation, because PP was only assessed for areas of SIC below 10 % to avoid pixel contamination from sea ice on the satellite imagery. This approach excludes large areas of the Arctic Ocean, as can be seen in Fig. 2.1(b), and excludes contributions of the supposedly very productive ice-associated algae (Castellani et al., 2017).

Lewis et al. (2020) estimate a 57 % increase in NPP during the period of 1998 to 2018, based on Chl *a*, SST and SIC data. They find that this increase is mostly attributable to the decrease in sea ice extent and increase in open water duration during the first decade. During the second decade, the increase was mainly associated with an increasing concentration in Chl *a* (i.e. phytoplankton biomass), especially in the Chukchi and Barents seas (Lewis et al., 2020). The authors point out that this indicates increasing nutrient availability, which may be driven by changes in advection in these inflow regions. It may also be related to nutrient replenishment from deeper mixing driven by the disappearance of sea ice.

Despite the observed increase across the Arctic domain, some regions show a decrease in net primary production. The decline has been observed in the outflow shelves and is likely associated with these regions receiving increasingly nutrient-depleted outflow waters that have sustained increasing rates of primary production 'upstream' (Arrigo & Van Dijken, 2015).

Models suggest that the positive trend will continue throughout the 21st century, due to the reduction of sea ice extent and the related increase in light availability. This is expected to enable the Arctic Ocean to be capable of supporting higher trophic levels and may increase its carbon export rates (Terhaar et al., 2021). One signal of this trend are the so-called fall blooms, which commenced to develop in regions of seasonal ice cover. They appear to be triggered by the replenishment of nutrient concentrations through enhanced mixing from fall storms, and continued light availability due to a delay in sea ice re-freezing (Ardyna & Arrigo, 2020; Hoppe et al., 2024).

Oziel et al. (2025) model two future scenarios for PP and carbon export in the Arctic Ocean. One model simulates the commonly predicted increasing in primary production Their simulation shows that this trend is accompanied by a compositional shift towards smaller phytoplankton functional groups and a related increase in carbon to nitrate ratio, which eventually increases the carbon export flux. Productivity may further be enhanced by higher influx of terrigenous nutrients from increasing river flows or new sources such as the melt of glaciers (Oziel et al., 2025; Terhaar et al., 2021). However, the second scenario they simulated shows decreasing rates of biomass production and carbon export. This could be explained by previously observed changes in phytoplankton respiration rates, which increase faster with increasing sea water temperatures compared to their carbon fixation rates and zooplankton grazing rates. Additionally, mesopelagic re-mineralization by heterotrophic bacteria increases with increasing temperatures and larger organic matter stock. This would eventually lead to a decreased efficiency in carbon transfer to the interior ocean. It furthermore adds to the dissolved inroganic carbon pool at the sea surface, which would favor out-gassing.

To further complicate predictions, (Swoboda et al., 2024) show based on 13 years of vertical flux measurements that the release of terrigenous material from melting sea ice ballasts the sinking of organic aggregates, which increases their settling velocities and results in approximately 30 % higher carbon export in the vicinity of the melting ice-edge in the Fram Strait.

Chapter 3

Methods

3.1 Fundamental background of sea ice modeling

Seasonal variability of sea ice and snow cover in the polar regions affects the radiation and heat fluxes in the ocean-ice-atmosphere system, which significantly influences the global climate. Therefore, sea ice models are an integral component of Earth system models and ocean models in polar regions, and without realistic sea ice modeling there would not be realistic regional and global climate models (Hunke et al., 2010).

Sea ice models simulate the vertical and horizontal behavior of sea ice. The horizontal transport of ice and its properties is called sea ice advection and is mainly driven by wind (Blockley et al., 2022). Vertical changes are mostly associated with thermodynamic melt and growth (i.e. freezing) as a function of heat flux between ocean and atmosphere through the ice. The heat diffusion is a result of the net flux of energy at the surface and bottom of the ice, which depends on latent and sensible heat exchange. At the ice-atmosphere interface, it also depends on longwave upward and downward fluxes and shortwave radiation fluxes, which can be altered by ice albedo and absorptive properties of the sea ice (Blockley et al., 2022). Sea ice ridging is furthermore simulated as a mechanical process that alters the vertical (and horizontal) extent of sea ice (Blockley et al., 2022).

Sea ice models solve a fundamental sea ice thickness distribution function that accounts for all these processes, which can be represented by multiple continuity equations. The evolution of sea ice velocity is derived from the vertical integration of a momentum equation that describes the force balance in the ice pack (Rampal et al., 2016). The acceleration of ice mass per unit area depends on atmospheric and ocean stress, Coriolis and ocean-tilt terms, and a sea ice stress tensor representing the ice pack's strength. How the internal stress term changes as a function of deformation and material strength is defined by a set of equations that determine the sea ice model's rheology (Blockley et al., 2022).

3.2 Sea ice model comparison

In this project, two different model simulations are analyzed, which were obtained from running the biogeochemical ocean model HYCOM-ECOSMO with two different sea ice models. For one simulation, the biogeochemical model was coupled to the classical sea ice model CICE, for the second one it was coupled to the recently developed sea ice model neXtSIM. Below, the key differences between the two sea ice models are discussed. A summary of the key differences in provided below in Table 3.1.

3.2.1 Rheology

One of the key differences between CICE and neXtSIM is their rheologies. The CICE-simulation applies an elastic-viscous-plastic rheology (EVP) where the ice strength depends on ice thickness and ice concentration only. It simulates the ice behavior as a highly viscous, solid material that can dissipate internal stress until a defined threshold is exceeded, which leads to irreversible deformation (i.e. plastic behavior) (Feltham, 2008). The elastic component was introduced to simulate sea ice behavior under small strain rates that are typical for very thick and rigid ice. In these cases the model assumes an elastic behavior to avoid viscosity values tending towards infinity (Hunke & Dukowicz, 1997). One shortcoming of such EVP rheologies is their inability to simulate realistic deformation statistics when the model is run at resolutions coarser then 5 km, because the temporal and spatial scale of fractal features such as ridges and leads is highly variable (Blockley et al., 2022; Boutin et al., 2023; Ólason et al., 2025). Hence, such features tend to be underrepresented when CICE is run on a grid adapted to model the full Arctic domain, or when run over long time periods.

The neXtSIM-simulation discussed in this study was run with the brittle Bingham-Maxwell (BBM) rheology, which defines three different regimes of ice pack behavior: (1) Under high compressive stresses, the sea ice converges in a viscous-elastic manner; (2) under diverging normal stresses, the sea ice exhibits viscous-elastic diverging behavior; (3) under small compressive stresses the ice behaves purely elastic independent of the level of damage, which prevents unrealistic thickening of highly damaged ice (Ólason et al., 2025). One of the key advantages of this brittle rheology over the rheology applied in CICE is its parameterization of damage. Damage is represented by a scalar parameter that is altered when the stress exceeds a defined failure criterion (Mohr-Coulomb criterion). This damage parameter links large scale behavior causing stress and deformation to sub-grid features, and therefore allows fractures to occur in an elastic material at a more realistic scale (Ólason et al., 2022). Elasticity and viscosity, and as a result the ice strength, decrease with increasing damage. Viscosity reduces faster than the ice's elasticity. This was shown to realistically simulate irreversible deformations where the sea ice is highly damaged, for example along faults (Ólason et al., 2025). A simple healing term is defined based on the temperature gradient between the ice base and snow-ice interface. Healing does not appear during times of ice melt (Ólason et al., 2022). The strength of this rheology to model realistic sea ice fracturing is especially pronounced in areas of highly concentrated pack ice, and is less relevant in areas of lower SIC or where the ice pack is more mobile, because in such regions internal stress and deformation rates are usually low (Ólason et al., 2025).

3.2.2 Sea ice thickness distribution

CICE is run with five SIT categories with the following lower bounds: 0.00 m, 0.64 m, 1.39 m, 2.47 m, 4.57 m (Hunke et al., 2015). The ice cover in each grid cell is partitioned into the respective thickness classes and the model solves the continuity equations for each class separately (Hunke et al., 2015). Computation of thickness redistribution in neXtSIM is simpler, since the model operates with only two sea ice thickness categories: (1) young sea ice, with a slab thickness between 5 cm and 27.5 cm; (2) consolidated ice of variable thickness, which is formed by transferring young ice into the consolidated ice category over time or due to ridging. The continuity equations for thickness and concentration are solved separately for each ice category (Rampal et al., 2019). The larger number of SIT categories in CICE makes the simulation of ridge formation and the effects of such sea ice features on radiation fluxes more realistic compared to neXtSIM, as thickness can be distributed more gradually during ridge formation (Hunke et al., 2015; Ólason et al., 2025).

Ice advection in CICE is simulated using an Eulerian approach. Firstly, in each grid cell and for each thickness category separately, sea ice fractional area and tracer elements (ice and snow depth and energy, salinity, others) are calculated. Ice velocities are identified at the corners of each grid cell and used to calculate the fluxes of total ice area, volume, and energy across cell boundaries. Ice velocities are assumed to be the same for each thickness category. At the end of each time step, the state variables of all grid cells are updated and passed on to other model components to determine associated changes in diagnostic variables (Hunke et al., 2015).

neXtSIM is the first sea ice model with a fully Lagrangian framework for sea ice advection. This enables the model to better preserve smaller deformations and sea ice fractal features (Rampal et al., 2016). The model is set up with an unstructured mesh of triangles. The velocity of sea ice movement is calculated on the nodes, which move ’with’ the sea ice and thus change the area of each element. Sea ice volume in each element is conserved, by adding open water or increasing thickness during divergence and convergence respectively (Ólason et al., 2025). A remapping scheme is applied when distortion of the grid elements exceeds a set deformation threshold. Additionally, the representation of sub-grid features is improved by applying a time-splitting method for solving the momentum equation. This allows for updating rapidly evolving variables such as sea ice velocity, stress and damage in shorter time steps compared to advection, thermodynamics and healing (Ólason et al., 2022). It should be noted that neXtSIM applies an ice grounding scheme to simulate landfast ice, which can remain anchored to the coastline during the melt season (Boutin et al., 2023).

Thermodynamic thickness change (i.e. vertical growth and melt) in CICE is computed by treating each sea ice thickness category separately as a column of homogeneous ice. The effects of brine salinity on the enthalpy are considered (selected option 'mushy thermodynamics'). The salt content of the ice generally lowers its freezing temperature, and the model calculates the energy needed for melting as a function of the salinity. Ice formation in open water starts as frazil ice that is added to the thinnest category. Thermodynamic growth is applied at the bottom of existing sea ice and the ice area in each grid cell is conserved during transfer between thickness categories. Due to conductive fluxes, growth cannot appear at the surface. However, the formation of snow-ice at the surface can contribute to increasing ice thickness. Melting occurs at the top and bottom (Hunke et al., 2015).

Simulation of growth and melt processes in the discussed neXtSIM-simulation relies on two different thermodynamic models for the young and consolidated ice classes. Ice formation in open water is always added to the young ice. Its vertical growth and melt is simulated by solving the heat diffusion equation based on a one-layer approach of Semtner (1976) that assumes no heat capacity of sea ice. For consolidated ice, the model applies a two-layer approach according to Winton (2000) that treats the ice as layers of different internal temperatures and considers the effect of salinity as in the CICE-simulation (Ólason et al., 2025). Ice formed due to the flooding of snow (snow-ice) is also contributing to the growth of the ice pack thickness (Boutin et al., 2023).

CICE applies the **mechanical redistribution** scheme after horizontal transport, to ensure that the total ice area continues to fit into the grid cell after conversion. It transfers ice from a thinner into a thicker ice thickness category, while conserving ice volume and internal energy. As mentioned above, the rheology defines to which degree the ice deforms and thickens during conversion. A weighing factor is applied to favor the closing of open water and ridging of thinner ice (Hunke et al., 2015).

neXtSIM simulates ridge formation only in grid elements that are fully ice covered, as in this case the stress cannot be off-set by deformation of the grid cell triangle. In case the grid element is not fully ice covered, its open water fraction is reduced through the deformation of the grid cell. During convergence, overall ice volume and mean SIT are conserved. Comparable to CICE, ridging of the young ice is favored over ridging of consolidated ice, assuming that the latter is usually thicker and has more resistance to compressional forces. The volume of ridged young ice is transferred to the consolidated ice class, while ridged consolidated ice increases the ridge thickness (Ólason et al., 2025).

3.2.3 Material and radiation fluxes

Salinity and freshwater fluxes between ice and ocean affect the mixed layer depth and thus influence primary production in the Arctic. CICE accounts for changes in the ice's bulk salinity due to brine ejection over time. Desalination is enhanced by vertical flushing of melt ponds (Hunke et al., 2015). The melt of young ice in CICE is thus expected to have less freshening effects on the upper ocean than the melt of its multi-year ice. It should also be noted, that precipitation and all melted snow contribute to the freshwater influx to the ocean. Furthermore, all freshwater stored in melt ponds eventually ends up in the upper ocean when ice fully melts or melt ponds disappear due to ridging.

Sea ice in neXtSIM remains with a constant salinity of 5 after formation. Therefore, the melt of young ice in neXtSIM is assumed to have a stronger freshening effect compared to CICE, while freshwater fluxes from melting multi-year/consolidated ice should be comparable in both models. neXtSIM only considers the volume of melt ponds as a virtual reservoir with effects on albedo and heat budget, but without contributions to the freshwater balance (Ólason et al., 2025). Considering these differences, the melt of ice in CICE is expected to have a stronger freshening effect on the upper ocean than the melt of ice in the neXtSIM-simulation.

In CICE, shortwave radiation, and thus photosynthetically active radiation are allowed to penetrate through the ice into the ocean as a function of the sea ice thickness. Absorption from algal pigments in the ice is parameterized. In contrast, neXtSIM does not allow for light flux through the ice.

Both sea ice-coupled simulations were run without accounting for sea ice algae or nutrients in the sea ice. Nutrient cycling and biological activity are handled solely by HYCOM-ECOSMO.

3.3 HYCOM-ECOSMO coupling

The Hybrid Coordinate Ocean Model (HYCOM) is an ocean physics model that has previously been coupled to the sea ice model CICE to simulate the Arctic Ocean.

ECOSMO II(CHL) is a 3D bio-physical ECoSystemMOdel that simulates hydrodynamics and an intermediate-complexity biology of the lower trophic levels, including nutrient cycles, phytoplankton and zooplankton evolution and detritus pathways. Sediment and water column exchange processes are also considered (Daewel & Schrum, 2013; Yumruktepe et al., 2022). The model simulates the trophic interactions between three phytoplankton groups (diatoms, flagellates, coccolithophores) and two zooplankton groups (micro- and meso-zooplankton). It models nutrient pathways for nitrate, ammonia, phosphate and silicate, which are treated according to the molar Redfield ratio, and also accounts for DOM and particulate (detrital) organic matter (Yumruktepe et al., 2022). Nutrients are tracked in the water column and inside a single sediment layer. In 2017, chlorophyll *a* was introduced as a prognostic state variable for each phytoplankton group, following the approach of Geider et al. (1997). This has significantly improved the simulation of seasonal and vertical variability of phytoplankton biomass to chlorophyll *a* ratio. It presents a good indicator for biological interactions and productivity, and accounts for processes such as photoacclimation (Yumruktepe et al., 2022).

HYCOM-ECOSMO's original domain covers the Arctic and includes the most northern regions of the Atlantic, which are relevant for simulating the Atlantic inflow through the Fram Strait. The model is run with a grid of 400 x 380 grid points with average grid spacing of 17 km. The model bathymetry is interpolated from the Bathymetric Chart of Oceans database (Jakobsson et al., 2024). The ocean model assumes hybrid vertical coordinates, using isopycnals in the stratified open ocean and z-coordinates in the upper ocean mixed layer due to its homogeneous potential density. This method has shown to be suitable for representing the density-driven inflow of Atlantic water and deep water formation in the Arctic (Sakov et al., 2012). For biogeochemical simulations, the upper five depth levels are always set as z-levels, in order to keep a minimum vertical resolution in areas of very shallow mixed layer depth. This is important to ensure realistic representation of the decrease in biomass production due to the light gradient in the upper ocean (Yumruktepe et al., 2022). Advection and mixing, i.e. the transport of biological state variables, is handled by the ocean model HYCOM via its native tracer-transport routines, coupled to ECOSMO via the open source Fortran-based Framework for Aquatic Biogeochemical Models (Bruggeman & Bolding, 2014). As a result, all physical and biological components are assessed using the same time-stepping scheme of 20 min. The model code is publicly available and can be accessed on NERSC's Github (NERSC, 2025).

For the simulations analyzed in this study, the biogeochemical model was initialized in 1992, from a spin-up starting in 1987. The initial conditions for nutrient concentrations were derived from the World Ocean Atlas (WOA) 2013 climatologies, and biomass values were set at low uniform concentrations (compare Yumruktepe et al. (2022)). The model physics were initialized in 1986, based on a spin-up run starting in 1977, based on WOA 2018 climatologies for temperature and salinity. WOA datasets are available at https://www.ncei.noaa.gov/products/world-ocean-atlas.

For both simulations, the sea ice coupled HYCOM-ECOSMO was forced with atmospheric data from the European Centre for Medium-Range Weather Forecasts' (ECMWF) ERA-Interim reanalysis (Dee et al., 2011). The CICE-simulation was forced with 6-hourly atmospheric forcing vs. 1-hourly in the neXtSIM-simulation. For the physical component of the ocean model, the forcing variables include 10 m winds, 2 m air temperature, dew-point temperature at 2 m, cloud coverage and total precipitation. The biogeochemical model component is forced by the surface net solar radiation. River forcing is simulated with monthly climatologies derived from three hydrological models for the Arctic (see Table 3.1 for details), and flow volumes are used to scale nutrient influx (compare Yumruktepe et al. (2022). Thus, river runoff does not account for inter-annual variability in nutrients or other fluxes.

The HYCOM-ECOSMO coupled model is nested at its boundaries with a reanalysis of the Nucleus for European Modelling of the Ocean (NEMO), including the blue ocean (thermodynamics) and the green ocean (TOP-PISCES and biogeochemical) (EU Copernicus Marine Service, 2020). Nesting data is of daily resolution and applied with a relaxation time-scale of 1 day, which allows for simulating interannual variabilities of the boundary conditions. State variables were relaxed to WOA 2013 climatologies (and WOA 2018 for salinity) at the boundaries during the

Table 3.1: Comparison of simulation set-up and overview of key differences between the sea ice models used in this study.

	CICE	neXtSIM
Simulation set-up		
Ocean model	Hybrid Coordinate Ocean Model (HYCOM)	
Biogeochemical model	ECOSMO II(CHL)	
Nesting	Copernicus marine reanalysis product for Arctic Ocean physics and hindcast for biogeochemistry, daily resolution	
Atmospheric forcing	6-hourly ERA-Interim reanalysis	1-hourly ERA-Interim reanalysis
River forcing	Arctic-HYPE+TRIP+Greenland runoff, monthly climatologies	
Model relaxation	WOA 2013 and WOA 2018, monthly climatologies	
Analysis period	Simulation period: 2007-2016; target years: 2012-2013	
Key differences of sea ice models		
Rheology	Elastic-viscous-plastic (EVP)	Brittle Bingham-Maxwell (BBM)
Advection scheme	Eularian	Lagrangian, time-splitting
Thickness classes	5	2
Thermodynamics	'Mushy'	Single-layer, two-layer
Salinity/freshwater	Brine ejection, melt ponds	5 (constant)
Radiation fluxes	Light penetration	No light penetration

model spin-up. Relaxation for salinity and temperature was stopped after 1993, while nutrients, alkalinity and DOC continued to be relaxed at a time-scale of 20 days. All WOA datasets are accessible on the website of NOAA (NOAA, 2025).

The CICE-coupled model run commenced in 1993, whereas the neXtSIM-coupled simulation was initialized in January 2006 from a restart file of the CICE-run. It was decided to select the analysis period of 2007 to 2016, to allow for a one-year spin-up period for the neXtSIM-simulation.

An overview of the simulation set-up and model coupling, together with a summary of the key difference between the two sea ice models is provided in Table 3.1.

3.4 Datasets and processing

Both sea ice models output their simulation results as netCDF-files, adopting the grid dimensions of the HYCOM-ECOSMO native grid (400 x 380 grid points). Other relevant dimensions are the sea ice thickness categories (five in CICE, two in neXtSIM) and the time dimension that provides a time stamp for the output variables. To adapt the files according to analysis needs (daily, monthly and climatology files), they were processed using the following command line toolboxes: the Climate Data Operators (CDO) collection, module version CDO/1.9.10 (for further documentation see Schulzweida (2023)); and the netCDF Operator (NCO) toolkit, module version NCO/5.1.3 (Zender, 2008).

CICE generates one netCDF-file with one timestep for each day separately. To create monthly average files, the CDO command ’mergetime’ was applied to create temporary files that sum all daily files for a month. Afterwards, the CDO command ’monmean’ was applied, which creates monthly average files for each month of each year. The data processing of the neXtSIM-files was slightly different, since the model creates 6-hourly outputs combined into one monthly netCDF-file with 112, 120, or 124 timesteps, depending on the length of each month. The CDO command ’timmean’ was performed on the neXtSIM sea ice files to create monthly averages of variables across all timesteps contained in each original monthly file. For plotting daily time series of neXtSIM sea ice, the functionalities of the Python package ’xarray’ were used to plot a daily average of the 6-hourly variable values.

The biogeochemical data is contained in the output files of the coupled HYCOM-ECOSMO set-up, the so-called .a/.b file pairs. The .a-files contain all output data in binary format, whereas the .b-files describe the meta data. In order to proceed with the analysis of the biogeochemical conditions in the model simulations, the model’s output files needed to be converted to netCDF-format. For that purpose, the ’hyc2proj’-routine was run on all output file pairs. The routine and examples of all the necessary input files are available on the Nansen Environmental and Remote Sensing Center’s Github (see NERSC (2025)). ’hyc2proj’ reads and horizontally interpolates the data on a selected projection. It afterwards extracts selected variables by interpolating the respective model fields vertically onto pre-selected depth levels. The output file is a netCDF-file with one value per variable per grid cell at each selected depth level. Biogeochemical variables were extracted at 26 depth levels, spanning the upper 500 m of the ocean. Horizontal interpolation was omitted by selecting the ’native’ grid option and all analysis was performed on the model grid. The resulting daily netCDF-files were further processed with the CDO commands ’mergetime’ and ’monmean’ to create monthly average files.

Finally, to create climatology-files for the simulation period of 2007 to 2016, the ’ncra’ command of the NCO toolkit was applied to the monthly averaged files of sea ice and biogeochemistry-outputs.

Time series of the daily and monthly netCDF-files were plotted in Python, mainly using the packages ’xarray’, ’numpy’ and ’netCDF4’. These allow the handling of multi-dimensional arrays of netCDF-files. The ’cartopy’ package was used to map the variables of interest from the monthly average files using a Polar Stereographic Projection that is most suitable for analysis of the Arctic domain. It was decided to plot the months of March, April, May and June, since they are most representative of the onset of the spring melt and algal spring bloom across the Arctic domain. This supports the analysis of differences arising in Arctic primary production modeling due to differences in the coupled sea ice models. March to May are hereafter referred to as the Arctic spring months, while June will be referred to as the first month of the Arctic summer.

3.5 Selected variables

The following variables were extracted for analysis: temperature, salinity, nutrient concentrations (silicate, nitrate and phosphate), mixed layer depth (MLD) as well as gross primary production values, carbon export, sea ice concentration (SIC) and sea ice thickness (SIT).

All biogeochemical variables are available as the grid cell mean. Salinity is given as practical salinity and is thus unit-less. Temperature is expressed in °C. Nutrient concentrations are given in mole concentration in sea water with the unit mmol m^{-3}. MLD is defined by sigma theta (temperature and oceanic vertical diffusivity), which means the model identifies the thickness of the mixed layer from the surface down to the depth where the density difference diverts by 0.01 kg/m3 from a reference level.

Primary production can only be extracted as gross primary production (GPP), because the model does not have an explicit term for respiration (Yumruktepe et al., 2022). It computes GPP rates separately for each phytoplankton type, as a function of a default maximum growth rate, the limiting factors for light and nutrients, and phytoplankton biomass. The variable is given as carbon per unit volume in sea water in mg m^{-3} d^{-1}. For further analysis, GPP was vertically integrated over 500 m. The unit of the integrated GPP is mg C m^{-2} d^{-1}. As the limiting factors are treated by the model as factors for the calculation of GPP rates, light limitation and nitrate limitation are unit-less and range between 0 and 1, with 0 representing full limitation, and 1 presenting no limitation. During extraction with 'hyc2proj', the limiting factors were also interpolated onto the selected depth levels. Therefore, the limiting factors needed to be integrated across 100 m depth for further analysis.

Carbon export is calculated as the product of detrital biomass and sinking speed and is thus a combination of downward transport inside the mixed layer, and gravitational sinking below the mixed layer. The variable was extracted at depths of 300 m and 500 m for both simulations.

SIC is given as cell average as a range between 0 and 1. It was decided to exclude SIT as a predictor for GPP when comparing the two simulations, because open water in the grid cell is included during the calculation of the SIT cell average. This makes it difficult to discern the effect of light penetration through ice in CICE vs. no light penetration in neXtSIM from the actual influence of open water in the grid cell.

3.6 Analysis methods

Climatologies from the simulation period between 2007 and 2016 of key physical and biogeochemical fields and sea ice parameters were plotted as spatial averages across the full Arctic domain. The objective of this primary analysis was to assess whether both coupled models simulate the expected annual cycles of the variables.

Hovmöller diagrams were plotted from monthly data to display the depth distribution of GPP and limiting factors, to understand at which depth PP in the water column is limited. These plots also indicated across which depth the limiting factors needed to be integrated.

Daily time series for the spatially averaged sea ice parameters, biogeochemical key fields and limiting factors (light, nutrients) were plotted for selected regions and target years to identify the variables with the potentially strongest influence on integrated GPP in both coupled model runs.

The monthly average files for March to June of both target years were mapped to show the spatial distribution of the key variables within the selected regions, to understand which factors cause spatial differences in PP between the model simulations.

Based on the analysis steps above, the supposed key predictors of GPP were assessed using linear least-squares regression analysis with the Python statistical function 'linregress' from the SciPy package. The function returns the Pearson correlation coefficient and the p-value based on the null hypothesis that the slope is zero, using the Wald Test with t-distribution. The regression analysis was conducted with daily data, correlating the variable values for all grid cell points for each month separately (March to June).

Chapter 4

Results

In the following section, the results for the analysis of the two available HYCOM-ECOSMO simulations coupled to the different sea ice models CICE and neXtSIM will be presented. First, climatologies of the key biogeochemical and sea ice parameters are included, which present a spatial average of these variables across the Arctic domain. Afterwards, the results from the analysis of the selected regions are presented. These include time series for the target years 2012 and 2013, plotted from daily data as spatial averages across each region. The time series of both simulations are plotted together to enable comparison, throughout with the CICE-coupled simulation in red, and the neXtSIM-coupled simulation in blue. To determine spatial differences between the simulations, maps were plotted from the monthly mean files. For sea ice and biogeochemical parameters, the maps of March to June were analyzed for both target years, while MLD was plotted for the months of January to June to include the months of deep winter mixing in the beginning of both years.

4.1 Selection of study regions and target years

The Arctic domain was divided into 12 sub-regions, and daily time series of integrated GPP and sea ice parameters plotted for the target years were used to identify notable differences in both simulations. These were taken into consideration to select the following regions for further analysis: (1) The Arctic Atlantic region (ArcAtl) is a central Arctic region and shows thick sea ice and high SIC values throughout the year. (2) The Chukchi Sea (CHS) is one of the inflow regions of the Arctic with high SIT and SIC values in winter, but low SIC during summer. The CICE-simulation simulates higher productivity than neXtSIM, which is also missing the spring bloom peak in 2013. (3) The Barents Sea in a region of the marginal ice zone, and primary inflow region of Atlantic water. The spring bloom onset appears earlier and the GPP peak is higher in CICE. Fig. 4.1 shows the extent of the regional masks that were applied in this study for the three selected regions.

Regional analysis was conducted for the low sea ice year 2012 and the following year 2013,

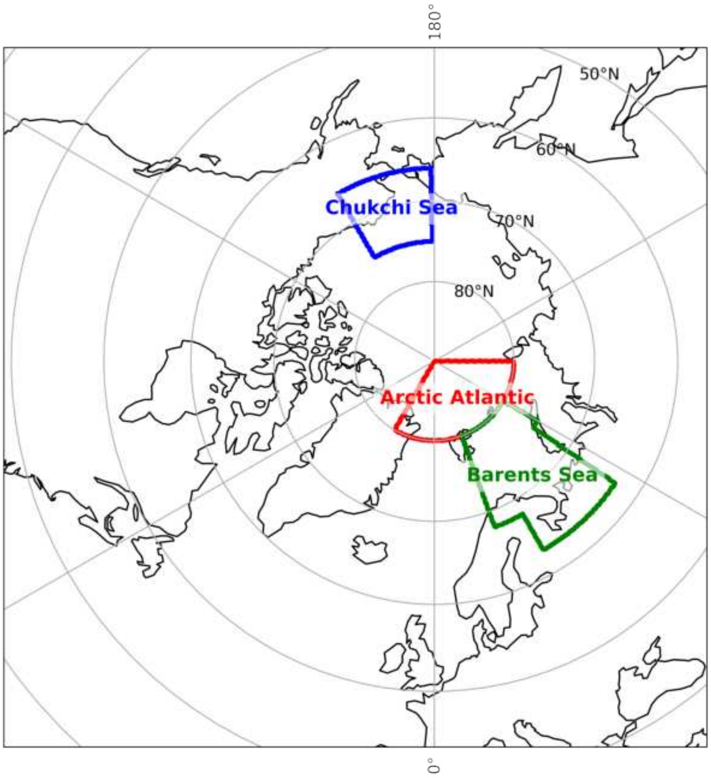

Figure 4.1: Map of the Arctic domain, showing the extents of the selected study regions.

which are expected to show larger responses of GPP to stronger sea ice dynamics. This choice also aims at understanding how effects of sea ice minima may accumulate over time.

4.2 Climatologies of the Arctic domain

Climatology data from the simulation period of 2007 to 2016 was used to plot the seasonal cycles for the key physical, biogeochemical and sea ice parameters, spatially averaged across the full Arctic domain.

The SST climatologies presented in Fig. 4.2 shows strong agreement between both model simulations, with maximum temperatures of approximately 5 °C in August, and minimum temperatures below 1 °C in January to April. The surface salinity climatologies presented in Fig. 4.3 show that neXtSIM is more saline than CICE. Maximum salinity in both simulations is reached in April, which also shows the maximum difference in salinity of 0.75. Minimum surface salinities appear in August.

The MLD climatologies of both simulations show the expected mixed layer deepening in fall and shoaling in spring (Fig. not shown). The neXtSIM-simulation models deeper winter mixing. The maximum difference in MLD shows in March, where the neXtSIM-simulation is more than 10 m deeper compared to the CICE-simulation.

The climatologies of the surface concentrations for all three nutrients show a decrease in concentrations starting in spring (Fig. not shown). Minimum values are reached towards the

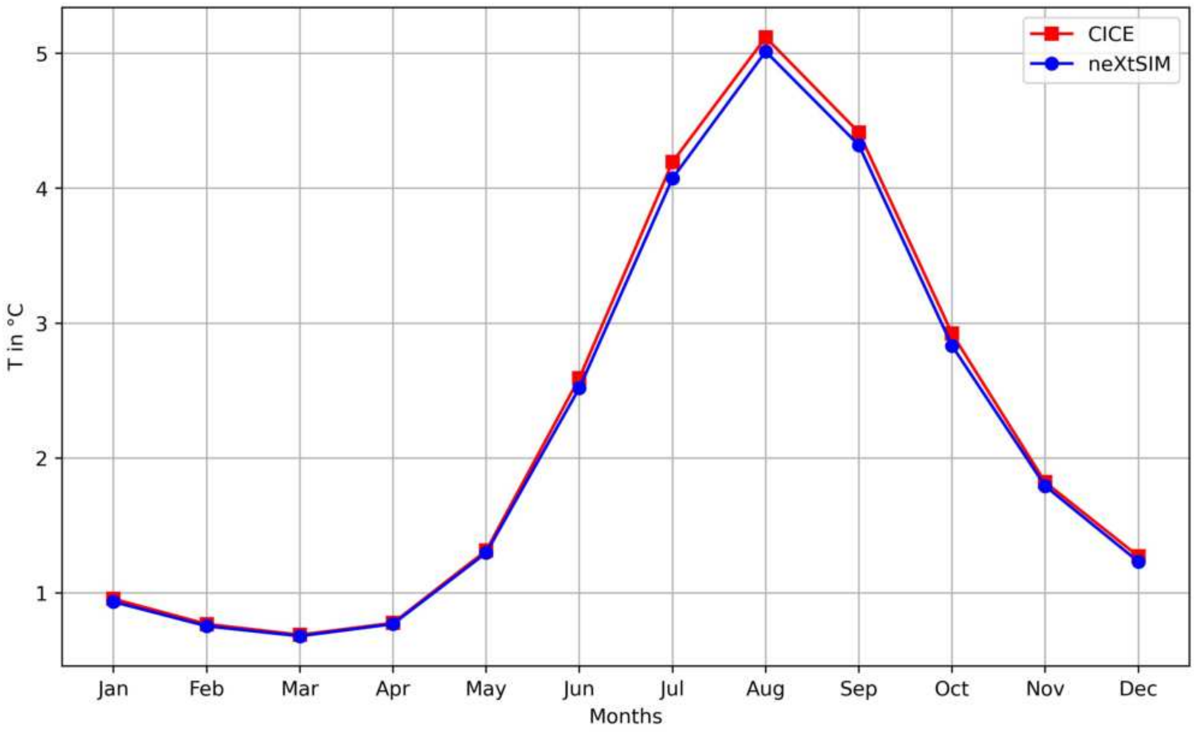

Figure 4.2: Climatologies of SST for the simulation period from 2007 to 2016, plotted for both simulations.

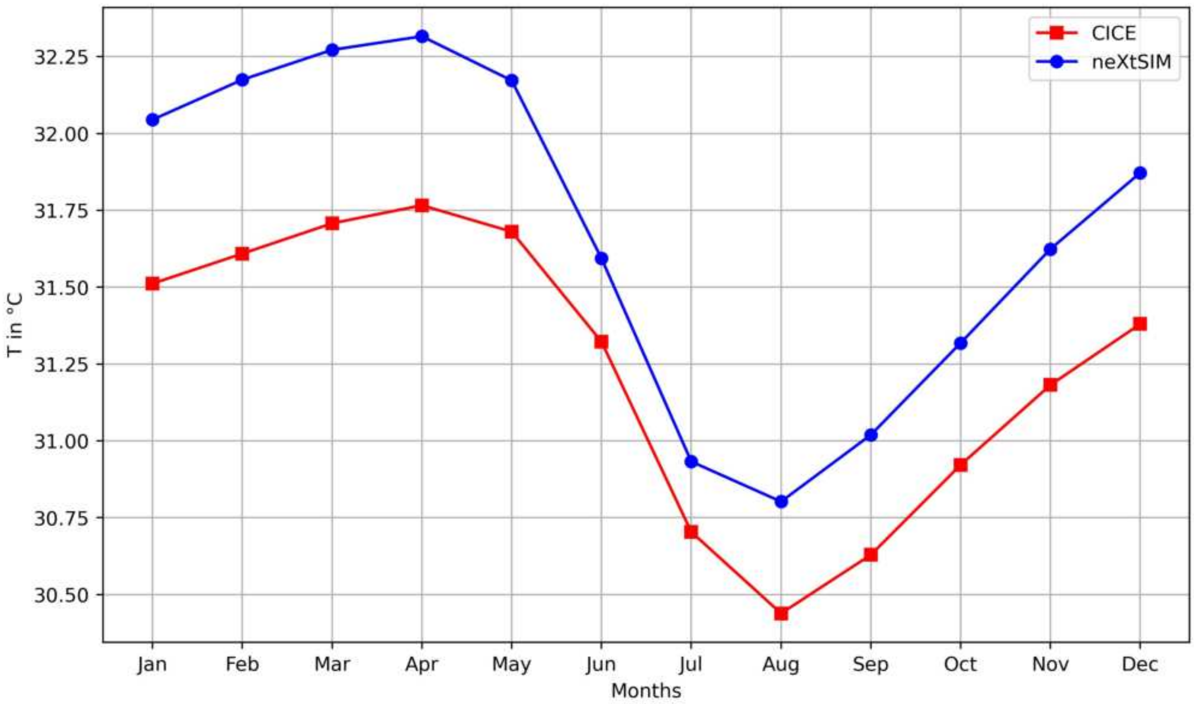

Figure 4.3: Climatologies of surface salinity for the simulation period from 2007 to 2016, plotted for both simulations.

end of the summer. The CICE-simulation shows an earlier drop of all nutrient concentrations in spring compared to the neXtSIM-simulation. In both simulations, nitrate appears to be the limiting nutrient, as surface concentrations drop below 1.0 mmol m^{-3}. Climatologies of integrated GPP show higher production rates in CICE throughout the year (Fig. not shown). Growth starts earlier and is stronger in the CICE-simulation. The peak production is reached in May, with approximately 360 mg C m^{-2} d^{-1} in the CICE-simulation, and approximately 290 m C m^{-2} d^{-1} in the neXtSIM-simulation.

The climatologies for the sea ice parameters (Figures not shown) display a larger SIT in the CICE-simulation compared to the neXtSIM-simulation. Both reach their SIT maximum in April, and drop to the minimum in August. The largest difference between simulations shows between September and November. SIC in winter are higher in the CICE-simulation, which also shows a stronger decrease and earlier minimum of SIC in August. The minimum in neXtSIM is reached in September. SIC decline starts during March in both simulations.

The across-domain climatologies of all key parameters show that both coupled models simulate the expected seasonal cycles. Rates of integrated GPP in both simulations are of the same order of magnitude as reported by NOAA (compare Frey et al. (2024)). CICE simulates higher rates of integrated GPP across the full domain during the period of 2007 to 2016, while also having thicker winter SIC. Mixed layer and sea surface salinity are larger in the neXtSIM-simulation.

4.3 Barents Sea

The Barents Sea is an inflow region of the Arctic Ocean on the Atlantic boundary. It was selected for analysis to identify the effects of the ice edge in both model simulations on primary production in HYCOM-ECOSMO. The analysis of the spatial averages in the form of daily time series was not conducted, as large areas of this region are ice free throughout the year. Hence, the large differences in key variables arising from conditions in open water vs. underneath the sea ice are expected to disguise the effects of the sea ice characteristics on PP. Therefore analysis was mostly based on the maps of the monthly mean values. Nevertheless, the time series of SIT and SIC were plotted to show differences in the sea ice parameters across the grid cells that contain sea ice.

The maps for integrated GPP for March to June (see Fig. 4.4 for neXtSIM 2012) show similar patterns in both years and simulations. PP starts to appear in March along the Norwegian coast and on the western coast of the Novaya Zemlya archipelago along the eastern boundary of the region. Another band of GPP occurs north of 75 °N. The central areas of the region show low production values in March, but show increased production rates in April, May and June, during which primary production increases across the region.

The maps that show the differences of integrated GPP rates between simulations, presented in Fig. 4.5 for 2012 as an example confirm that productivity in March is higher in CICE almost

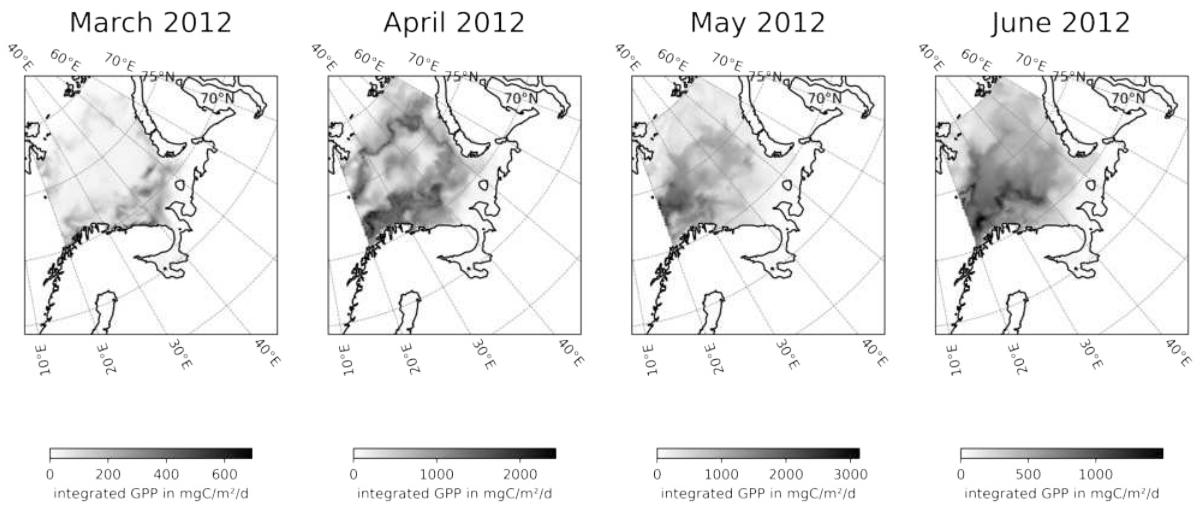

Figure 4.4: Maps of integrated GPP rates (in mg C m^{-2} d^{-1}) in the Barents Sea from the neXtSIM-simulation for March to June 2012, plotted from monthly mean files. The White Sea is located approximately between 30 °E and 40 °E along the 65 °N latitude.

everywhere in the region. The CICE-simulation continued to have higher rates in April in the central areas, whereas the northern and southern extents of the Barents Sea show higher productivity rates in neXtSIM during April. Both simulations show very low primary production rates in the White Sea and along the Siberian coastline in the South of the Barents Sea.

Daily time series of the sea ice parameters show that SIC remains lower in neXtSIM throughout both target years. The SIT time series presented in Fig. 4.6 shows that winter sea ice is thinner in 2012 compared to 2013 in both simulations. Maximum thickness is comparable in 2012, but SIT is larger in neXtSIM in 2013. Melting starts earlier in neXtSIM in 2012, but timing is similar in 2013.

SIC maps (Fig. 4.7 of neXtSIM as example) show that in 2013 the sea ice extent, defined according to NOAA as areas with SIC larger than 15 % (Meier et al. (2024)) extents further into the central areas from the northern, southern and southeastern boundaries of the region. The sea ice extent in CICE appears larger and has higher SIC during both years compared to neXtSIM, which can be seen in the difference maps presented for the year 2012 in Fig. 4.8.

The maps plotted for the light limitation factor (not shown) show that areas where the light limitation factor is below 0.2 largely co-locate with the areas of the sea ice extent in both simulations and both years. The difference maps for 2012, presented as an example in Fig. 4.9 show that the neXtSIM-simulation is less light limited compared to the CICE-simulation in the highest latitudes of the region during all months. Difference maps for 2013 show similar differences of lower magnitude.

Both simulations show large values for the nitrate limitation factor across the full area of the region during the spring months and June in both years. This means that the Barents Sea is not nitrate limited in neither simulation during those months. A slight decrease in limitation is detected towards the summer. Both simulations show low nitrate limitation factors in the White

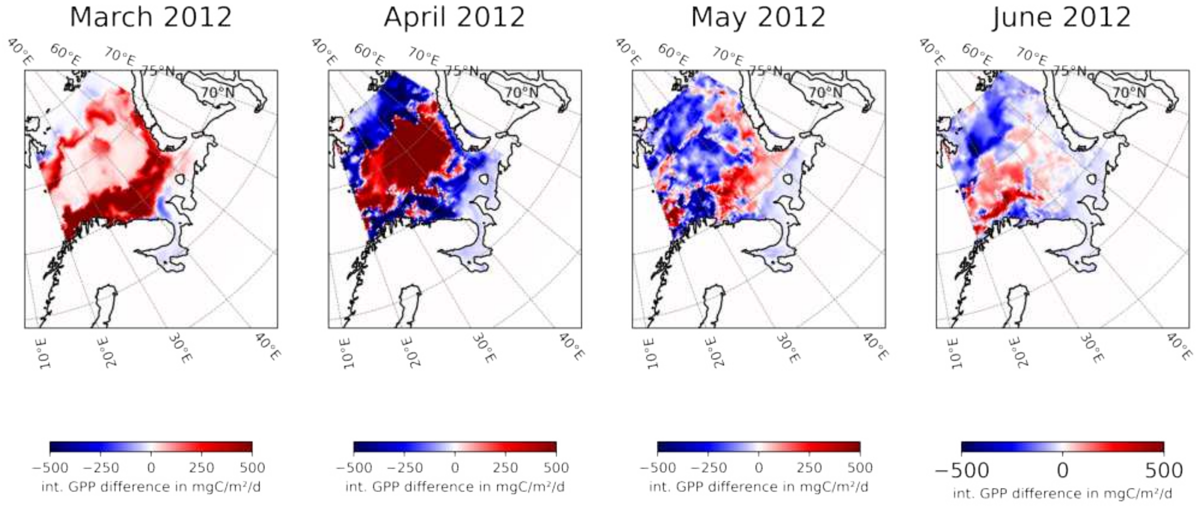

Figure 4.5: Difference maps (CICE minus neXtSIM) of integrated GPP rates (in mg C m^{-2} d^{-1}) in the Barents Sea for March to June 2012, plotted from monthly mean files.

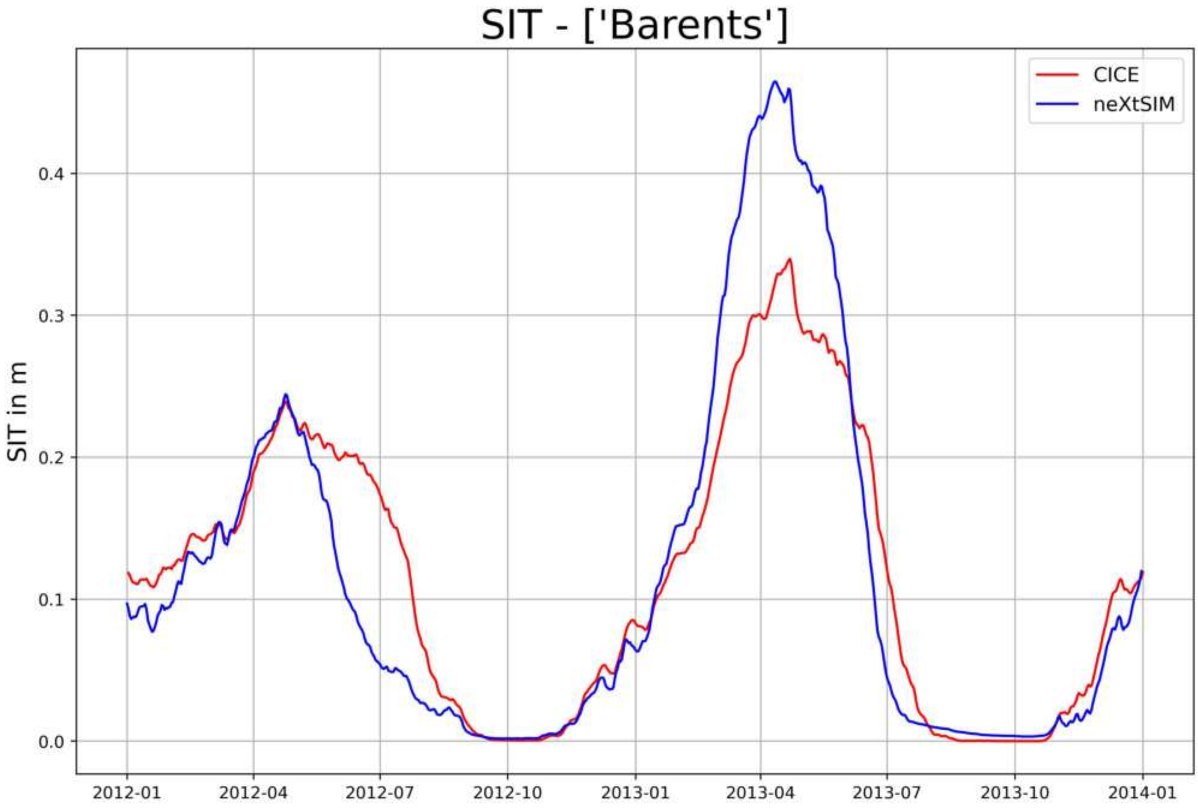

Figure 4.6: Time series of SIT for 2012 to 2013 for both simulations, plotted as regional average from daily files.

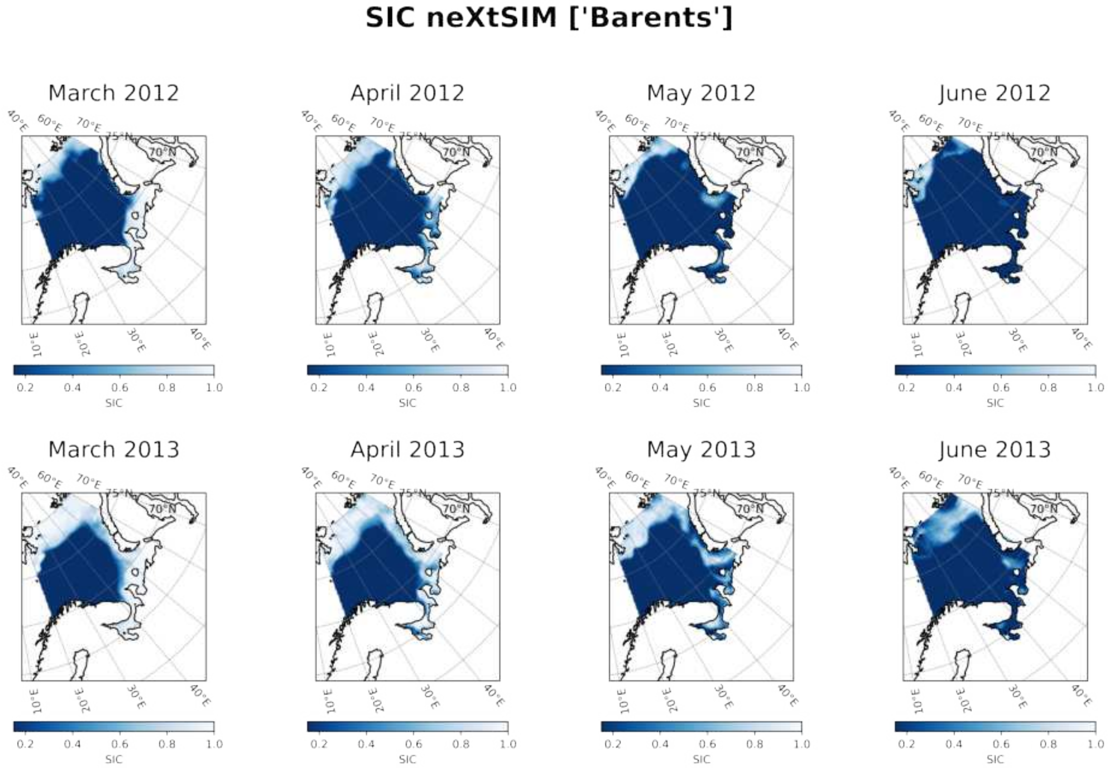

Figure 4.7: Maps of SIC in the Barents Sea from the neXtSIM-simulation for March to June of both years, plotted from monthly mean files. The White Sea is located approximately between 30 °E and 40 °E along the 65 °N latitude.

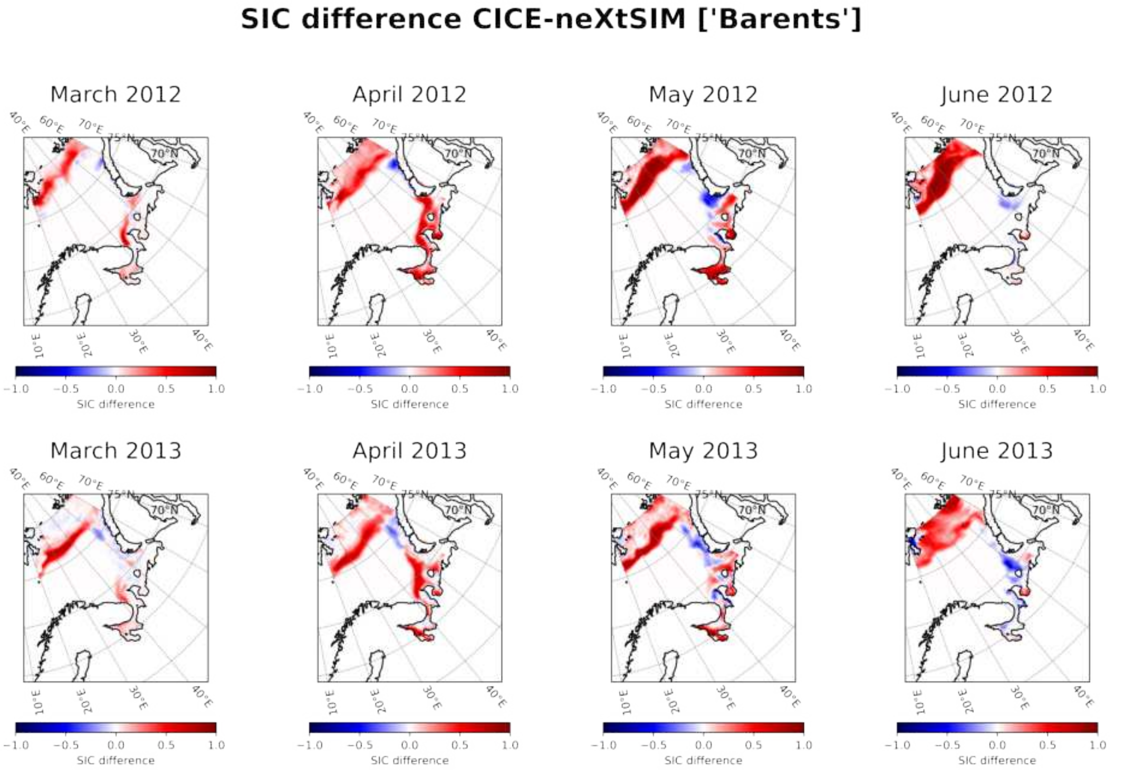

Figure 4.8: Difference maps (CICE minus neXtSIM) of SIC in the Barents Sea for March to June 2012, plotted from monthly mean files. Red areas indicate higher SIC in CICE, blue areas indicate higher SIC in neXtSIM. The White Sea is located approximately between 30 °E and 40 °E along the 65 °N latitude.

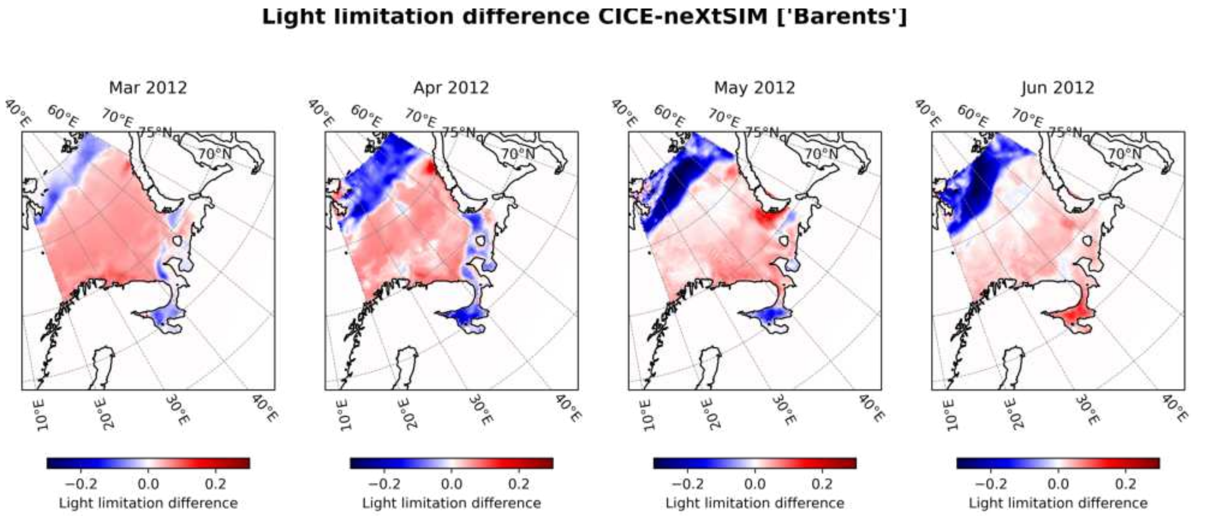

Figure 4.9: Difference maps (CICE minus neXtSIM) of light limitation (integrated over 100 m) in the Barents Sea for March to June 2012, plotted from monthly mean files. Red areas indicate higher light availability in CICE, blue areas indicate higher light availability in neXtSIM. The White Sea is located approximately between 30 °E and 40 °E along the 65 °N latitude.

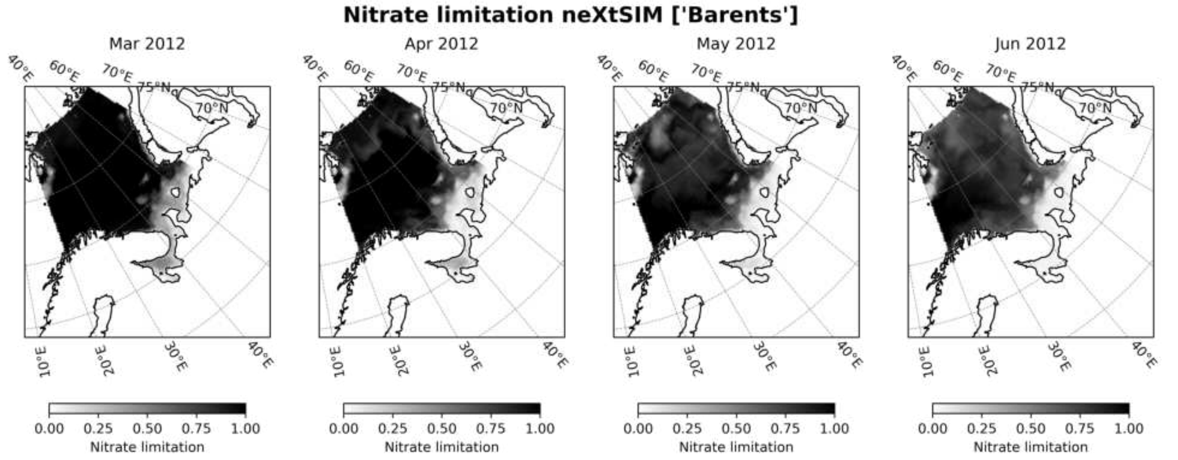

Figure 4.10: Maps of nitrate limitation (integrated over 100 m) in the Barents Sea from the neXtSIM-simulation for March to June in 2012, plotted from monthly mean files. Darker shading indicates higher nitrate availability. The White Sea is located approximately between 30 °E and 40 °E along the 65 °N latitude.

Sea and along the southeastern coast of Siberia (see Fig. 4.10 as example for neXtSIM 2012). The difference maps (not shown) reveal that the neXtSIM-simulation is less nitrate limited in the regions of the sea ice extent in March and April of both years.

The maps of the MLD (see Fig. 4.11 as example for neXtSIM 2012), plotted for January to June show for both simulations and both years that the mixed layer is deepest in the central areas of the region during winter and spring. Both simulations show the expected shoaling of the MLD in May and a more uniform shallow mixing across the region in June of both years. The mixed layer is very shallow in the White Sea and along the Siberian during all months in both simulations. Both model simulations show less deep mixing during the winter in the areas of the sea ice extent. Difference maps (see Fig. 4.12 for 2012) show that neXtSIM simulates deeper MLD underneath the sea ice extent. This difference along the ice edge in the north is more pronounced in 2012 compared to 2013. In June 2013, the CICE-simulation shows a small area of deeper mixed layer east of Svalbard with a depth of more than 75 m.

The carbon export time series could only be obtained at 300 m depth, due to the shallow bathymetry of the Barents Sea. Both simulations show peak export rates of more than 10 mol m^{-2} d^{-1} during July, with the neXtSIM-simulation lagging slightly behind the CICE-simulation during both years.

In summary, the comparison between the simulations in the Barents Sea shows that the neXtSIM-coupled model simulates higher rates of primary production underneath the sea ice extent. SIC are lower in neXtSIM, and light availability underneath the sea ice is higher. Sea ice melt is stronger in neXtSIM during 2012 until August, and SIT decrease is larger in neXtSIM in 2013 compared to CICE. The neXtSIM-coupled model further shows deeper mixing and lower nitrate limitation underneath the sea ice.

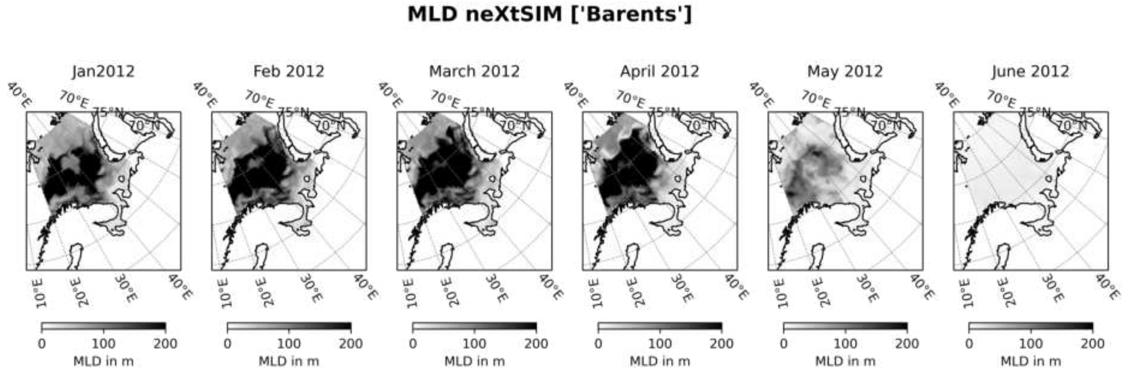

Figure 4.11: Maps of MLD (given in m depth) in the Barents Sea from the neXtSIM-simulation for January to June 2012, plotted from monthly mean files. The White Sea is located approximately between 30 °E and 40 °E along the 65 °N latitude.

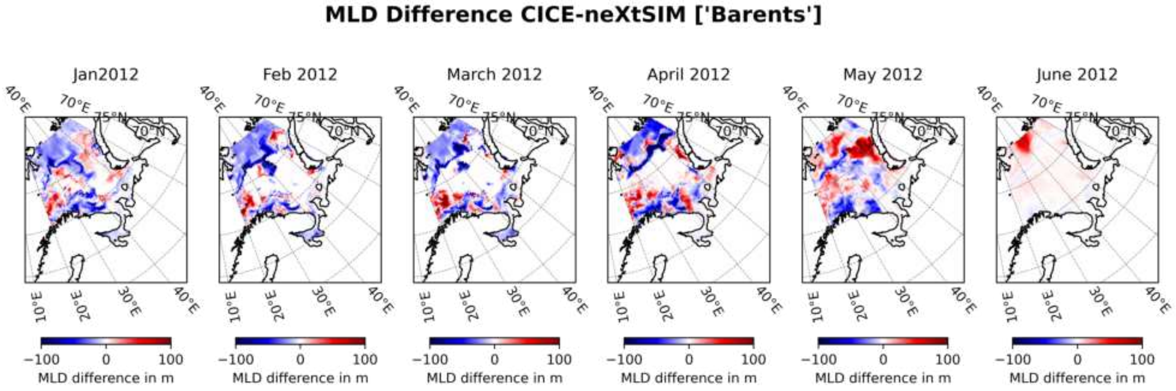

Figure 4.12: Difference maps (CICE minus neXtSIM) of MLD in the Barents Sea for January to June 2012, plotted from monthly mean files. Red areas indicate a deeper mixed layer in CICE, blue areas indicate a deeper mixed layer in neXtSIM. The White Sea is located approximately between 30 °E and 40 °E along the 65 °N latitude.

4.4 Arctic Atlantic

The Arctic Atlantic region is located north of the Barents Sea and was selected as region that belongs to the central Arctic Ocean. It remains largely ice covered during the summer months. Its sea ice cover is constituted by considerable extents of thicker multi-year ice (Meier et al., 2024). Large volumes of sea ice are exported along the Greenland coast from the Arctic in this region.

4.4.1 Biogeochemical variables

The daily time series of integrated GPP (see Fig. 4.13) for 2012 and 2013 shows an earlier onset of the spring bloom in the neXtSIM-simulation, with a larger difference in onset time for the year 2012 compared to 2013. Peak integrated GPP rates of over 8 mg C m^{-2} d^{-1} are higher and reached earlier in neXtSIM compared to the CICE-simulation, which shows peaks at apprximately 7 mg C m^{-2} d^{-1}. Furthermore, the neXtSIM-coupled model simulates two peaks in April and June. The monthly depth distribution of GPP plotted as Hovmöller diagram (not shown) indicates that primary production occurs down to a depths of approximately 80 m to 90 m in 2012 and 2013 in both simulations, reaching slightly deeper in 2013 in both models.

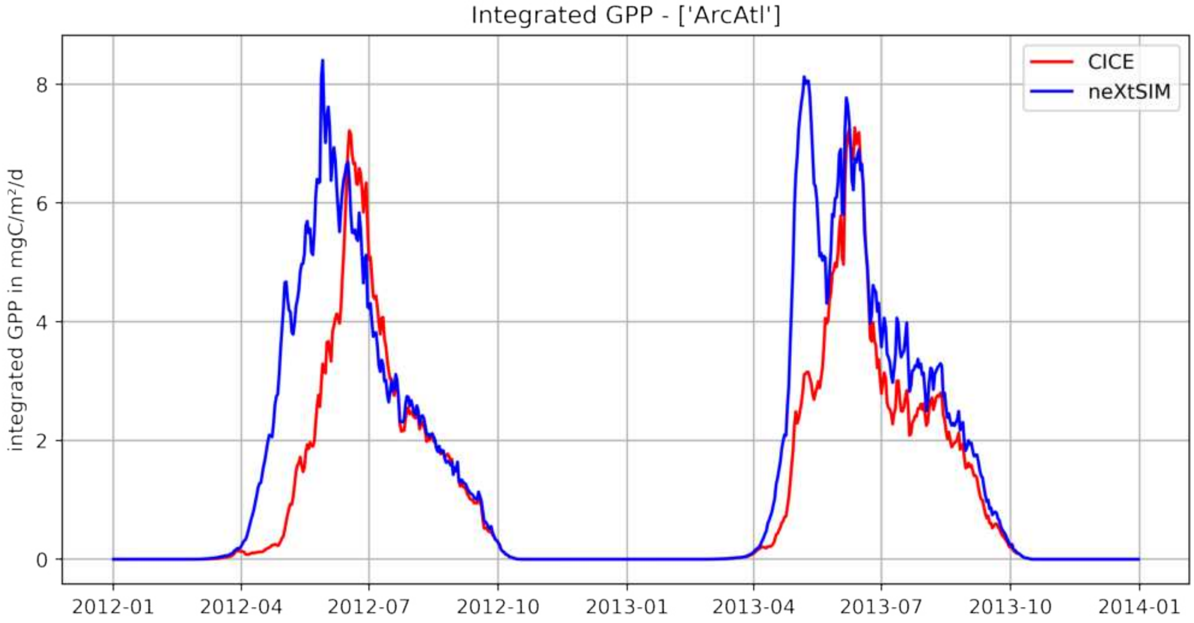

Figure 4.13: Time series of integrated GPP rates (in mg C m^{-2} d^{-1}) in the Arctic Atlantic region for 2012 to 2013 for both simulations, plotted as regional average from daily files.

The monthly maps of integrated GPP for March to June show distribution patterns that are comparable between simulations and years. For reference, the maps for spring 2012 from the neXtSIM-simulation are provided in Fig. 4.14. Primary production starts to appear in the southern extent of the region in March and April, and spreads further north and across the full region during May and June. The difference maps (not shown) indicate that integrated GPP rates

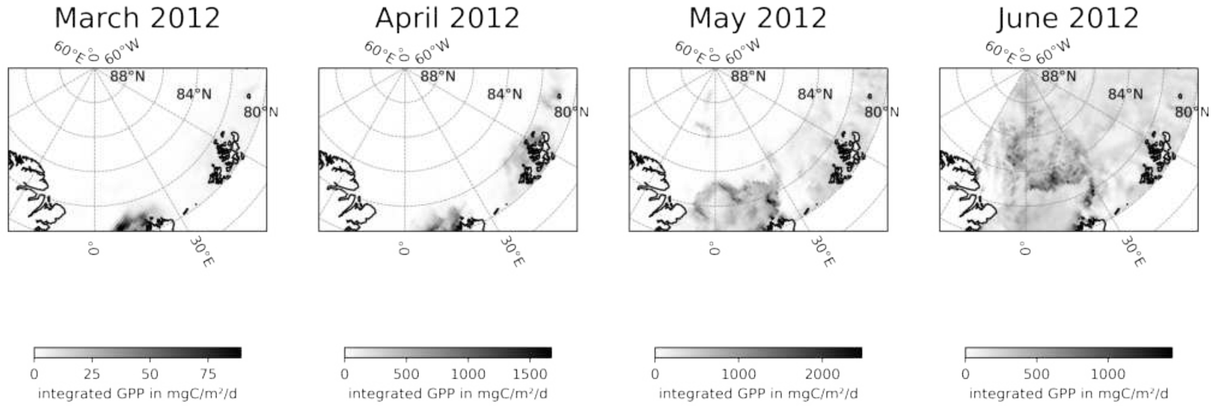

Figure 4.14: Maps of integrated GPP rates (in mg C m^{-2} d^{-1}) in the Arctic Atlantic region from the neXtSIM-simulation for March to June 2012, plotted from monthly mean files.

are higher in neXtSIM in the southern regions of the spring bloom onset in March and April of both years. The maps show an area north of Greenland that is more productive in CICE as of May in both years.

The daily time series for the light limitation factor, presented in Fig. 4.15 shows that light availability increases faster in neXtSIM compared to CICE at the end of March 2012, and that neXtSIM reaches the maximum of the light limitation factor (i.e. maximum of light availability) earlier. Peaks are comparable in both simulations in 2012. In 2013, both simulations reach their maximum light availability in June, but the peak is higher in neXtSIM compared to CICE.

The maps of the light limitation factor plotted for March to June (example for neXtSIM in 2012 provided in Fig. 4.16) show that light becomes available in the southern extents of the region first, while light availability is increasing across the full region in May and June. This pattern appears in both simulations and both years. The CICE-simulation shows a 'smoother' spread of light availability across the region, while neXtSIM exhibits a spatially more heterogeneous spread, as can be seen observed in Fig. 4.16.

The maps of difference between simulations for the light limitation factor, presented for 2012 in Fig. 4.17 show that neXtSIM is clearly less light limited in the southern extent during March and April of 2012. This difference is less pronounced towards the summer months, and in the year 2013.

The results of the linear regression analysis for integrated GPP predicted from light limitation are shown in Table 4.1. They indicate a significant correlation between the two variables.

The time series of the nitrate limitation factor (not shown) indicates that the neXtSIM-simulation is less nitrate limited compared to CICE. Both simulations show a decrease in limiting factor around May in both years and small values during the summer, reflecting nutrient depletion in the water column. The minimum values are smaller in 2013 compared to 2012. The maps plotted for the nitrate limitation factor (not shown) display that nitrate availability is high and uniformly distributed across the region, but decreases towards June in both years and simulations.

The spatially averaged time series of carbon export at 300 and 500 m depth (not shown)

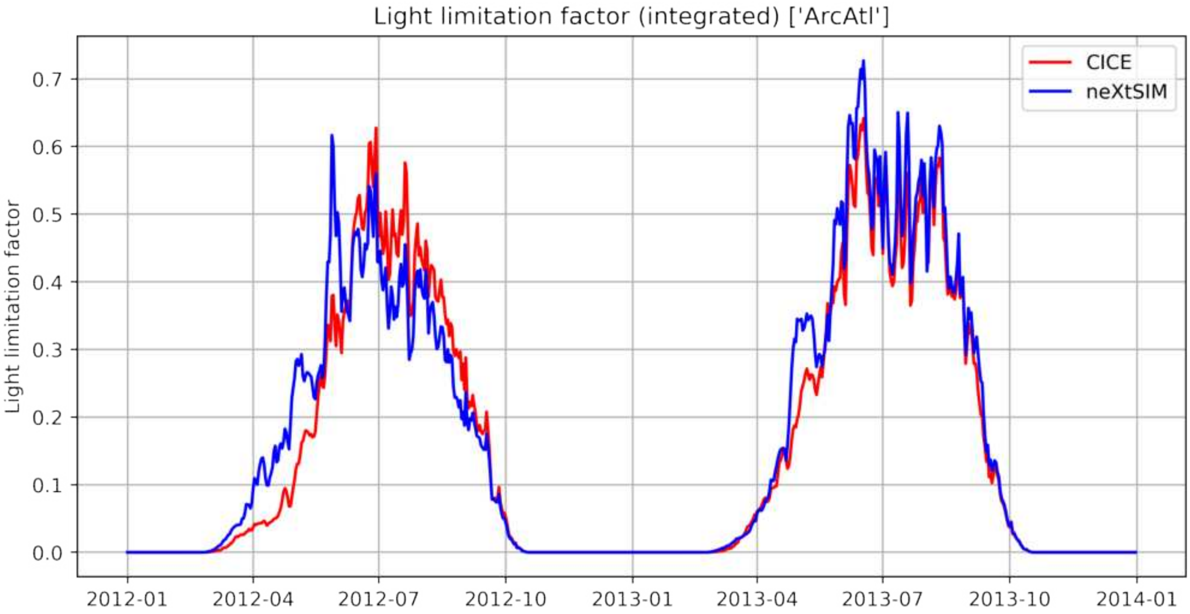

Figure 4.15: Time series of the light limitation factor (integrated over 100 m) In the Arctic Atlantic region for 2012 and 2013 for both simulations, plotted as regional average from daily files. Larger factors indicate lower levels of limitation.

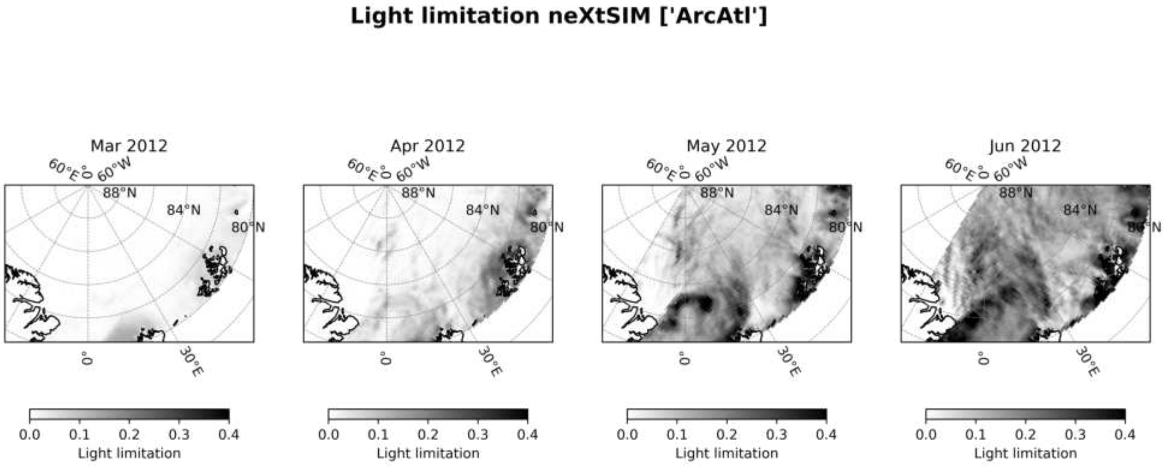

Figure 4.16: Maps of light limitation (integrated over 100 m) in the Arctic Atlantic region from the neXtSIM-simulation for March to June 2012, plotted from monthly mean files. Darker shading indicates higher light availability.

Table 4.1: R-values from linear regression analysis for integrated GPP for ArcAtl, using the light limitation factor as predictor variable (all p-values < 0.0001).

	2012		**2013**	
Month	**r CICE**	**r neXtSIM**	**r CICE**	**r neXtSIM**
March	0.45	0.65	0.61	0.76
April	0.47	0.52	0.56	0.46
May	0.51	0.58	0.49	0.61
June	0.33	0.56	0.26	0.49

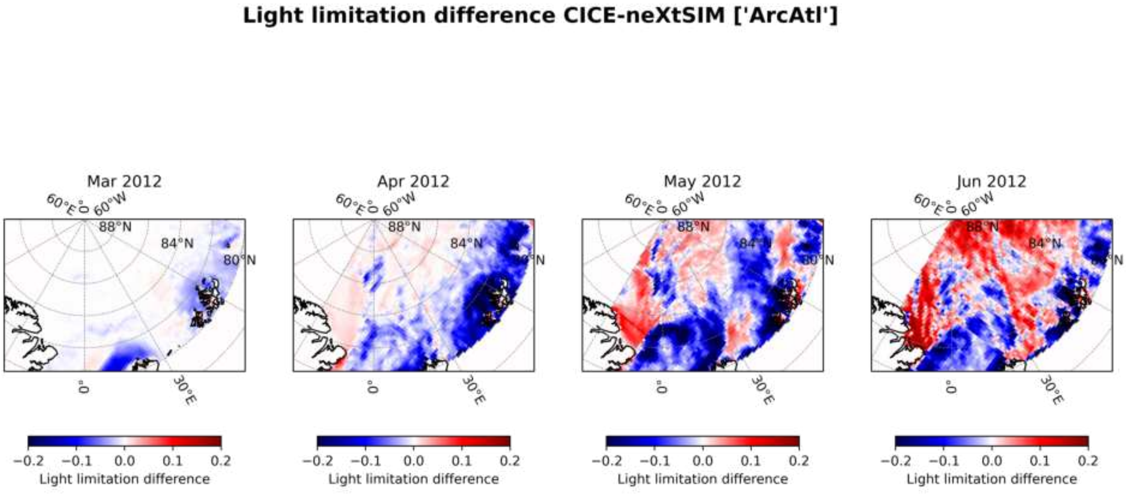

Figure 4.17: Difference maps (CICE minus neXtSIM) of light limitation (integrated over 100 m) in the Arctic Atlantic region for March to June 2012, plotted from monthly mean files. Red areas indicate higher light availability in CICE, blue areas indicate higher light availability in neXtSIM.

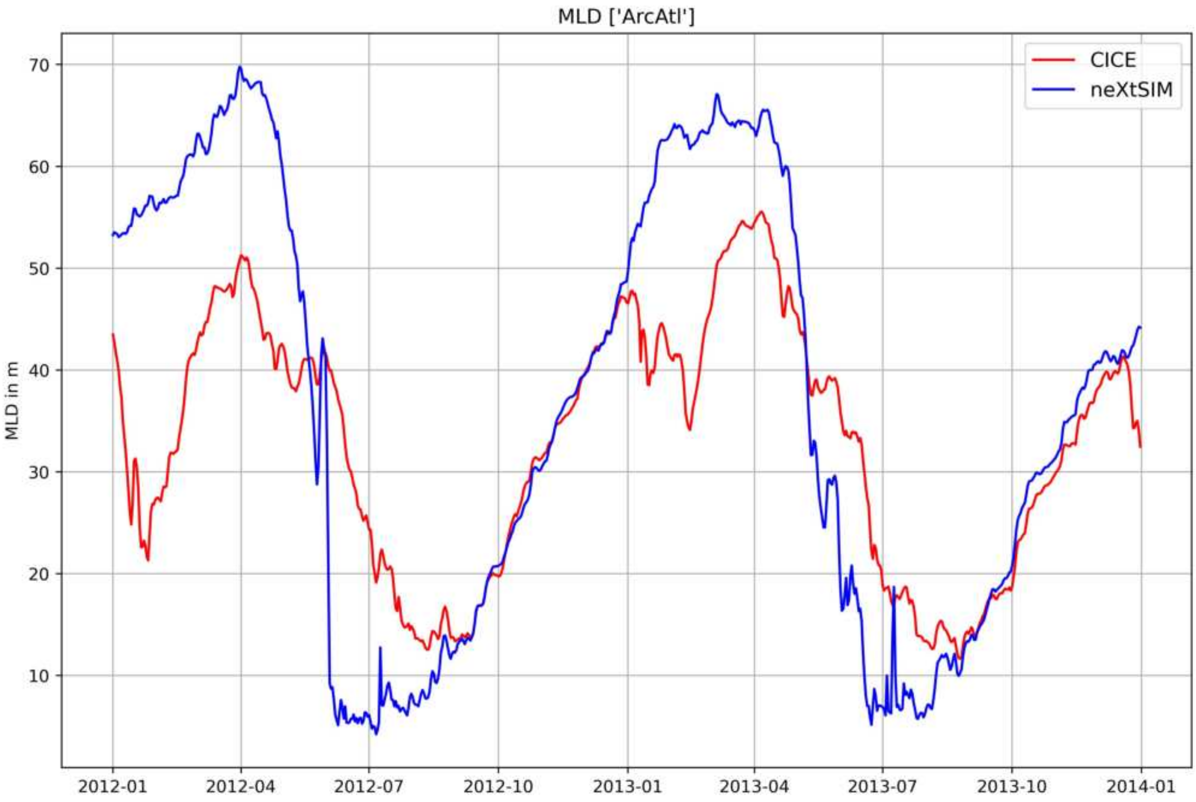

Figure 4.18: Time series of MLD in the Arctic Atlantic region for 2012 to 2013 for both simulations, plotted as regional average from daily files.

reveal that that maximum export rates are of the same magnitude in both simulations. Peak export rates are approximately 3.75 mol m^{-2} $^{-1}$ and 2.25 mol m^{-2} $^{-1}$ at 300 m and 500 m depth respectively. Peak export at 30 m is reached in September, and at 500 m in October of both years and in both simulations, although CICE lags lags slightly behind neXtSIM in 2012.

4.4.2 Mixed layer depth

The times series for the spatially averaged MLD plotted from daily data, presented in Fig. 4.18 shows that winter mixing is deeper in neXtSIM in both years, which reaches a MLD of 65 m depth. The maximum MLD is approximately 10 m shallower in CICE, which also shows an episode of considerable shoaling during winter. Spring shoaling in neXtSIM is more rapid, and the minimum MLD during summer is lower and longer in place compared to CICE.

The monthly maps of the MLD (see Fig. 4.19 as example from CICE in 2013) were plotted for January to June of both years and show variations in MLD of wave-like patterns. The neXtSIM-simulation shows similar MLD distribution between January and April in both years, and shoaling appears in May. The maps for the CICE-simulation show a more shallow MLD in January and February compared to March and April in both years. As can be seen in the map in Fig. 4.19, shoaling starts in May, but a large area of deeper mixing remains in the center of the Arctic Atlantic region. The same pattern is observed in 2012.

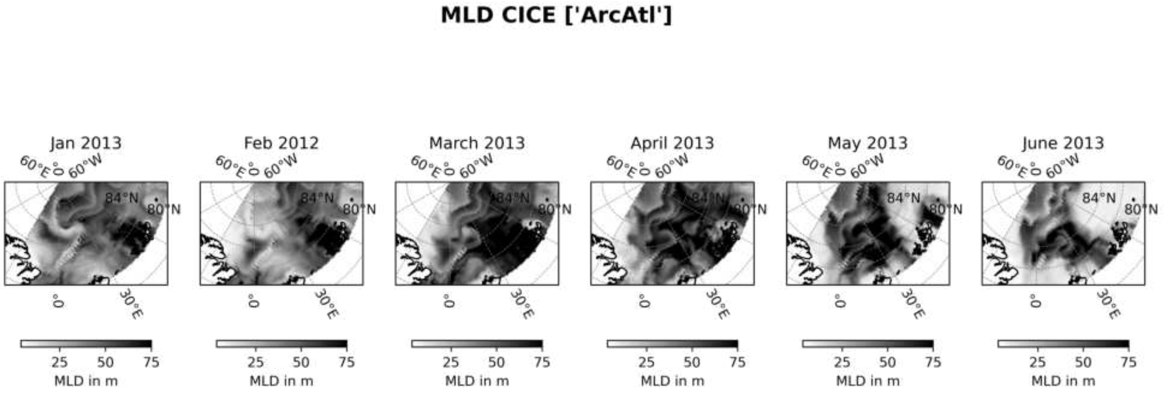

Figure 4.19: Maps of MLD (given in m depth) in the Arctic Atlantic region from the CICE-simulation for January to June 2013, plotted from monthly mean files.

4.4.3 Sea ice variables

The daily time series of the spatially averaged SIT (not shown) reveals that neXtSIM is thicker during both target years, reaching maximum values around 2 m (compared to 1.5 m in CICE) in June of both years. The SIT minima are lower in both simulations in 2013 compared to 2012. Summer SIT in CICE is 0.8 m in 2012, and approaches 0.6 m in 2013, while neXTSIM SIT approaches 1.0 m and 0.8 m in the summers of 2012 and 2013, respectively. The absolute decrease in SIT appears similar between simulations in each year.

The SIC time series in Fig. 4.20 shows that winter SIC are lower in neXtSIM (below 0.95) compared to CICE (approximately at 0.98) and also decrease more rapidly compared to CICE. Minimum SIC are approximately the same in both simulations and are lower during 2013 compared to 2012. The time series shows that temporal variability of SIC is stronger in neXtSIM during winter.

The maps of both sea ice parameters (not included) show smoother distribution of spatial variations in CICE compared to neXtSIM. SIT for the month of March to April show that both simulations model thick ice of SIT ≥ 2 m in proximity to the northern Greenland coast. Decline in SIC starts to appear along the southern boundaries of the region in both simulations during March and April in both years, and spreads across the region in May and June. The difference maps for SIC presented in Fig. 4.21 show that CICE keeps higher SIC along the southern boundaries of the region, particularly around the coasts of Svalbard and Franz Joseph Land (see map in Fig. 2.1(a) for direction). In May and June of both years, CICE shows higher SIC across most of the region, but concentrations are higher in neXtSIM along the coast of Greenland in June of both years.

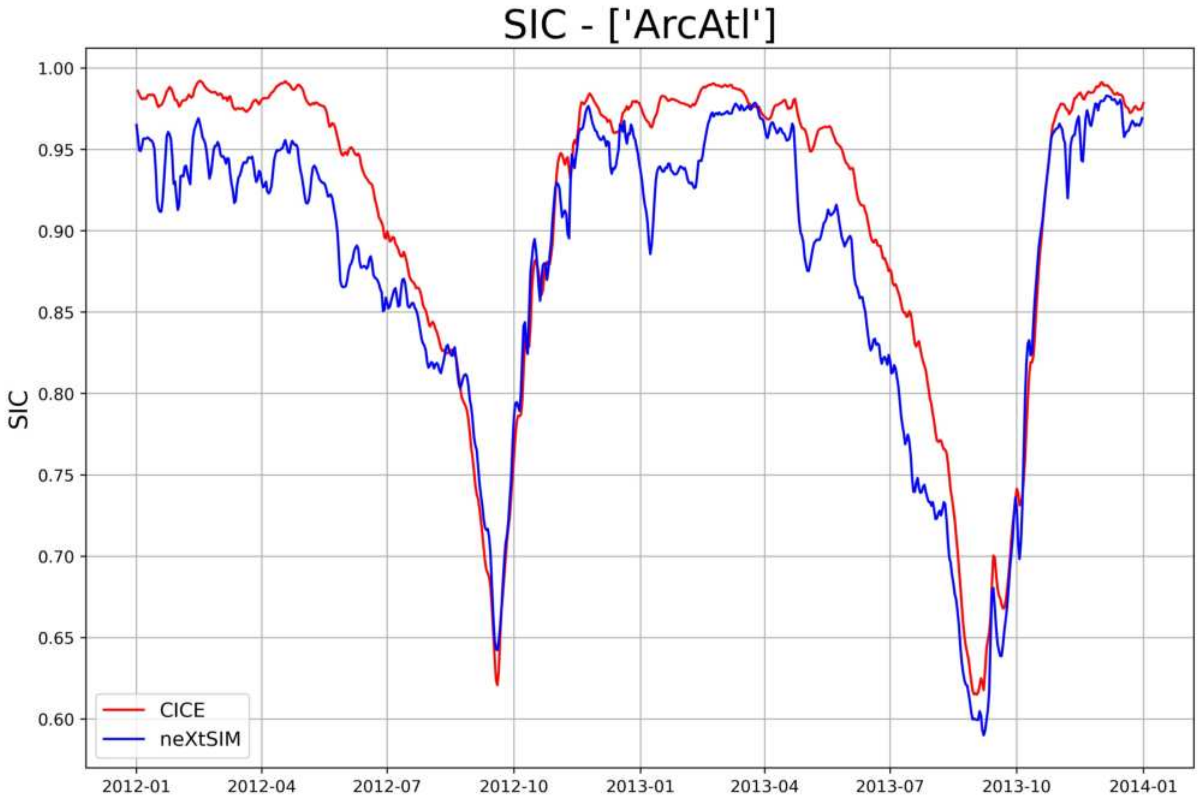

Figure 4.20: Time series of SIC for 2012 to 2013 for both simulations, plotted as regional average from daily file.

4.4.4 Summary of results

The neXtSIM-coupled model simulates overall higher rates of integrated GPP, and a stronger onset of the spring bloom in the southern parts of the Arctic Atlantic region. The simulation also shows earlier and stronger light availability, particularly in the south. Furthermore, the system is less nitrate limited in the neXtSIM-simulation. Winter mixing is deeper in the neXtSIM-simulation, which simulates more rapid shoaling during the spring. The neXtSIM sea ice model simulates thicker sea ice but lower sea ice concentrations. While the absolute melt of sea ice seems similar in both simulations, the drop in SIC is more rapid in neXtSIM, especially in the southern extents of the region.

4.5 Chukchi Sea

The Chukchi Sea is the inflow region of the Pacific water into the Arctic Ocean that lies directly at the Bering Strait. Sea ice is mostly exported from the region towards the eastern regions of the Arctic, and is either re-circulated in the Beaufort Gyre, or is exported by the Transpolar Drift via the Fram Strait into the Atlantic Ocean.

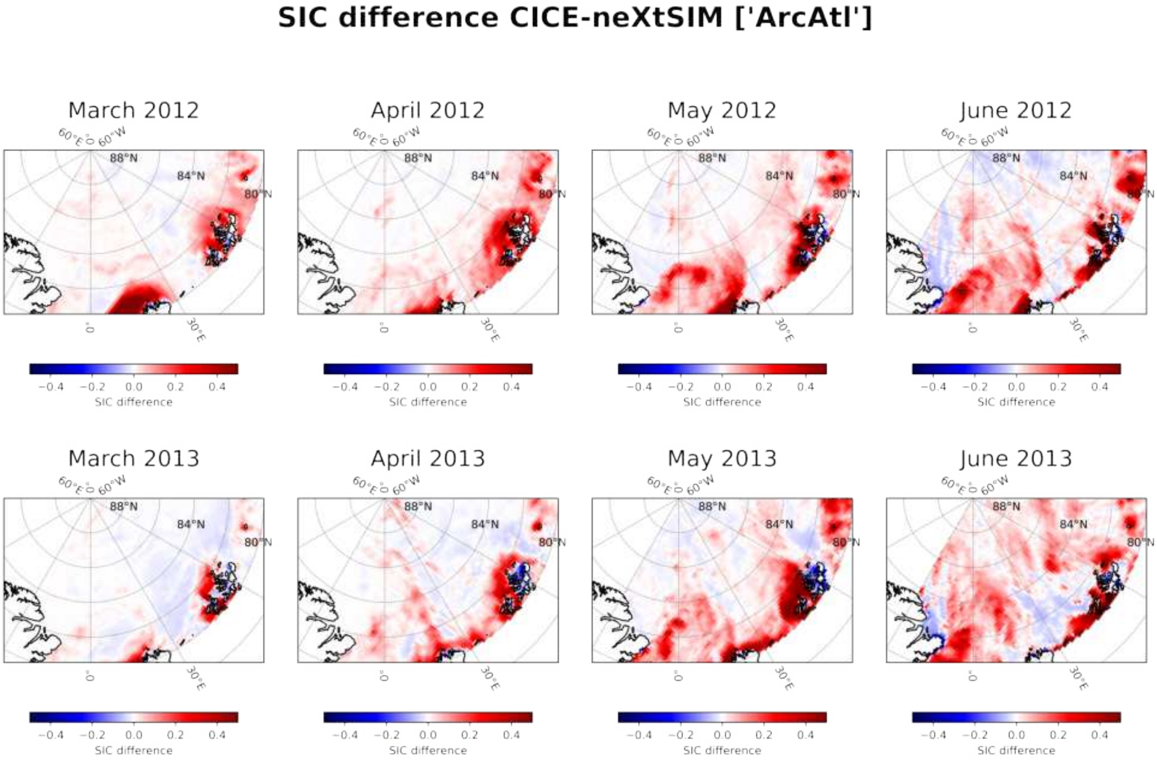

Figure 4.21: Difference maps (CICE minus neXtSIM) of SIC in the Arctic Atlantic region for March to June 2012, plotted from monthly mean files. Red areas indicate higher SIC in CICE, blue areas indicate higher SIC in neXtSIM.

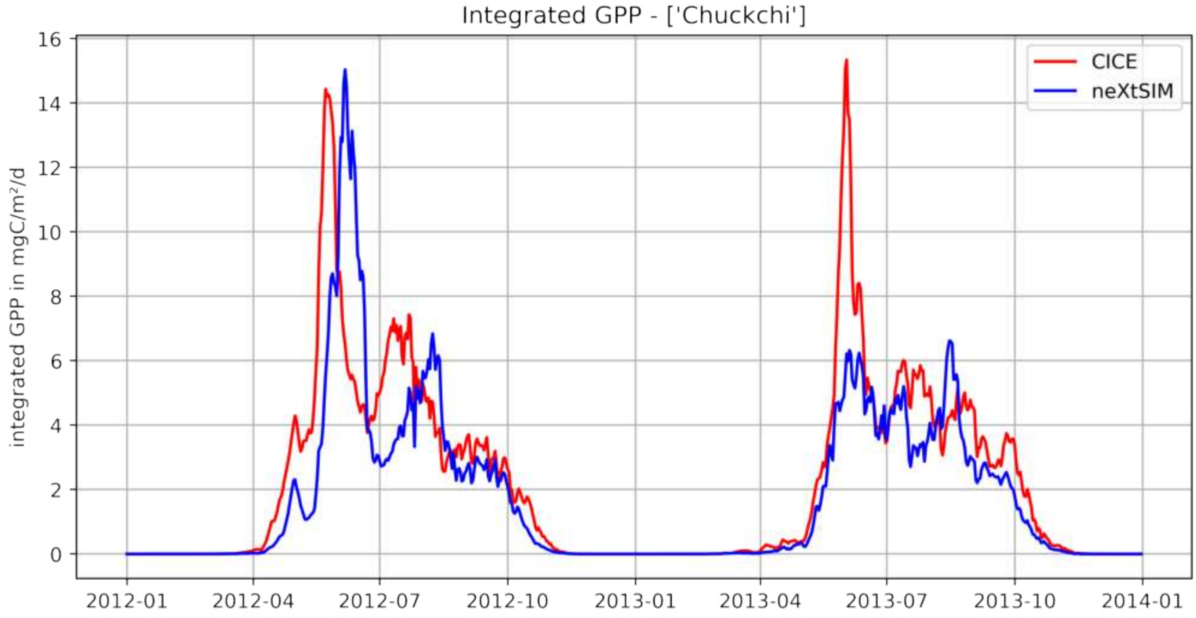

Figure 4.22: Time series of integrated GPP rates (in mg C m^{-2} d^{-1}) in the Chukchi Sea for 2012 to 2013 for both simulations, plotted as regional average from daily files.

4.5.1 Biogeochemical variables

As can be seen in the times series plot for integrated GPP in Fig. 4.22, the CICE-simulation shows an earlier spring bloom onset in 2012 compared to the neXtSIM-simulation. This difference in onset time is less pronounced in 2013. Peak values of daily production rates reach over 14 mg C m^{-2} d^{-1} and are aimilar in both simulations in 2012, although CICE reaches its peak earlier (May) than neXtSIM (June). Both simulations show a second smaller peak of primary production (approximately 7 mg C m^{-2} d^{-1}) in July (neXtSIM) and August (CICE) during that year. In 2013, the neXtSIM-simulation does not show a pronounced spring peak and rather homogeneously low daily production values in spring and summer.

Hovmöller diagrams plotted from the spatially averaged monthly files (not shown) indicate that primary production occurs to maximum depths of 110 m in both simulations during the low ice year 2012, while it occurs to depth of approximately 90 m in both simulations in 2013.

The maps of the monthly integrated GPP for the months of March to June (see Fig. 4.23 as example for neXtSIM 2012) show similar distribution patterns for both simulations. The onset of the spring bloom can be observed along the Alaskan coast in March and April, and primary production spreads across most of the region in May and June. The very low integrated GPP rates in the Kotzebue Sound (west of the Bering Strait) in both simulations is noteworthy.

The difference maps (not shown) for both years show that integrated GPP is stronger in CICE in April and May across most of the Chukchi Sea. This is also the case in June 2013, whereas in June 2012 there are also larger areas of higher PP in neXtSIM compared to CICE.

The time series for the light limitation factors (see Fig. 4.24) shows bell-shaped curves for both simulations. The increase of the light limitation factor (i.e. the increase of light availability)

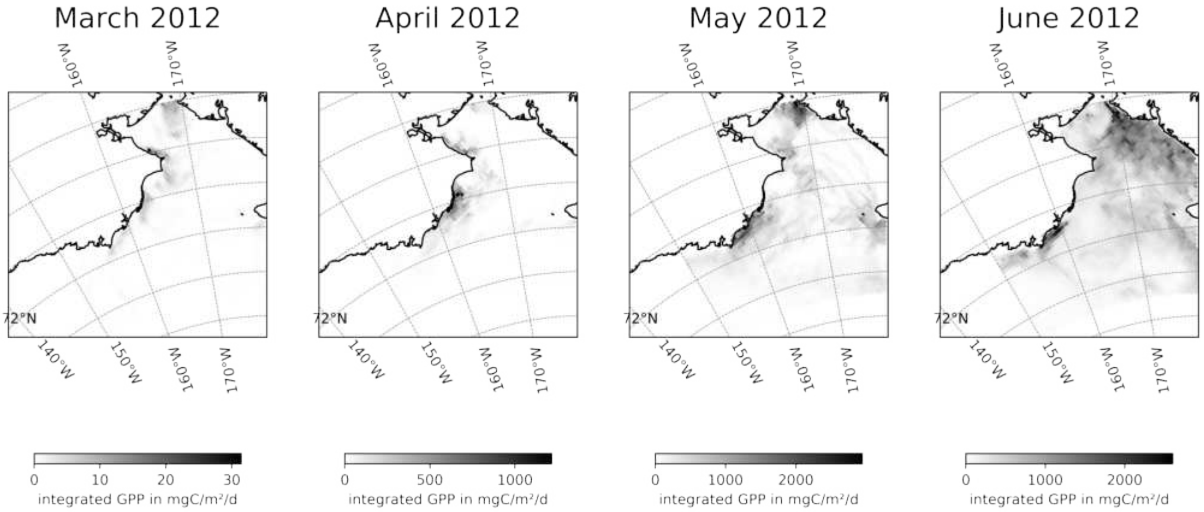

Figure 4.23: Maps of integrated GPP rates (in mg C m^{-2} d^{-1}) in the Chukchi Sea from the neXtSIM-simulation for March to June 2012, plotted from monthly mean files.

starts in March and shows a faster increase in CICE in both years. The CICE-simulation appeares to be less light limited during both years. The maximum values for light availability achieved in both simulations are higher in 2012 compared to 2013.

Light limitation maps show that the region is largely light limited (limiting factor < 0.1) during March in both simulations and years, and that limitation decreases towards June. A comparison between the maps of CICE and neXtSIM presented in Fig. 4.25 and Fig. 4.26 for the year 2012 shows that the light limitation factor increases more 'smoothly' in the CICE-simulation. This is also observed in 2013. Kotzebue Sound shows strong light limitation until June in both years and simulations. The difference maps plotted for the light limitation factor (see Fig. 4.27 as example for 2012) confirm that CICE is less light limited during all months and in both years.

The nitrate limitation time series (not shown) shows higher values for the limiting factor (i.e. less limitation) from January until the end of April, and after October in both simulations and years. The factors decrease in May and remain low during the summer months, representing a stronger degree of nitrate limitation caused by consumption. CICE appears more limited during both summers, and both simulations show stronger limitation in 2013 compared to 2012.

Nitrate limitation maps (see Fig. 4.28 as example for neXtSIM 2012) for both simulations and years show a divide of the region. The southern extent of the Chukchi Sea is more nitrate limited compared to the northern extent. The difference maps (see Fig. 4.29 for 2012) show that nitrate availability is higher in CICE in March and April in the southern and more eastern extent of the region. Apparent is also a corner of very low nitrate limitation in CICE at the north western boundary of the region together with a 'belt' of less nitrate limitation in neXtSIM.

The spatially averaged daily time series of carbon export, shown in Fig. 4.30 for 300 m depth, reveals that peak export rates of 3.5 mol m^{-2} $^{-1}$ in CICE appear earlier than in neXtSIM (approximatley 4 mol m^{-2} $^{-1}$) in 2012. A peak export rate appears to be missing in neXtSIM in 2013. A similar pattern shows at 500 m, where peak export rates larger than 2 mol m^{-2} $^{-1}$ appear

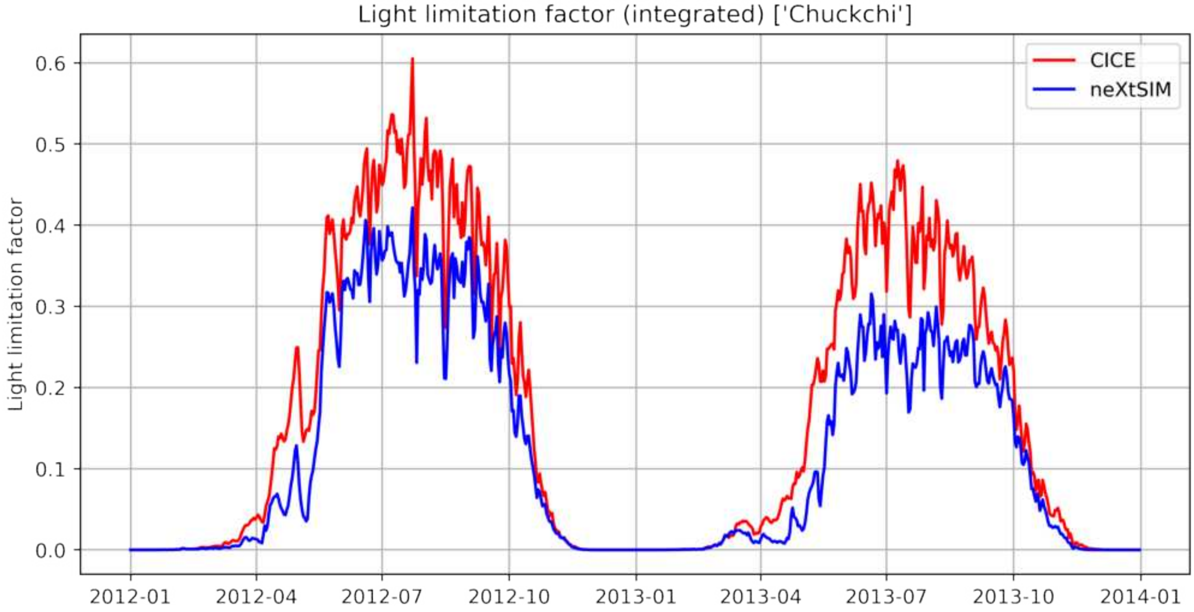

Figure 4.24: Time series of the light limitation factor (integrated over 100 m) in the Chukchi Sea for 2012 and 2013 for both simulations, plotted as regional average from daily files. Larger factors indicate lower levels of limitation.

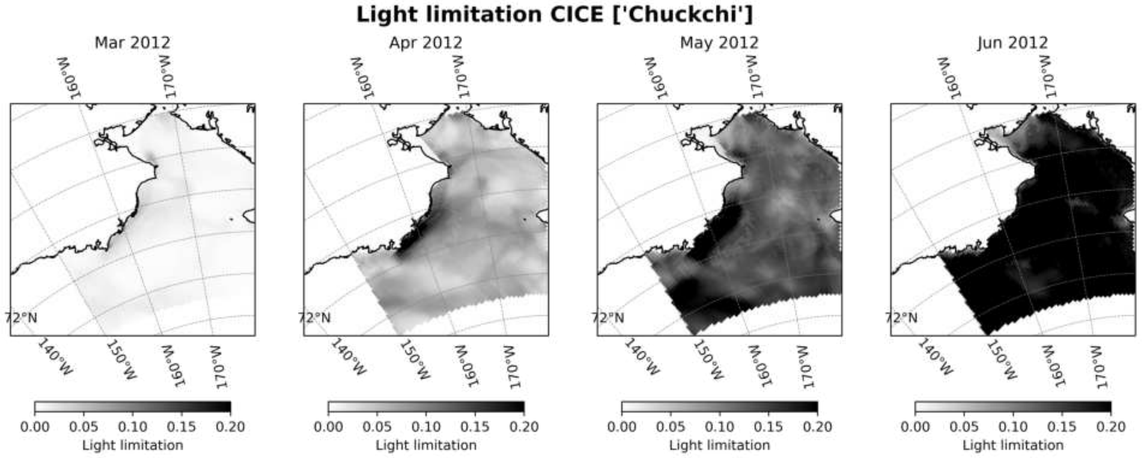

Figure 4.25: Maps of light limitation (integrated over 100 m) in the Chukchi Sea from the CICE-simulation for March to June in 2012, plotted from monthly mean files. Darker shading indicates higher light availability.

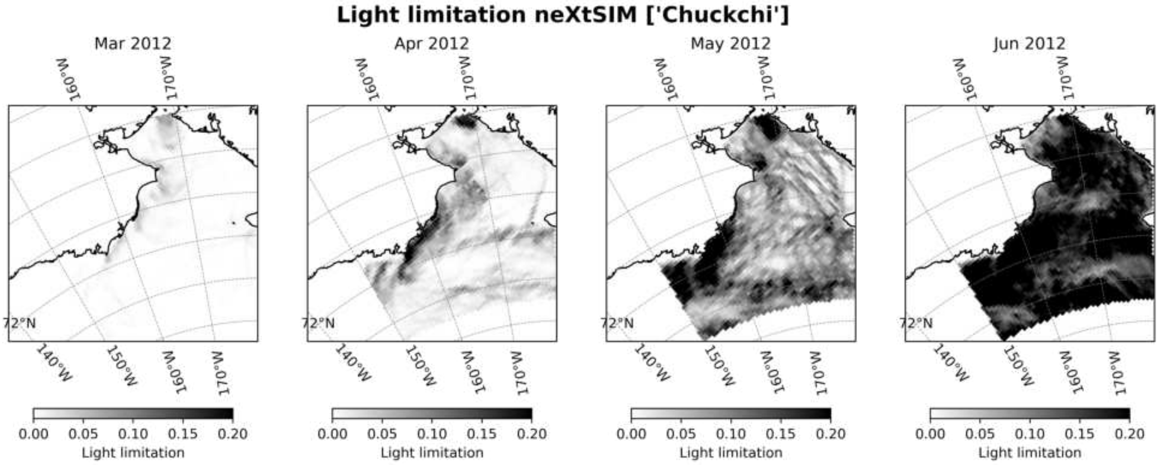

Figure 4.26: Maps of light limitation (integrated over 100 m) in the Chukchi Sea from the neXtSIM-simulation for March to June in 2012, plotted from monthly mean files. Darker shading indicates higher nitrate availability.

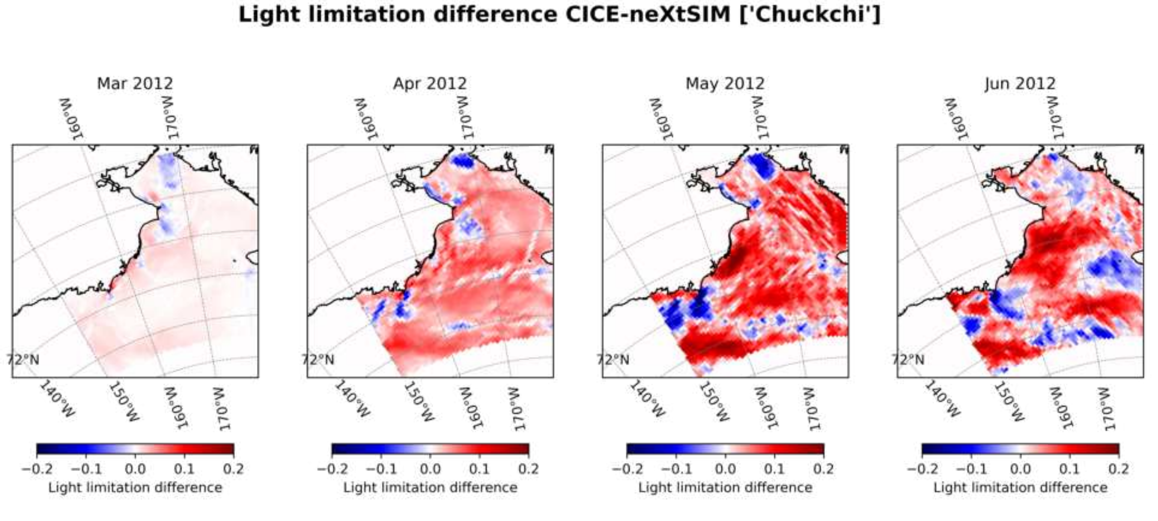

Figure 4.27: Difference maps (CICE minus neXtSIM) of light limitation (integrated over 100 m) in the Chukchi Sea for March to June 2012, plotted from monthly mean files. Red areas indicate higher light availability in CICE, blue areas indicate higher light availability in neXtSIM.

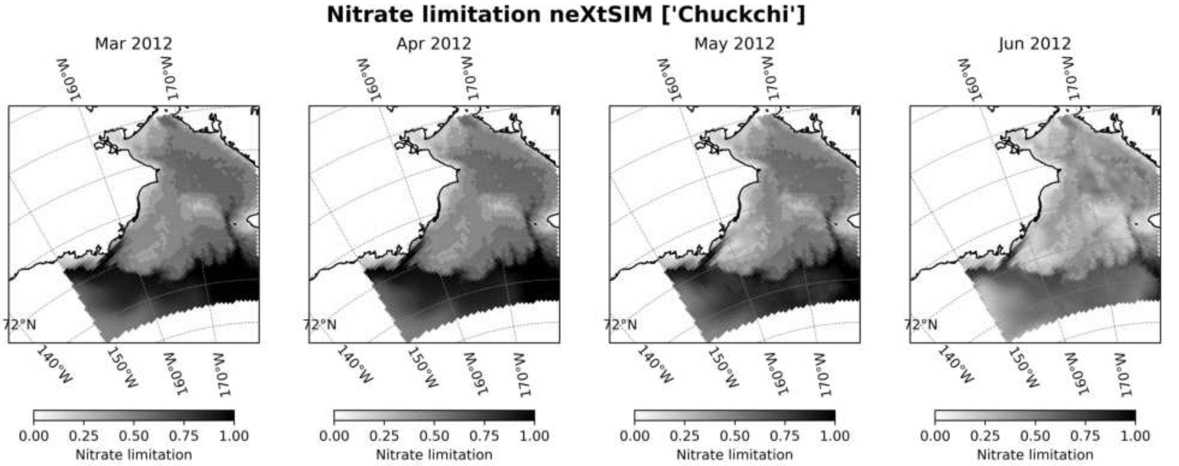

Figure 4.28: Maps of nitrate limitation (integrated over 100 m) in the Chukchi Sea from the neXtSIM-simulation for March to June in 2012, plotted from monthly mean files. Darker shading indicates higher nitrate availability.

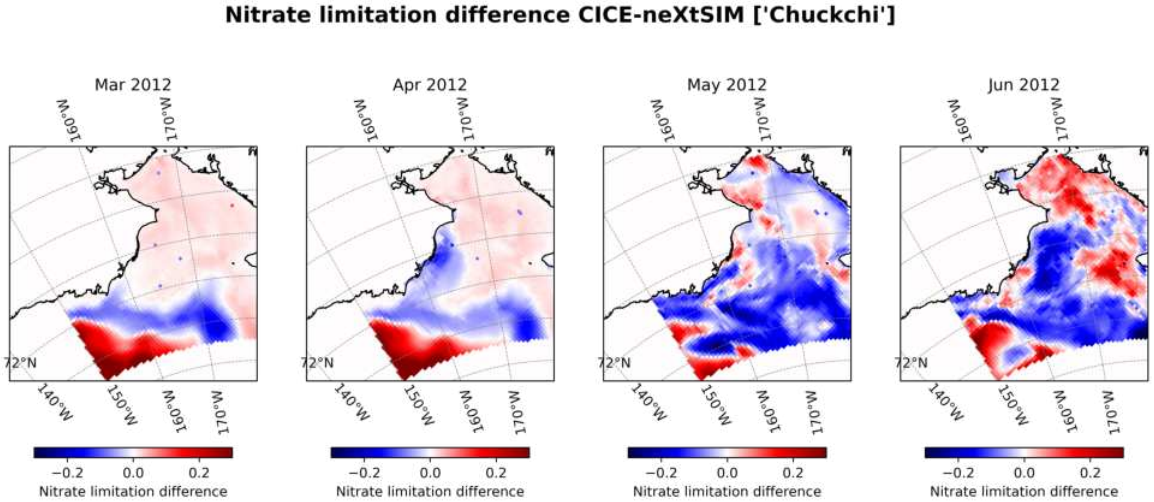

Figure 4.29: Difference maps (CICE minus neXtSIM) of nitrate limitation (integrated over 100 m) in the Chukchi Sea for March to June 2012, plotted from monthly mean files. Red areas indicate higher nitrate availability in CICE, blue areas indicate higher light availability in neXtSIM.

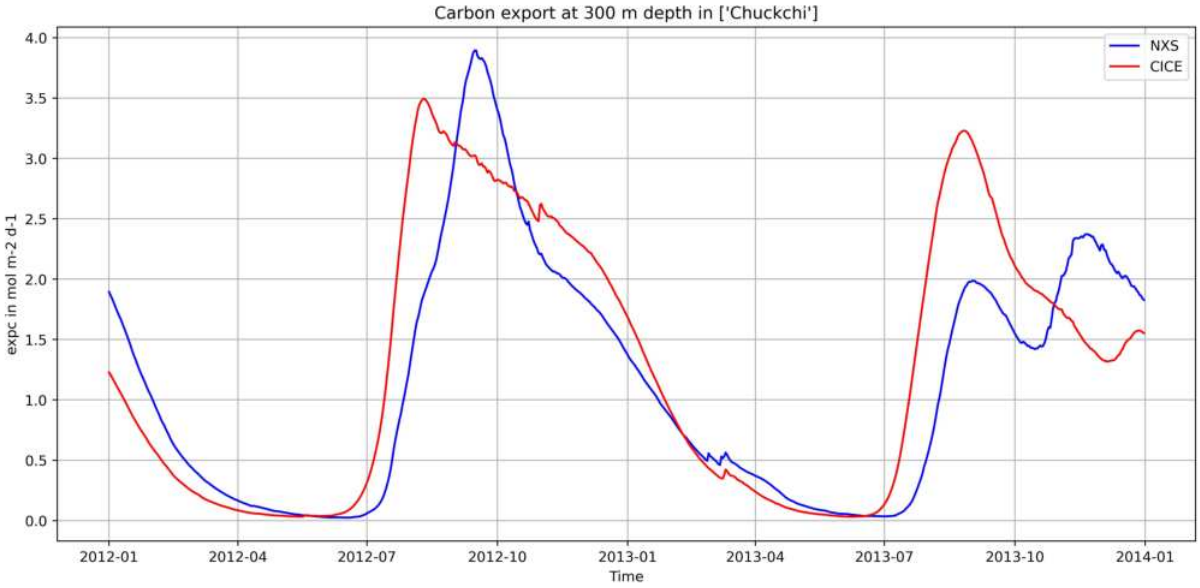

Figure 4.30: Time series of carbon export (in mol m^{-2} $^{-1}$) at 300 m depth for both simulations, plotted as regional average from daily files.

in October 2012 in both simulations. In 2013, export rates are similar in CICE to the previous year, while export rates in neXtSIM increase towards the end of the year. The time seires also shows a light lag of neXtSIM behind CICE.

4.5.2 Mixed layer depth

The daily time series of the MLD for the target years, presented in Fig. 4.31 shows that neXtSIM has a deeper winter mixed layer in January to April in 2012, while maximum depth in both simulations is approximately 35 m. Shoaling starts earlier in neXtSIM and the shallow mixed layer remains longer in place in both years.

Maps for the MLD were plotted from the monthly averaged files for January to June, to include the months of the deep winter mixing. Fig. 4.32 was included as example from the neXtSIM-simulation for the year 2012. Both simulations show that the areas of shallow mixed layer (MLD $<$ 40 m) increase towards the month of June. The difference maps (not shown) reveal that neXtSIM simulates a deeper mixed layer in the northern extent of the Chukchi Sea during January to March, while mixing is deeper in CICE in the south. Towards June, most of the region has a deeper mixed layer in CICE.

4.5.3 Sea ice variables

The daily time series of SIT for the target years (not included) show that SIT is larger in CICE throughout 2012 and 2013. The winter maxima of approximately 3.5 m (CICE) and 2.5 m (neXtSIM), are larger in 2012 compared to 2013. Summer minima are lower in 2012, where both simulations drop below SIT of 0.5 m. Thickness decrease starts approximately at the same time

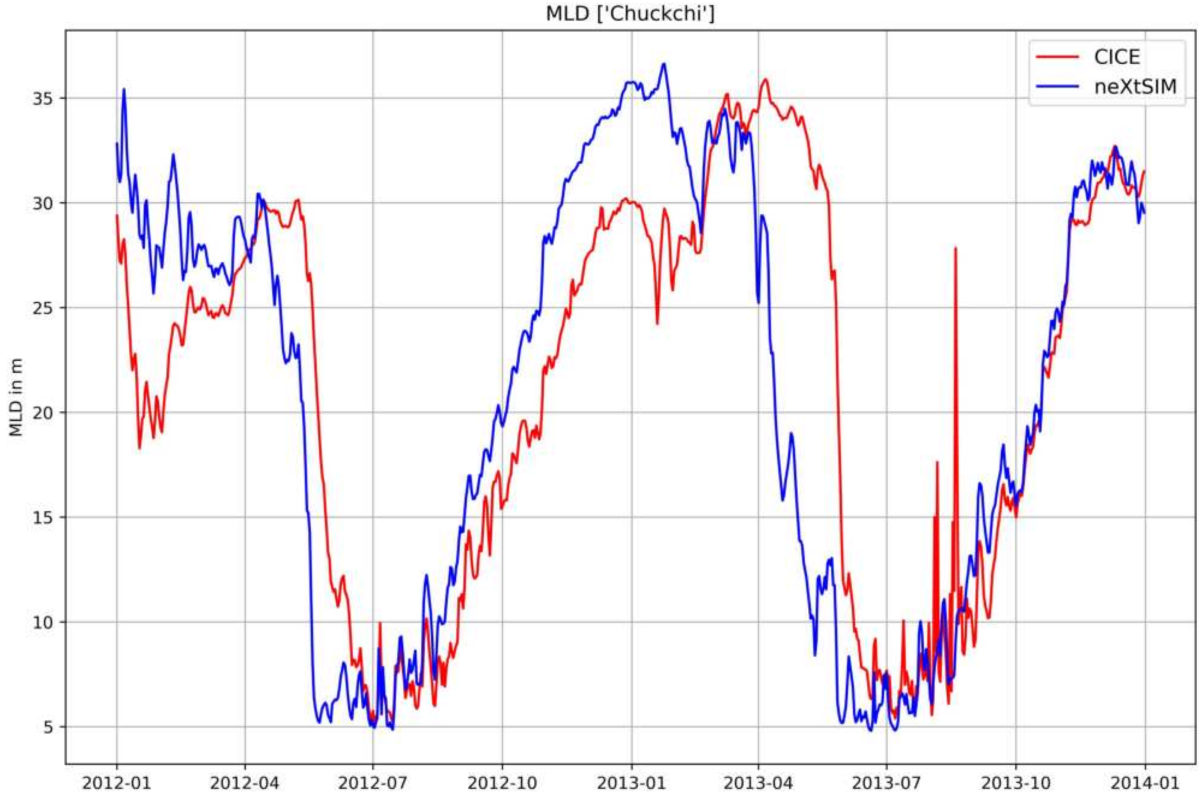

Figure 4.31: Time series of MLD in the Chukchi Sea for 2012 to 2013 for both simulations, plotted as regional average from daily files.

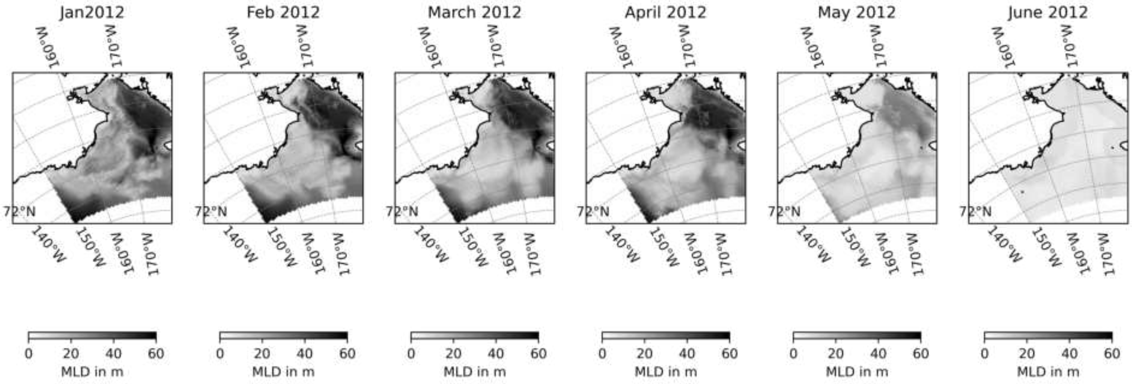

Figure 4.32: Maps of MLD (given in m depth) in the Chukchi Sea from the neXtSIM-simulation for January to June 2012, plotted from monthly mean files.

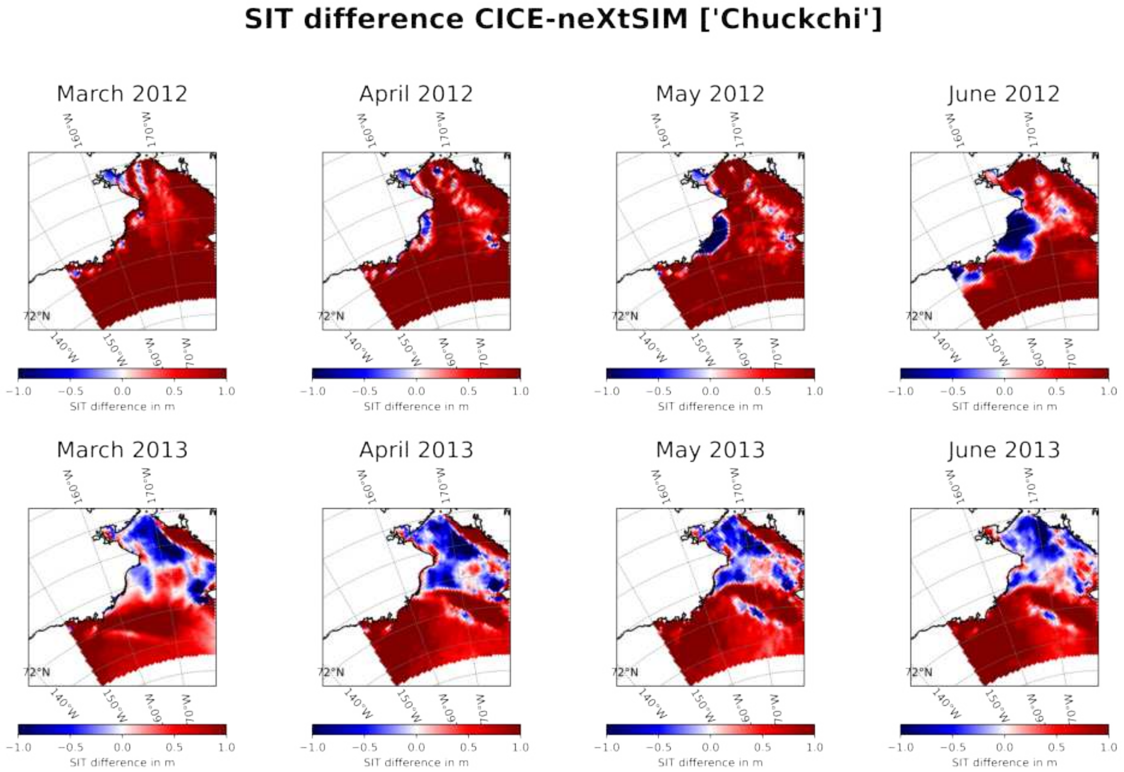

Figure 4.33: Difference maps (CICE minue neXtSIM) of SIT in the Chukchi Sea for March to June of both years, plotted from monthly mean files. Red areas indicate thicker ice in CICE, blue areas indicate thicker ice in neXtSIM.

in May of both years, but CICE shows a considerably stronger SIT decrease than neXtSIM until the end of June in both years. The maps of the SIT (not included) show that both sea ice models simulate large areas of SIT thicker than 2 m. Areas of thinner sea ice are mostly located along the Alaskan coast, and both simulations show larger areas of thinner sea ice in 2013 compared to 2012. The difference maps presented in Fig. 4.33 show that CICE is thicker than neXtSIM almost everywhere in the region in 2012, except for an area along the Alaskan Coast. In 2013, SIT in neXtSIM is larger in the more southern extent of the Chukchi Sea.

The time series of SIC (not included) show similar curves for both simulations, and maximum SIC during winter approach 1. Minimum summer SIC are lower in both simulations in 2012 (approaching 0.1) compared to 2013 (approaching 0.3). CICE shows a more rapid decrease in SIC. The monthly average maps of SIC for March to June presented in Fig. 4.34 and Fig. 4.35 show that SIC in neXtSIM are spatially more heterogeneous, while differences in CICE appear to be simulated more smoothly. In March and April of both years, SIC are homogeneously larger than 0.9 in CICE, whereas spatially distinct areas of SIC below 0.9 start to appear mainly along the Alaskan coast and close to the Bering Strait in neXtSIM. In May and June, SIC below 0.9 start to spread across the full region in both simulations, except in the area of Kotzebue Sound. The difference maps for SIC (not included) show that CICE has slightly higher SIC in March of both years in the south of the region. The largest differences in SIC appear along the Alaskan

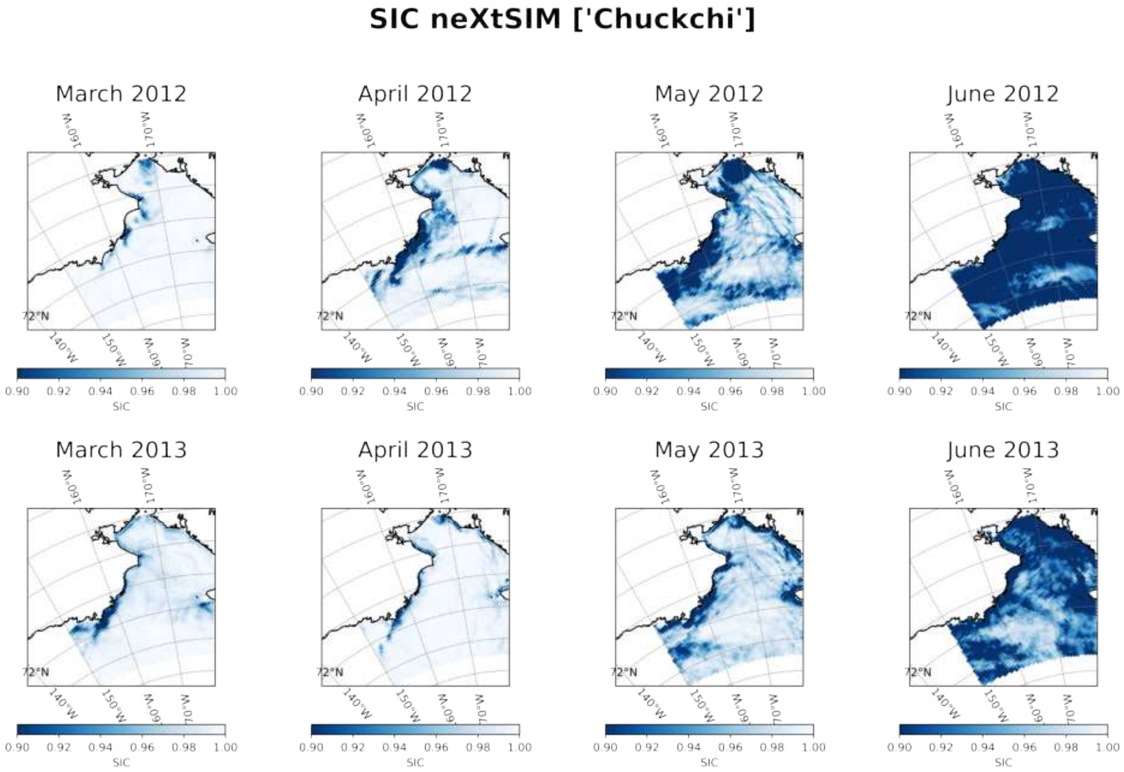

Figure 4.34: Maps of SIC in the Chukchi Sea from the neXtSIM-simulation for March to June of both years, plotted from monthly mean files.

coast in May and June 2013, and along the Siberian coast in June 2013, where neXtSIM has much higher SIC than CICE. Linear regression analysis was performed for SIC as predictor of integrated GPP. The r-values (all p-values < 0.0001) are presented in Table 4.2. A significant correlation between the variables was found during multiple months in both simulations.

4.5.4 Summary of results

In the Chukchi Sea, HYCOM-ECOSMO simulates higher GPP rates when coupled to the CICE sea ice model. In this simulation, also the light availability increases stronger at the beginning of spring and is higher in most of Chukchi Sea during the growth season compared to neXtSIM. The CICE-simulation shows higher nitrate availability in large areas towards the south in March and April. While neXtSIM shows deeper winter mixing earlier during the year, CICE shows a deeper mixed layer than neXtSIM in the southern extents of the region.

Sea ice is thicker in CICE and the loss of thickness is stronger in the CICE-simulation until June in both years. The CICE-simulation also shows a more rapid decline in SIC in both years during spring.

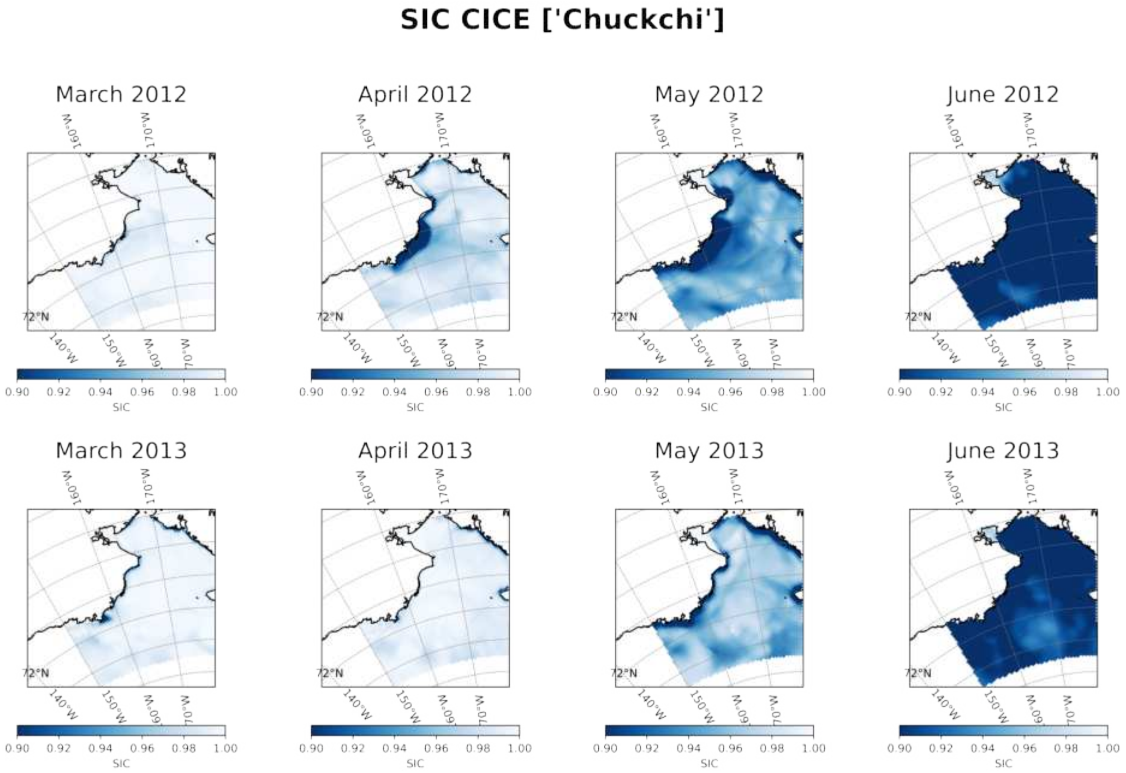

Figure 4.35: Maps of SIC in the Chukchi Sea from the CICE-simulation for March to June of both years, plotted from monthly mean files.

Table 4.2: R-values from linear regression analysis for integrated GPP for Chukchi Sea, using the SIC as predictor variable (all p-values < 0.0001).

	2012		**2013**	
Month	**r CICE**	**r neXtSIM**	**r CICE**	**r neXtSIM**
March	-0.2596	-0.4899	-0.3059	-0.5091
April	-0.4517	-0.4060	-0.4119	-0.2532
May	-0.1829	-0.3150	-0.2151	-0.3990
June	-0.2050	-0.0285	-0.0763	-0.0338

Chapter 5

Discussion

The differences in primary production rates and associated limiting factors between simulations were investigated in the regions Barents Sea, Arctic Atlantic and Chukchi Sea. To understand whether the different rheologies of the coupled sea ice models influence primary production in HYCOM-ECOSMO, differences in the sea ice parameters ’thickness’ and ’concentration’ were considered during the analysis. The result for each region are discussed in the following chapter, which is concluded with remarks on the similarities between the regions.

5.1 Barents Sea

5.1.1 Ice-edge bloom

So-called ice edge blooms can be observed in all polar regions, and have been estimated to generate approximately 50 % to 65 % of the annual primary production in the Barents Sea (Druzhkova et al., 2020). It has been found that these ice-edge associated blooms are driven by higher light availability in these areas of lower SIC. Furthermore, the mixed layer depth tends to be shallower underneath the sea ice, which can increase light exposure of phytoplankton and lead to more favorable distribution of the micro-algae in relation to their grazers (Druzhkova et al., 2020; Sakshaug & Slagstad, 1992).

The maps of integrated GPP for March in both simulations and years (see example from neXtSIM for 2012 in Fig. 4.4) show that the areas of the spring bloom onset roughly align with the boundaries of the sea ice extent, i.e. the area of SIC $>$ 15 % shown in Fig. 4.7. Furthermore, it can be observed in the MLD maps in Fig. 4.11, that vertical mixing is less deep in the areas underneath the sea sea ice extent. This is true in both simulations and shows that both coupled models simulate the conditions that affect the spring bloom in an ice edge area.

5.1.2 Magnitude of integrated GPP

It can be observed in the maps for March of both years and simulations (see Fig. 4.4 as example from neXtSIM 2012) that the productivity of the spring bloom is higher along the southern ice edge compared to the northern ice edge. Such north-south gradients have been described for the Barents Sea by Sakshaug & Slagstad (1992). They can either be related to an earlier increase in light availability in the south, or due to earlier mixed layer shoaling from freshwater influx into the upper ocean. Both of these factors are related to an earlier increase in incoming solar radiation in the lower latitudes in spring. SIC is know to have an inverse relationship with light availability and melt water influx. Whether differences in the sea ice characteristics between models can therefore explain differences in integrated GPP in the Barents Sea will be discussed in the following section.

The maps of difference in integrated GPP (see Fig. 4.5 for 2012 as example) show that CICE simulates higher production rates during the spring bloom onset in March along the ice edge, and in the central and southern regions of open water. In April, neXtSIM shows higher production rates underneath the sea ice extent.

Judging from the difference maps of light limitation (see Fig. 4.9 for 2012), light availability is higher in neXtSIM underneath the sea ice in the northern extent of the region during March to June, and is also higher across large areas underneath the southern sea ice extent in March and April. This corresponds to lower SIC in neXtSIM in these areas (see Fig. 4.8), and higher integrated GPP rates in Apri (see Fig. 4.5 for 2012). The larger integrated GPP rates in CICE observed during March along the ice edge are likely related to the fact that light can penetrate through the thin sea ice in CICE, which increases light availability during early spring in the CICE-simulation.

Underneath the northern sea ice extent, the mixed layer shoaling in spring appears to be stronger in neXtSIM between April and May, as can be seen in the maps of the MLD difference presented for 2012 as an example (see Fig. 4.12). Considering the faster SIT decrease in neXtSIM as seen in the time series (Fig. 4.6), the larger volumes of freshwater influx in neXtSIM starting in April likely increase the stratification and enhance phytoplankton distribution in the water column. The stronger melt may be enhanced by lower SIC in neXtSIM. The effect of freshening may further be influenced by differences of sea ice salinity between simulations.

Since wind forcing is stronger in the neXtSIM (1-hourly) compared to the CICE-simulation (6-hourly), it cannot be excluded that stratification in neXtSIM may be enhanced by larger influx volumes of the fresher Arctic water masses from the north (see East Spitzbergen Current (ESC) and Bear Island Current (BIC) in the circulation map in Fig. 2.1(b)) (Kohlbach et al., 2025)). This may also explain the lower integrated GPP rates in the neXtSIM-simulation in the central areas of the region, as the polar water would decrease the influence of the warm, more saline and nutrient-rich inflow waters from the Atlantic Ocean.

The results discussed above suggest that the difference in sea ice models influence the primary production in the Barents Sea region to a certain extent. The effect of light flux through ice in the CICE-simulation influences the spring bloom onset, but becomes negligible during later months of spring in the Barents Sea, when the already low SIC are decreasing further. The differences in SIT and SIC and related influx volumes of melt water appear to affect upper ocean stratification in the area of the sea ice extent. This seems to contribute to the differences in primary production rates between simulations during April.

5.2 Arctic Atlantic

5.2.1 Spring bloom and primary production magnitude

For the Arctic Atlantic region, the results show that the spring bloom onset happens earlier in the neXtSIM-simulation (see Fig. 4.13). Peak production rates are reached earlier and are higher compared to the CICE-simulation, and neXtSIM also shows two production peaks in 2013. All of this implies that HYCOM-neXtSIM-ECOSMO simulates higher productivity of phytoplankton in the Arctic Atlantic region. Hence, it is expected that the neXtSIM-simulation is less light limited, that water column stratification commences earlier, and that the simulation may also show lower nitrate limitation. To confirm these assumptions, first the time series of the light and nitrate limitation factors are compared to the integrated GPP plot.

The times series of light limitation (see Fig. 4.15) show that light becomes available earlier and increases more strongly in neXtSIM at the end of March in 2012, which aligns well with the earlier spring bloom onset. The timing of light availability is less different between simulations in April 2013, which is also reflected in a shorter delay of spring bloom onset in CICE in April 2013 compared to 2012. Light limitation factors (i.e. light availability) are higher in neXtSIM in 2013 compared to 2012, and remain higher for longer during spring and summer, which appears to trigger the second production peak in 2013 in the neXtSIM-simulation.

Productivity drops considerably after June in both simulations and years, even though the light availability still shows smaller peaks in July and August. The drop in productivity coincides with the drop in nitrate limitation seen in the time series (not shown).

Correlation analysis yields significant r-values for the light limitation factor as predictor for integrated GPP shown in Table 4.1. R-values for the neXtSIM-simulation are larger than 0.45 (all p-values < 0.0001) during all months, and are higher compared to the values for the CICE-simulation except in April 2013. R-values in CICE are larger than 0.4 during all months, except in June 2012 and 2013, when they drop below 0.34. Linear correlation between integrated GPP and nitrate limitation is less significant (all r-values < 0.3, all p-values < 0.0001). Nevertheless, largest values are achieved in June in both simulations.

This confirms that in the Arctic Atlantic region, the spring bloom onset and productivity during spring is more dependent on light availability, while during the later months of the growth season productivity may be increasingly depending on nitrate availability. This aligns with observations from the Arctic Ocean (Ardyna & Arrigo, 2020).

5.2.2 Light availability and sea ice parameters

To understand how the difference in sea ice behavior influence differences in light availability and primary production, time series and maps of the light limitation factor and integrated GPP were compared to plots of SIT and SIC.

The daily time series of light limitation (see Fig. 4.15) show that the CICE-simulation reaches comparable peak levels of light availability despite exhibiting higher SIC until August (see Fig. 4.20). This indicates that the light flux through ice in CICE is sufficient to increase light availability up to a similar level as in the neXtSIM-simulation until the end of June.

The comparison of the SIC maps with the light availability maps (both not included) show for the neXtSIM-simulation that areas of increasing light availability (light limitation factor $>$ 0.1) co-locate with areas of SIC $<$ 0.9. This can also be observed when comparing these maps from the CICE-simulation (not shown), although the increase of light availability is not restricted to the areas of SIC decline during the later months of spring. This is the expected result of light flux through sea ice in CICE.

The comparison of the difference maps for light availability (Fig. 4.17) and SIC (Fig. 4.21) from 2012 as example reveal that neXtSIM simulates lower SIC in the southern regions of the Arctic Atlantic, where it is also less light limited especially during the early spring months. The strong correlation between SIC and light availability during early spring is confirmed by the results of the linear regression analysis, which yields r-values of $\geq$ 0.45 (all p-values $<$ 0.0001) for March and April of both years and simulations (Table of r-values not shown).

The observations presented above suggest that the decline in SIC is of high importance for the light availability during early spring, when SIT still increases in both simulations. Atmospheric radiation appears too weak to reach through the thicker sea ice in this region in CICE until the late spring. It suggests that this difference in the sea ice models has a negligible impact on the integrated GPP rates during the spring bloom onset. It also emphasizes the importance of the parameter 'SIC' as determinant of PP in a region of overall thicker sea ice.

5.2.3 Mixed layer depth and sea ice parameters

Although the maps of light limitation and primary production show high correspondence in both model simulations and years, factors such as mixed layer shoaling and nutrient availability may influence productivity.

The integrated GPP map of May (see Fig. 5.1 as example from 2013) of the CICE-simulation shows a centrally located area of low integrated GPP rates, despite high light availability observed at that time in this area (compare Fig. 5.2). This location is not not nitrate limited, but shows a significantly deeper mixed layer, as can be seen in the map of May 2013 in Fig. 4.19. Hence,

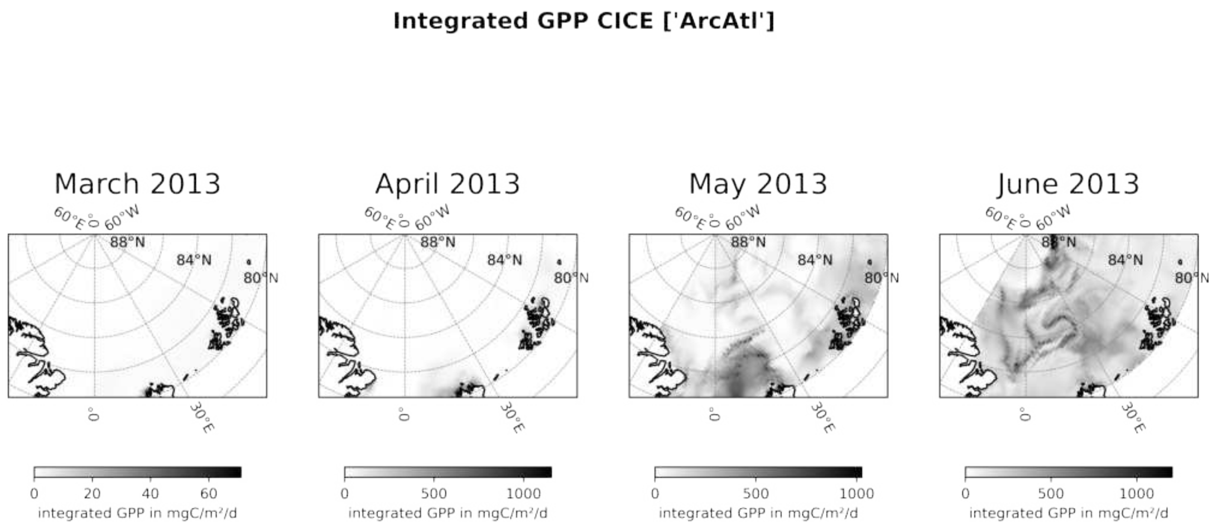

Figure 5.1: Maps of integrated GPP rates (in mg C m^{-2} d^{-1}) in the Arctic Atlantic region from the CICE-simulation for March to June 2012, plotted from monthly mean files.

integrated GPP in CICE appears to be limited by the vertical distribution of phytoplankton and its grazers in the water column in this area.

Whether this differences in vertical mixing is cause by differences in the sea ice parameters is discussed as follows. From the time series of sea ice thickness (not shown) it can be seen that sea ice congelation continues until the end of June in both simulations. However, SIT increase is smaller in CICE across the region. This would result in lower volumes of brine ejection during ice growth, lower surface salinity and thus weaker mixing in CICE. The maps of SIT (not shown) neither indicate a considerable ice growth in the area of deeper MLD in May 2013 in CICE. This makes differences SIT an unlikely driver of the differences in vertical mixing.

To further investigate the potential causes of the difference in MLD, sea surface salinity maps were plotted from the monthly files for March to June. As can be seen in the difference map for May 2013 presented Fig. 5.3, the CICE-simulation reaches higher surface salinity values compared to neXtSIM in the central area showing the deeper mixed layer.

This suggests, that the region receives less of the fresher polar water from the Transpolar Drift (see the map of surface circulation in Fig. 2.1(b)) in the CICE-simulation. This may be explained by the difference in atmospheric forcing between the simulations, since the TPC is partly driven by prevailing winds from Siberia towards Greenland (Johnson, 2024). A significant influence of this polar water on water column properties has been observed by (Kohlbach et al., 2025).

The spatial relationship between mixed layer shoaling due to sea ice melt and its effects on primary production could not be observed. However, sea ice parameters may trigger differences in the winter MLD. neXtSIM shows deeper winter mixing (see time series in Fig. 4.18), which corresponds to the much stronger sea ice thickness increase until the end of June across the region. Congelation would lead to larger volumes of brine being ejected into the upper ocean in neXtSIM, which would enhance vertical mixing. Since the stronger atmospheric forcing in the

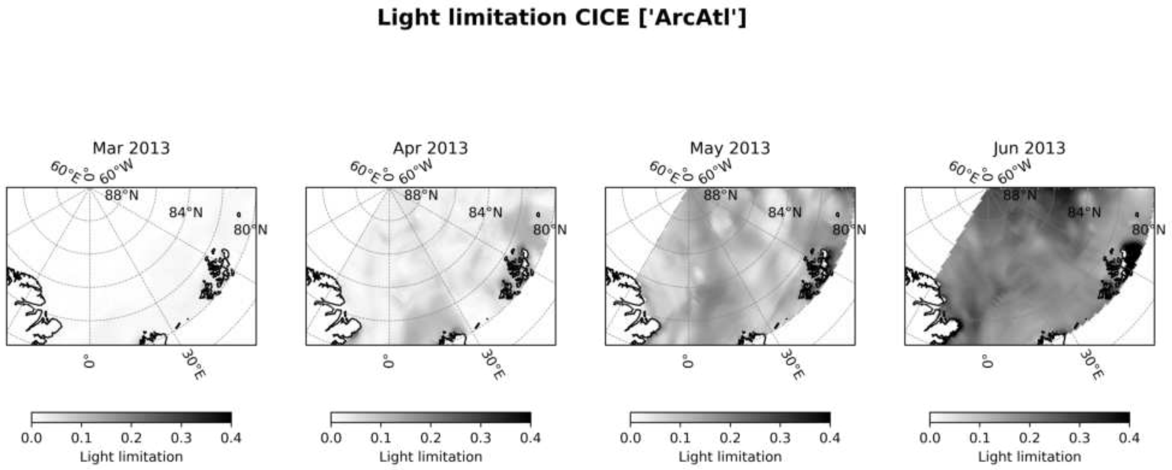

Figure 5.2: Maps of light limitation (integrated over 100 m) in the Arctc Atlantic region from the CICE-simulation for March to June in 2013, plotted from monthly mean files. Darker shading indicates higher light availability.

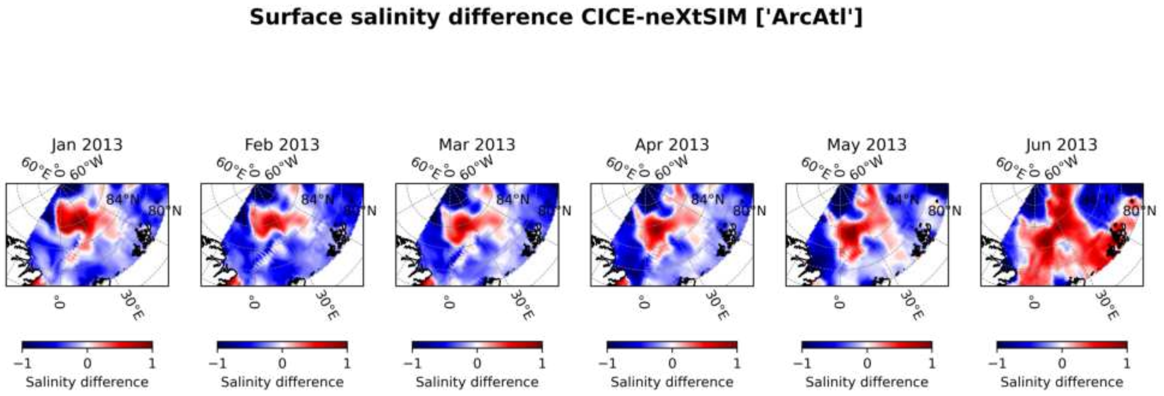

Figure 5.3: Difference maps (CICE minus neXtSIM) of surface salinity in the Arctic Atlantic region for January to June 2012, plotted from monthly mean files. Red areas indicate higher surface salinity in CICE, blue areas indicate higher surface salinities in neXtSIM.

neXtSIM-simulation also influences the vertical mixing, especially during winter storms, it is not possible to discern which of these factors is more relevant for the deeper winter mixing in neXtSIM.

5.2.4 Concluding remarks

The analysis and discussion of results from the Arctic Atlantic region suggests that spring bloom onset and magnitude of primary production are largely driven by light availability. This factor appears mostly influenced by SIC in both model simulations. The alleviation of light limitation is more homogeneous in CICE during the later spring months, which is associated with radiation fluxes through the ice in this model. However, the effect of this difference in ice thermodynamics on integrated GPP seems to be negligible during early spring, when atmospheric radiation in this high latitude region is too weak to penetrate through the ice in CICE. The deeper winter mixing may partly be driven by larger SIT increases in neXtSIM, which also seems to positively affect nutrient availability.

5.3 Chukchi Sea

5.3.1 Spring bloom and primary production magnitude

The daily time series of integrated GPP presented in Fig. 4.22 show an earlier spring bloom onset and earlier peak production rates during both years for the CICE-simulation. Therefore, it is expected that the CICE-simulation will show stronger light availability than the neXtSIM-simulation.

The daily time series of the light limitation factor for both years presented in Fig. 4.24 confirm this assumption, showing that the CICE-simulation is less light limited during the growth seasons in both years, and that light availability increases stronger in both years. This stronger light availability during the time of the spring bloom onset in CICE is also observed in the maps in Fig. 4.27, which show the difference in light availability between model simulations for 2012 as an example. CICE shows larger light limitation factors (i.e. light availability) across most areas of the Chukchi Sea.

Neither of the simulations shows nitrate limitation of the system. This aligns with the reported high nutrient levels in Chukchi Sea due to large influx volumes through the Bering Strait, which has been reported to cause the highest primary production rates in the region compared to areas in the Pacific sector of the Arctic Ocean (Zheng et al., 2021).

5.3.2 Light availability and sea ice parameters

To determine whether the differences in sea ice characteristics affects primary production in the Chukchi Sea, maps of SIC were compared to light availability maps and integrated GPP maps.

Both simulations show a co-location of areas with SIC < 0.9 and increasing light limitation factors (compare Fig. 4.34 and Fig. 4.26 as example for neXtSIM in 2012). These areas of lower SIC also co-locate with areas of increased integrated GPP rates in both simulations and years (see Fig. 4.23 for neXtSIM 2012). In response to the light flux through sea ice in CICE, light availability and integrated GPP also start to increase in areas of SIC larger than 0.9, mostly as of April in both years (compare Fig. 4.25 and 4.35 for 2012). Nevertheless, the increase in integrated GPP rates is stronger in areas of lower SIC in CICE during those months (map not shown).

The difference map of light availability, presented in Fig. 4.27 for 2012 as an example, show stronger light availability in neXtSIM in some confined areas along the Alaskan Coast. These costal stretched are know areas of landfast ice and polynya formation, which can be simulated by the neXtSIM sea ice model (Rheinlænder et al., 2022).

The observations discussed above suggest that the decline in SIC is very important for the onset of the primary production during the early spring months in both simulations, and that the integrated GPP is enhanced by light flux through ice in later spring in CICE. The results of the linear regression analysis (see Table 4.2) support this assessment. Absolute r-values for the neXtSIM-simulation were larger compared to the CICE-simulation during most month, except in April of both years. This shows that integrated GPP is more correlated to a decline in SIC in neXtSIM compared to CICE. Absolute r-values were larger than 0.4 in March and April of both years and for both simulations, with the exception of March 2012 in CICE. This supports the assumption that SIC decline is more influential on integrated GPP during the early spring.

5.3.3 Mixed layer depth and sea ice parameters

As discussed before, vertical mixing is know to have an effect on phytoplankton distribution and spring bloom onset. To identify whether the difference in sea ice parameters and their potential influence on MLD affect primary production modeling in the region, first the time series of MLD (see Fig. 4.31) and integrated GPP (see Fig. 4.13) were compared. It shows that the timing of the spring bloom onset and the mixed layer shoaling do not align in the CICE-simulation in either year. Shoaling starts approximately at the time when the productivity peak is already reached. This is different for the neXtSIM-simulation in 2012, when the onset of the bloom is roughly aligned with the start of the MLD shoaling, and peak production rates are achieved once the shallow summer MLD has established. The comparison of difference maps of the MLD with difference maps for both sea ice parameters (both not shown) did not yield any visible correspondence.

The rather shallow MLD in the Chukchi Sea with a spatially averaged maximum depth of 35 m in both simulations is related to the shallow bathymetry of the region, and the influence of the fresh water influx from the Pacific Ocean through the Bering Strait, which is know to significantly enhance stratification in the region (Woodgate et al., 2006). Hence, the stronger shoaling in neXtSIM could be associated with the stronger wind forcing that changes inflow volumes through the Bering Strait (Woodgate, 2018).

5.3.4 Missing peak production in neXtSIM

The missing spring peak production in 2013 in the neXtSIM-simulation (see Fig. 4.22) may be caused by higher rates of zooplankton consumption compared to the previous year and the CICE-simulation. This assumption could not be confirmed, as the time series of zooplankton abundance plotted from the daily files (not shown) did not show high abundance during spring 2013 in neXtSIM.

Another potential explanation for the missing peak production could be a difference in how the phytoplankton community is affected by limiting factors. The time series of light limitation (see Fig. 4.24) showed lower light availability in neXtSIM compared to CICE, and in 2013 compared to 2012. However, these differences appear to be too small to trigger a 'failure' of spring bloom.

As mentioned above, the influx from the boundary oceans can affect the species composition of phytoplankton in the Arctic Ocean through advection of different phytoplankton species (Timmermans & Marshall, 2020; Woodgate, 2018). Changes in phytoplankton assemblage may therefore change the nutrient requirements, as advected taxa may be limited by other micro- or macro-nutrients. A difference in this advection between both simulations may arise from the difference in atmospheric forcing.

5.3.5 Concluding remarks

In the Chukchi Sea, the CICE-simulation showed higher rates of primary production, despite larger SIT and comparable SIC with neXtSIM. Considering the slightly stronger SIC decline during spring in CICE, all these observations point at the relevance of SIC for integrated GPP. The spatial analysis showed that this was specifically true during the early spring months, when atmospheric solar radiation influx appeared to be too low to affectively trigger integrated GPP underneath the sea ice in CICE, even though the model allows for light flux through the ice. The influence of the sea ice parameters on the MLD and stratification could not be established, likely due to the shallow bathymetry and strong influence of the influx water from the Pacific Ocean.

5.4 Carbon export

Carbon export rates in the Arctic Atlantic and Barents Sea regions appeared to be very similar in magnitude and seasonal cycle at 300 m depth (Barents Sea, Arctic Atlantic) and 500 m depth (Arctic Atlantic). The strongest difference between carbon export in the simulations was identified at 300 m depth in the Chukchi Sea (see Fig. 4.30). It seems that the carbon export follows roughly the integrated GPP curves, which is most apparent in the Chukchi Sea (compare Fig. 4.22) with its missing spring peak in neXtSIM in 2013.

As deeper vertical mixing results in faster downward transport of detritus, the materials are less degraded when they reach the layer underneath a thick mixed layer, which increases gravitational sinking speeds. Therefore, MLD has a two-fold effect on carbon export rates. Therefore, this preliminary analysis of carbon export should be supplemented with spatial analysis of integrated GPP, MLD, and sea ice parameters, to better understand to which extent sea ice parameters influence the rates of carbon export. This is planned during further research.

5.5 Synthesis of regional analysis

The analysis of the selected regions showed that both sea ice models simulate SIT and SIC differently for the low sea ice year 2012 compared to 2013. In Arctic Atlantic and Chukchi Sea, SIT and SIC minimum values were lower in summer of 2012 compared to summer of 2013. In the Barents Sea, summer SIC and SIT approach zero in both years and simulations. Thus the difference between years was determined from the maximum values, which were smaller in 2012 for SIT and SIC in both simulations compared to 2013.

The climatology for SIC showed that the neXtSIM sea ice model simulated lower SIC across the Arctic domain compared to CICE. This is likely related to the brittle rheology of the neXtSIM sea ice model, which affects the dynamics and thermodynamics of the pack ice through the simulation of fractal features. Lower overall SIC and faster SIC decline in spring in the neXtSIM-simulation were found for the Barents Sea and the Arctic Atlantic region. In contrast, SIC were very similar in the Chukchi Sea, and the SIC decline in CICE was even slightly faster than in the neXtSIM-simulation. The very strong decrease in SIC in both simulations in Chukchi Sea, from winter concentrations of approximately 1 down to 0.2 during summer, indicates that the pack ice becomes mobile very fast. This would result in lower rates of deformation stress on the sea ice, which thus diminishes the effect of the brittle rheology on sea ice characteristics. Furthermore, the faster decline in SIC in CICE could also be related to differences in thermodynamic melt arising from the difference in SIT. For further analysis, it is suggested to investigate sea ice velocities to better understand the sea ice dynamic behavior in Chukchi Sea.

The effect of differences in SIC between simulations on light availability appeared clearly in all regions of analysis. In regions of generally low SIC, such as the ice edge region in the Barents Sea, the light flux through ice in the CICE model appeared to have an additional effect on increasing light availability and integrated GPP in comparison to neXtSIM. In areas of higher SIC and SIT, this difference in sea ice models appeared less important during the early spring months, where SIC was the major determinant of light availability in both simulations. However, during later spring, light flux through ice seemed to positively affect light availability in CICE compared to neXtSIM. This is likely related to an increasing strength of solar radiation with progressing polar day.

Through their influence on SIC, the different sea ice rheologies appeared to cause differences in integrated GPP via light limitation. To better analyze the importance of this effect, it is recommended to add light flux through sea ice in the neXtSIM-simulation. This appears especially relevant for comparison of integrated GPP rates in areas of lower latitudes and lower SIC. It will also be relevant to analyze production rates during later spring under lower SIC, as well as the comparison of the total amount of GPP produced during a growth season.

As the brittle rheology of neXtSIM affects ridge formation and thus the sea ice topography, the sea ice models will likely differ in sea ice albedo. The more rigid topography in neXtSIM restricts the formation of large melt ponds and delays the snow melt through snow redistribution during ridging. This likely causes the sea ice albedo to decrease slower in neXtSIM, which would delay sea ice melt at the ice surface in neXtSIM compared to CICE. At the same time, a higher ratio of open water resulting from fractal features in neXtSIM could increase melt of the surrounding sea ice from the heat absorbed by the ocean via the open water surface. For further research, it is suggested to also look at the sea ice albedo variable that is available in the data output of both sea ice models.

The influx of melt water into the upper ocean and its influence on shoaling affected integrated GPP in the Barents Sea and in the Arctic Atlantic region. Furthermore, the deeper winter mixing in the Arctic Atlantic region in the neXtSIM-simulation may have partly been driven by larger SIT, with an effect on nutrient availability for the region. Therefore, differences in rheology that influence the sea ice congelation and sea ice melt may have an influence on primary production modeling in HYCOM-ECOSMO.

However, the differences in wind forcing between the simulations may have also affected the differences in stratification in these regions to a certain extent. Therefore, it is recommended to set up the simulations with the same atmospheric forcing, to identify in how far stratification is affected by the differences in sea ice rheology. This appears especially important in the inflow areas of the Arctic Ocean.

Chapter 6

Conclusions

The comparison of the HYCOM-CICE-ECOSMO with the HYCOM-neXtSIM-ECOSMO simulation showed that the difference in sea ice model caused differences in primary production timing and magnitude between simulations. The differences in integrated gross primary production were correlated to differences in light availability, which was strongly linked to the seasonal sea ice concentration decline in all regions. These differences in SIC between simulations are a result of the differences in sea ice model behavior, and thus primary production is indirectly affected by the model rheology via light limitation.

In some regions (Arctic Atlantic and Barents Sea), differences in sea ice melt and formation appeared to affect the water column stratification and vertical mixing. This may have caused differences in primary production via phytoplankton distribution and nutrient availability in the water column. However, influx variations from the Atlantic and the Pacific oceans triggered by differences in wind forcing between simulations could not be ruled out as predictor of mixed layer depth. Nevertheless, to a certain extent sea ice rheology seems to have a direct effect on phytoplankton growth by influencing sea ice melt and formation processes.

To better assess the effects of the mechanical damage in the brittle rheology on light availability and vertical mixing compared to the EVP rheology, it is recommended to run both simulations without light flux through ice, and with the same wind forcing.

Carbon export rates appeared to be mainly conditioned by the GPP rates during the growth season. Therefore, the effects of the different rheologies on primary production will affect carbon export similarly. It is proposed to conduct spatial analysis of carbon export rates compared to integrated GPP rates and MLD. This will allow to determine to which extent a difference in vertical mixing arising from sea ice melt and formation in both simulations influences the sinking of detrital biomass.

The results of this study show that the differences in sea ice characteristics arising from different sea ice model rheologies influence primary production modeling in the biogeochemical ocean model HYCOM-ECOSMO. This points at the importance of employing sea ice models that represent the sea ice cover with its fractal features in a more realistic way. Considering the anticipated changes in sea ice dynamics expected from the reduction and thinning of the Arctic sea ice, this seems to be especially true for future predictions of Arctic Ocean primary production and carbon sequestration.

References

Ardyna, M., & Arrigo, K. R. (2020). Phytoplankton dynamics in a changing Arctic Ocean. *Nature Climate Change*, *10*, 892–903. doi:10.1038/s41558-020-0905-y.

Arrigo, K. R., & Van Dijken, G. L. (2003). Phytoplankton dynamics within 37 Antarctic coastal polynya systems. *Journal of Geophysical Research: Oceans*, *108*, 2002JC001739. doi:10.1029/2002JC001739.

Arrigo, K. R., & Van Dijken, G. L. (2015). Continued increases in Arctic Ocean primary production. *Progress in Oceanography*, *136*, 60–70. doi:10.1016/j.pocean.2015.05.002.

Årthun, M., Brakstad, A., Dörr, J., Johnson, H. L., Mans, C., Semper, S., & Våge, K. (2025). Atlantification drives recent strengthening of the Arctic overturning circulation. *Science Advances*, *11*, eadu1794. doi:10.1126/sciadv.adu1794.

Australian Antarctic Division (2017). Sea Ice. https://www.antarctica.gov.au/about-antarctica/ice-and-atmosphere/sea-ice/. Last access: 25.09.2025.

Barber, D., & Massom, R. (2007). Chapter 1: The Role of Sea Ice in Arctic and Antarctic Polynyas. In W. Smith, & D. Barber (Eds.), *Elsevier Oceanography Series* (pp. 1–54). Elsevier volume 74. doi:10.1016/S0422-9894(06)74001-6.

Behrenfeld, M. J. (2010). Abandoning Sverdrup's Critical Depth Hypothesis on phytoplankton blooms. *Ecology*, *91*, 977–989. doi:10.1890/09-1207.1.

Björk, G., & Winsor, P. (2006). The deep waters of the Eurasian Basin, Arctic Ocean: Geothermal heat flow, mixing and renewal. *Deep Sea Research Part I: Oceanographic Research Papers*, *53*, 1253–1271. doi:10.1016/j.dsr.2006.05.006.

Blockley, E., Johannessen, J. A., & Ólason, E. Ö. (2022). Sea Ice modelling. In E. Alvarez Fanjul, S. Ciliberti, & P. Bahurel (Eds.), *Implementing Operational Ocean Monitoring and Forecasting Systems* (pp. 124–150). Paris, France: IOC-UNESCO. doi:10.25607/OBP-1774.

Boutin, G., Ólason, E., Rampal, P., Regan, H., Lique, C., Talandier, C., Brodeau, L., & Ricker, R. (2023). Arctic sea ice mass balance in a new coupled ice–ocean model using a brittle rheology framework. *The Cryosphere*, *17*, 617–638. doi:10.5194/tc-17-617-2023.

Bretones, A., Nisancioglu, K. H., Jensen, M. F., Brakstad, A., & Yang, S. (2022). Transient Increase in Arctic Deep-Water Formation and Ocean Circulation under Sea Ice Retreat. *Journal of Climate*, *35*, 109–124. doi:10.1175/jcli-d-21-0152.1.

Bruggeman, J., & Bolding, K. (2014). A general framework for aquatic biogeochemical models. *Environmental Modelling & Software*, *61*, 249–265. doi:10.1016/j.envsoft.2014.04.002.

Castellani, G., Losch, M., Lange, B. A., & Flores, H. (2017). Modeling Arctic sea-ice algae: Physical drivers of spatial distribution and algae phenology. *Journal of Geophysical Research: Oceans*, *122*, 7466–7487. doi:10.1002/2017JC012828.

Daewel, U., & Schrum, C. (2013). Simulating long-term dynamics of the coupled North Sea and Baltic Sea ecosystem with ECOSMO II: Model description and validation. *Journal of Marine Systems*, *119–120*, 30–49. doi:10.1016/j.jmarsys.2013.03.008.

Dee, D. P., Uppala, S. M., Simmons, A. J., Berrisford, P., Poli, P., Kobayashi, S., Andrae, U., Balmaseda, M. A., Balsamo, G., Bauer, P., Bechtold, P., Beljaars, A. C. M., Van De Berg, L., Bidlot, J., Bormann, N., Delsol, C., Dragani, R., Fuentes, M., Geer, A. J., Haimberger, L., Healy, S. B., Hersbach, H., Hólm, E. V., Isaksen, L., Kållberg, P., Köhler, M., Matricardi, M., McNally, A. P., Monge-Sanz, B. M., Morcrette, J.-J., Park, B.-K., Peubey, C., De Rosnay, P., Tavolato, C., Thépaut, J.-N., & Vitart, F. (2011). The ERA-Interim reanalysis: Configuration and performance of the data assimilation system. *Quarterly Journal of the Royal Meteorological Society*, *137*, 553–597. doi:10.1002/qj.828.

Druzhkova, E. I., Ishkulova, T. G., & Pastukhov, I. A. (2020). Features of summer ice-edge bloom in the Barents Sea. *IOP Conference Series: Earth and Environmental Science*, *539*, 012186. doi:10.1088/1755-1315/539/1/012186.

EU Copernicus Marine Service (2020). Arctic Ocean Physics Reanalysis. doi:10.48670/MOI-00007.

Fan, Y., Liu, W., Zhang, P., Chen, R., & Li, L. (2023). North Atlantic Oscillation contributes to the subpolar North Atlantic cooling in the past century. *Climate Dynamics*, *61*, 5199–5215. doi:10.1007/s00382-023-06847-y.

Feltham, D. L. (2008). Sea Ice Rheology. *Annual Review of Fluid Mechanics*, *40*, 91–112. doi:10.1146/annurev.fluid.40.111406.102151.

Fernández-Méndez, M., Olsen, L. M., Kauko, H. M., Meyer, A., Rösel, A., Merkouriadi, I., Mundy, C. J., Ehn, J. K., Johansson, A. M., Wagner, P. M., Ervik, Å., Sorrell, B. K., Duarte, P., Wold, A., Hop, H., & Assmy, P. (2018). Algal Hot Spots in a Changing Arctic Ocean: Sea-Ice Ridges and the Snow-Ice Interface. *Frontiers in Marine Science*, *5*, 75. doi:10.3389/fmars.2018.00075.

Flatau, M. K., Talley, L., & Niiler, P. P. (2003). The North Atlantic Oscillation, Surface Current Velocities, and SST Changes in the Subpolar North Atlantic. *Journal of Climate*, *16*, 2355–2369. doi:10.1175/2787.1.

Flores, H., Veyssière, G., Castellani, G., Wilkinson, J., Hoppmann, M., Karcher, M., Valcic, L., Cornils, A., Geoffroy, M., Nicolaus, M., Niehoff, B., Priou, P., Schmidt, K., & Stroeve, J. (2023). Sea-ice decline could keep zooplankton deeper for longer. *Nature Climate Change*, *13*, 1122–1130. doi:10.1038/s41558-023-01779-1.

Frey, K. E., Stock, L. V., Garcia, C. O., Cooper, L. W., & Grebmeier, J. M. (2024). NOAA Arctic Report Card 2024 : Arctic Ocean Primary Productivity: The Response of Marine Algae to Climate Warming and Sea Ice Decline. *NOAA technical report OAR ARC*, *24–06*, 58–70. doi:10.25923/9EX0-T425.

Geider, R., MacIntyre, H., & Kana, T. (1997). Dynamic model of phytoplankton growth and acclimation:responses of the balanced growth rate and the chlorophyll a:carbon ratio to light, nutrient-limitation and temperature. *Marine Ecology Progress Series*, *148*, 187–200. doi:10.3354/meps148187.

Gonçalves-Araujo, R. (2016). *Tracing Environmental Variability in the Changing Arctic Ocean with Optical Measurements of Dissolved Organic Matter*. Ph.D. thesis Universität Bremen. doi:10.13140/RG.2.2.16968.32001.

Hoppe, C. J. M., Wolf, K. K. E., Cottier, F., Leu, E., Maturilli, M., & Rost, B. (2024). The effects of biomass depth distribution on phytoplankton spring bloom dynamics and composition in an Arctic fjord. *Elementa: Science of the Anthropocene*, *12*, 00137. doi:10.1525/elementa.2023.00137.

Hunke, E. C., & Dukowicz, J. K. (1997). An Elastic-Viscous-Plastic Model for Sea Ice Dynamics. *Journal of Physical Oceanography*, *27*, 1849–1867. doi:10.1175/1520-0485(1997)027<1849:AEVPMF>2.0.CO;2.

Hunke, E. C., Lipscomb, W. H., & Turner, A. K. (2010). Sea-ice models for climate study: Retrospective and new directions. *Journal of Glaciology*, *56*, 1162–1172. doi:10.3189/002214311796406095.

Hunke, E. C., Lipscomb, W. H., Turner, A. K., Jeffery, N., & Elliott, S. (2015). CICE: The Los Alamos Sea Ice Model Documentation and Software User's Manual Version 5.1 (LA-CC-06-012).

Jakobsson, M., Mohammad, R., Karlsson, M., Salas-Romero, S., Vacek, F., Heinze, F., Bringensparr, C., Castro, C. F., Johnson, P., Kinney, J., Cardigos, S., Bogonko, M., Accettella, D., Amblas, D., An, L., Bohan, A., Brandt, A., Bünz, S., Canals, M., Casamor, J. L., Coakley, B., Cornish, N., Danielson, S., Demarte, M., Di Franco, D., Dickson, M.-L., Dorschel, B., Dowdeswell, J. A., Dreutter, S., Fremand, A. C., Hall, J. K., Hally, B., Holland, D., Hong, J. K., Ivaldi, R., Knutz, P. C., Krawczyk, D. W., Kristofferson, Y., Lastras, G., Leck, C., Lucchi, R. G., Masetti, G., Morlighem, M., Muchowski, J., Nielsen, T., Noormets, R., Plaza-Faverola, A., Prescott, M. M., Purser, A., Rasmussen, T. L., Rebesco, M., Rignot, E., Rysgaard, S., Silyakova, A., Snoeijs-Leijonmalm, P., Sørensen, A., Straneo, F., Sutherland, D. A., Tate, A. J., Travaglini, P., Trenholm, N., Van Wijk, E., Wallace, L., Willis, J. K., Wood, M., Zimmermann, M., Zinglersen, K. B., & Mayer, L. (2024). The International Bathymetric Chart of the Arctic Ocean Version 5.0. *Scientific Data*, *11*, 1420. doi:10.1038/s41597-024-04278-w.

Johnson, R. S. (2024). The Transpolar Drift current: An ocean-ice-wind complex in rotating, spherical coordinates. *Monatshefte für Mathematik*, *205*, 735–755. doi:10.1007/s00605-024-01995-7.

Jones, E., Rudels, B., & Anderson, L. (1995). Deep waters of the Arctic Ocean: Origins and circulation. *Deep Sea Research Part I: Oceanographic Research Papers*, *42*, 737–760. doi:10.1016/0967-0637(95)00013-v.

Jones, E. P. (2001). Circulation in the Arctic Ocean. *Polar Research*, *20*, 139–146. doi:10.3402/polar.v20i2.6510.

Kohlbach, D., Fransson, A., Amargant-Arumi, M., Assmann, K. M., Assmy, P., Bratbak, G., Chierici, M., Cristea, A., Divine, D. V., Down, E., Eikrem, W., Foss, Ø., Gardner, J., Gradinger, R. R., Granskog, M. A., Hess, S., Ingvaldsen, R. B., Koenig, Z., Kwaśniewski, S., Majaneva, S., Marquardt, M., Müller, O., Ntniou, I. V., Ormańczyk, M., Raffel, B., Renaud, P., Renner, A. H. H., De Freitas, T. R., Sen, A., Smoła, Z., Svensen, C., Vader, A., Våge, S., Wiktor, J., Wold, A., Zabłocka, M., Ziegler, A., & Bluhm, B. A. (2025). Nansen and Amundsen basins: Gradients of physico-chemical properties and biota composition with implications for future resource management of the central Arctic Ocean. *Elementa: Science of the Anthropocene*, *13*, 00016. doi:10.1525/elementa.2024.00016.

Krisch, S., Hopwood, M. J., Roig, S., Gerringa, L. J. A., Middag, R., Rutgers Van Der Loeff, M. M., Petrova, M. V., Lodeiro, P., Colombo, M., Cullen, J. T., Jackson, S. L., Heimbürger-Boavida, L.-E., & Achterberg, E. P. (2022). Arctic-Atlantic exchange of the dissolved micronutrients iron, manganese, cobalt, nickel, copper and zinc with a focus on Fram Strait. *Global Biogeochemical Cycles*, *36*, e2021GB007191. doi:10.1029/2021GB007191.

Krumpen, T., Von Albedyll, L., Bünger, H. J., Castellani, G., Hartmann, J., Helm, V., Hendricks, S., Hutter, N., Landy, J. C., Lisovski, S., Lüpkes, C., Rohde, J., Suhrhoff, M., & Haas, C. (2025). Smoother sea ice with fewer pressure ridges in a more dynamic Arctic. *Nature Climate Change*, *15*, 66–72. doi:10.1038/s41558-024-02199-5.

Lewis, K. M., Van Dijken, G. L., & Arrigo, K. R. (2020). Changes in phytoplankton concentration now drive increased Arctic Ocean primary production. *Science*, *369*, 198–202. doi:10.1126/science.aay8380.

Maslanik, J., Stroeve, J., Fowler, C., & Emery, W. (2011). Distribution and trends in Arctic sea ice age through spring 2011: Trends in Arctic sea ice age. *Geophysical Research Letters*, *38*, n/a–n/a. doi:10.1029/2011GL047735.

Maslanik, J. A., Fowler, C., Stroeve, J., Drobot, S., Zwally, J., Yi, D., & Emery, W. (2007). A younger, thinner Arctic ice cover: Increased potential for rapid, extensive sea-ice loss. *Geophysical Research Letters*, *34*, 2007GL032043. doi:10.1029/2007GL032043.

Meier, W. N., Petty, A., & Hendricks, S. (2024). NOAA Arctic Report Card 2024: Sea Ice. *NOAA technical report OAR ARC*, *24–06*, 41–50. doi:10.25923/AKSK-7P66.

Mõttus, M., Sulev, M., Baret, F., Lopez-Lozano, R., & Reinart, A. (2012). Photosynthetically Active Radiation: Measurement and Modeling. In R. A. Meyers (Ed.), *Encyclopedia of Sustainability Science and Technology* (pp. 7902–7932). New York, NY: Springer New York. doi:10.1007/978-1-4419-0851-3_451.

NERSC (2025). Source code and utilities for the NERSC version of HYCOM+CICE. https://github.com/nansencenter/NERSC-HYCOM-CICE/tree/master/hycom/MSCPROGS. Last access: 20.09.2025.

NOAA (2025). World Ocean Atlas. https://www.ncei.noaa.gov/products/world-ocean-atlas. Last access: 20.09.2025.

NSIDC (2025). National Snow and Ice Data Center (NSIDC). https://nsidc.org/learn/parts-cryosphere/sea-ice/science-sea-ice. Last access: 22.09.2025.

Ólason, E., Boutin, G., Korosov, A., Rampal, P., Williams, T., Kimmritz, M., Dansereau, V., & Samaké, A. (2022). A New Brittle Rheology and Numerical Framework for Large-Scale Sea-Ice Models. *Journal of Advances in Modeling Earth Systems*, *14*, e2021MS002685. doi:10.1029/2021MS002685.

Ólason, E., Boutin, G., Williams, T., Korosov, A., Regan, H., Rheinlænder, J., Rampal, P., Flocco, D., Samaké, A., Davy, R., Spain, T., & Chua, S. (2025). (PREPRINT) The next generation sea-ice model neXtSIM, version 2. doi:10.5194/egusphere-2024-3521.

Oziel, L., Gürses, Ö., Torres-Valdés, S., Hoppe, C. J. M., Rost, B., Karakuş, O., Danek, C., Koch, B. P., Nissen, C., Koldunov, N., Wang, Q., Völker, C., Iversen, M., Juhls, B., & Hauck, J. (2025). Climate change and terrigenous inputs decrease the efficiency of the future Arctic Ocean's biological carbon pump. *Nature Climate Change*, *15*, 171–179. doi:10.1038/s41558-024-02233-6.

Perovich, D. K., & Polashenski, C. (2012). Albedo evolution of seasonal Arctic sea ice. *Geophysical Research Letters*, *39*, 2012GL051432. doi:10.1029/2012GL051432.

Qu, M., Lei, R., Liu, Y., & Li, N. (2024). Arctic Sea ice leads detected using sentinel-1B SAR image and their responses to atmosphere circulation and sea ice dynamics. *Remote Sensing of Environment*, *308*, 114193. doi:10.1016/j.rse.2024.114193.

Rampal, P., Bouillon, S., Ólason, E., & Morlighem, M. (2016). neXtSIM: A new Lagrangian sea ice model. *The Cryosphere*, *10*, 1055–1073. doi:10.5194/tc-10-1055-2016.

Rampal, P., Dansereau, V., Olason, E., Bouillon, S., Williams, T., Korosov, A., & Samaké, A. (2019). On the multi-fractal scaling properties of sea ice deformation. *The Cryosphere*, *13*, 2457–2474. doi:10.5194/tc-13-2457-2019.

Randelhoff, A., Holding, J., Janout, M., Sejr, M. K., Babin, M., Tremblay, J.-É., & Alkire, M. B. (2020). Pan-Arctic Ocean Primary Production Constrained by Turbulent Nitrate Fluxes. *Frontiers in Marine Science*, *7*, 150. doi:10.3389/fmars.2020.00150.

Rantanen, M., Karpechko, A. Y., Lipponen, A., Nordling, K., Hyvärinen, O., Ruosteenoja, K., Vihma, T., & Laaksonen, A. (2022). The Arctic has warmed nearly four times faster than the globe since 1979. *Communications Earth & Environment*, *3*, 168. doi:10.1038/s43247-022-00498-3.

Regan, H., Rampal, P., Ólason, E., Boutin, G., & Korosov, A. (2023). Modelling the evolution of Arctic multiyear sea ice over 2000–2018. *The Cryosphere*, *17*, 1873–1893. doi:10.5194/tc-17-1873-2023.

Rheinlænder, J. W., Davy, R., Ólason, E., Rampal, P., Spensberger, C., Williams, T. D., Korosov, A., & Spengler, T. (2022). Driving Mechanisms of an Extreme Winter Sea Ice Breakup Event in the Beaufort Sea. *Geophysical Research Letters*, *49*, e2022GL099024. doi:10.1029/2022GL099024.

Rogge, A., Janout, M., Loginova, N., Trudnowska, E., Hörstmann, C., Wekerle, C., Oziel, L., Schourup-Kristensen, V., Ruiz-Castillo, E., Schulz, K., Povazhnyy, V. V., Iversen, M. H., & Waite, A. M. (2023). Carbon dioxide sink in the Arctic Ocean from cross-shelf transport of dense Barents Sea water. *Nature Geoscience*, *16*, 82–88. doi:10.1038/s41561-022-01069-z.

Rudels, B. (2009). Arctic ocean circulation. In J. Steele, S. Thorpe, & K. Turekian (Eds.), *Encyclopedia of Ocean Science* (pp. 211–225). United Kingdom: Academic Press. (2nd ed.).

Rudels, B., & Carmack, E. (2022). Arctic Ocean Water Mass Structure and Circulation. *Oceanography*, *35*, 52–65. doi:10.5670/oceanog.2022.116.

Sakov, P., Counillon, F., Bertino, L., Lisæter, K. A., Oke, P. R., & Korablev, A. (2012). TOPAZ4: An ocean-sea ice data assimilation system for the North Atlantic and Arctic. *Ocean Science*, *8*, 633–656. doi:10.5194/os-8-633-2012.

Sakshaug, E., & Slagstad, D. (1992). Sea ice and wind: Effects on primary productivity in the Barents Sea. *Atmosphere-Ocean*, *30*, 579–591. doi:10.1080/07055900.1992.9649456.

Schulzweida, U. (2023). CDO User Guide. *CERN Data Center*, *Zenodo*. doi:10.5281/ZENODO.1435454.

Semtner, A. J. (1976). A Model for the Thermodynamic Growth of Sea Ice in Numerical Investigations of Climate. *Journal of Physical Oceanography*, *6*, 379–389. doi:10.1175/1520-0485(1976)006<0379:amfttg>2.0.co;2.

Serreze, M. C., Barrett, A. P., Crawford, A. D., & Woodgate, R. A. (2019). Monthly Variability in Bering Strait Oceanic Volume and Heat Transports, Links to Atmospheric Circulation and Ocean Temperature, and Implications for Sea Ice Conditions. *Journal of Geophysical Research: Oceans*, *124*, 9317–9337. doi:10.1029/2019JC015422.

Stubbins, A., Spencer, R. G. M., Mann, P. J., Holmes, R. M., McClelland, J. W., Niggemann, J., & Dittmar, T. (2015). Utilizing colored dissolved organic matter to derive dissolved black carbon export by arctic rivers. *Frontiers in Earth Science*, *3*. doi:10.3389/feart.2015.00063.

Sundfjord, A., Ellingsen, I., Slagstad, D., & Svendsen, H. (2008). Vertical mixing in the marginal ice zone of the northern Barents Sea - Results from numerical model experiments. *Deep Sea Research Part II: Topical Studies in Oceanography*, *55*, 2154–2168. doi:10.1016/j.dsr2.2008.05.027.

Sverdrup, H. U. (1953). On Conditions for the Vernal Blooming of Phytoplankton. *ICES Journal of Marine Science*, *18*, 287–295. doi:10.1093/icesjms/18.3.287.

Swoboda, S., Krumpen, T., Nöthig, E.-M., Metfies, K., Ramondenc, S., Wollenburg, J., Fahl, K., Peeken, I., & Iversen, M. (2024). Release of ballast material during sea-ice melt enhances carbon export in the Arctic Ocean. *PNAS Nexus*, *3*, pgae081. doi:10.1093/pnasnexus/pgae081.

Terhaar, J., Lauerwald, R., Regnier, P., Gruber, N., & Bopp, L. (2021). Around one third of current Arctic Ocean primary production sustained by rivers and coastal erosion. *Nature Communications*, *12*, 169. doi:10.1038/s41467-020-20470-z.

Timmermans, M.-L., & Marshall, J. (2020). Understanding Arctic Ocean Circulation: A Review of Ocean Dynamics in a Changing Climate. *Journal of Geophysical Research: Oceans*, *125*, e2018JC014378. doi:10.1029/2018JC014378.

Vonk, J. E., Fritz, M., Speetjens, N. J., Babin, M., Bartsch, A., Basso, L. S., Bröder, L., Göckede, M., Gustafsson, Ö., Hugelius, G., Irrgang, A. M., Juhls, B., Kuhn, M. A., Lantuit, H., Manizza, M., Martens, J., O'Regan, M., Suslova, A., Tank, S. E., Terhaar, J., & Zolkos, S. (2025). The land-ocean Arctic carbon cycle. *Nature Reviews Earth & Environment*, *6*, 86–105. doi:`10.1038/s43017-024-00627-w`.

Wang, Q., Wang, X., Wekerle, C., Danilov, S., Jung, T., Koldunov, N., Lind, S., Sein, D., Shu, Q., & Sidorenko, D. (2019). Ocean Heat Transport Into the Barents Sea: Distinct Controls on the Upward Trend and Interannual Variability. *Geophysical Research Letters*, *46*, 13180–13190. doi:`10.1029/2019GL083837`.

Westberry, T. K., Silsbe, G. M., & Behrenfeld, M. J. (2023). Gross and net primary production in the global ocean: An ocean color remote sensing perspective. *Earth-Science Reviews*, *237*, 104322. doi:`10.1016/j.earscirev.2023.104322`.

Winton, M. (2000). A Reformulated Three-Layer Sea Ice Model. *Journal of Atmospheric and Oceanic Technology*, *17*, 525–531. doi:`10.1175/1520-0426(2000)017<0525:artlsi>2.0.co;2`.

Woodgate, R. A. (2018). Increases in the Pacific inflow to the Arctic from 1990 to 2015, and insights into seasonal trends and driving mechanisms from year-round Bering Strait mooring data. *Progress in Oceanography*, *160*, 124–154. doi:`10.1016/j.pocean.2017.12.007`.

Woodgate, R. A., Aagaard, K., & Weingartner, T. J. (2006). Interannual changes in the Bering Strait fluxes of volume, heat and freshwater between 1991 and 2004. *Geophysical Research Letters*, *33*, 2006GL026931. doi:`10.1029/2006GL026931`.

Yumruktepe, V. Ç., Samuelsen, A., & Daewel, U. (2022). ECOSMO II(CHL): A marine biogeochemical model for the North Atlantic and the Arctic. *Geoscientific Model Development*, *15*, 3901–3921. doi:`10.5194/gmd-15-3901-2022`.

Zender, C. S. (2008). Analysis of self-describing gridded geoscience data with netCDF Operators (NCO). *Environmental Modelling & Software*, *23*, 1338–1342. doi:`10.1016/j.envsoft.2008.03.004`.

Zheng, Z., Wei, H., Luo, X., & Zhao, W. (2021). Mechanisms of Persistent High Primary Production During the Growing Season in the Chukchi Sea. *Ecosystems*, *24*, 891–910. doi:`10.1007/s10021-020-00559-8`.